BAW-1350
REACTOR TECHNOLOGY
(TID-4500)

1000-MWe LMFBR ACCIDENT ANALYSIS AND SAFETY SYSTEM DESIGN STUDY

— Topical Report —

Accident-Initiating Conditions
Part 1, Flow Abnormalities

by

J. H. Scott
R. W. Moore

Approved by: M. W. Croft
Project Manager

November 1970

ANL Contract No. 31-109-38-2339
B&W Contract No. 847-0501

BABCOCK & WILCOX
Power Generation Division
Nuclear Power Generation Department
P.O. Box 1260
Lynchburg, Virginia 24505

DISCLAIMER

THIS PAGE
WAS INTENTIONALLY
LEFT BLANK

PREFACE

This report was originally prepared as a technical note to document the work performed in a specific contract activity as soon as the work was completed. The technical editing was limited in order to meet the objective of timely reporting. The report was issued for USAEC-ANL use only, and the intent was to update and consolidate the information from all technical notes in a comprehensive phase report before final publication for public distribution at the end of Phase II.

This plan was changed when the contract was terminated in October 1970 for the convenience of the government. Instead, a final summary report will be prepared, and the previously issued technical notes will be published as formal topical reports. In accordance with the modified plan, this technical note is being published in its original form without further editing or modification except for minor technical corrections and changes in the title and date of issue. Even without updating and technical editing, the report provides detailed information that should be helpful in evaluating and resolving LMFBR safety questions in related areas.

M. W. Croft
Lynchburg, Virginia
November 15, 1970

CONTENTS

List of Figures

Figures (Con't)

Figures (con't)

1. INTRODUCTION

Babcock & Wilcox is performing work on the Accident Analysis and Safety System Design Study under ANL Contract No. 31-109-38-2339. Various utility companies are participating in the work on a cost-sharing basis, under separate agreements with B&W. The study is being conducted primarily to gain a better understanding of how safety requirements affect the design of large, liquid-metal, breeder reactors. The objective will be met by analyzing accidents that determine the design basis of the protective systems and safety features and developing conceptual designs for these protective systems and engineered safety features. The reference design[1] of B&W's 1000-MWe Follow-On Study is the basis for the Study.

The accurate analysis of accidents generally requires as precise a definition of the initiating events as is possible, since even relatively small uncertainties in the definition of initiating conditions could lead to large uncertainties in the accident analyses. Activities 210 and 211 of the Study involve the definition of such initiating conditions. Several broad categories of initiating conditions were identified from the malfunction survey performed during Phase I.[2] Briefly, these categories are as follows:

1. Accident-initiating conditions arising from primary coolant system abnormalities.

2. Accident-initiating conditions arising from secondary coolant loop abnormalities.

3. Accident-initiating conditions arising from reactivity insertions.

Studies involving the first two categories have been completed. The models, methods calculations, and results of these studies are discussed in this report.

The phenomena associated with certain types of accidents sometimes make it difficult to define the interface between initiating conditions and accident conditions. In these studies, a given transient was treated as an initiating event until irreversible damage occurred (such as cladding failure). The consequences of irreversible damage will then be investigated under Activity 220, Accident Analysis and DBA Selection.

Two broad categories of full-power initiating conditions have been investigated:

1. Flow abnormalities in the primary system.
2. Flow abnormalities in the secondary system.

Flow blockages have been excluded from these investigations, since blockage events will be investigated under Activity 220, Accident Analyses. Appropriate sensitivity studies were performed for each of the two broad categories; the results are discussed in detail in section 3.

Several primary loop abnormalities have been studied:

1. Complete loss of six primary pumps.
2. Complete loss of two primary pumps.
3. Double-ended break in a 28-inch primary pipe.

Several other events might have been studied, but each of them results in less severe transients than do the events listed.

Only one secondary loop malfunction was studied—the complete and instantaneous loss of access to the heat sink. This event bounds the severity of identifiable events. The results of these calculations are as follows:

1. No fuel melting occurred for any transient in which the control system functioned by the fourth level of protection.

2. No sodium boiling occurred for any protected transient.

3. No cladding temperatures in excess of 1420 F occurred for any transient.

From these results, one can conclude that:

1. No irreversible damage results from identifiable malfunctions unless partial failure of the protection system is postulated.

2. Flow abnormalities at power may be eliminated from the category of events potentially leading to gross damage.

2. SUMMARY OF RESULTS

Two broad categories of initiating conditions with the reactor at power have been investigated: flow abnormalities arising in the primary loop and abnormalities arising in the secondary loop. The TART[3] computer program with point kinetics and multiregion thermal model was used to study these transient conditions. In addition, the analog computer model was used to investigate certain phenomena relating to abnormalities of the secondary loop. The following abnormalities of the primary loop were investigated:

1. Complete loss of six primary pumps.
2. Complete loss of two primary pumps.
3. Double-ended break in a 28-inch primary pipe.

A number of other abnormalities, such as a hole in the inlet plenum shield tank might have been studied, but in every case these events obviously give rise to less severe transients than do the events listed above. Hence, the events listed above provide an upper bound for the severity of identifiable flow abnormalities in the primary loop. Flow blockages, both local and general, were excluded from this investigation because blockage accidents will be investigated under Activity 220, Accident Analysis.

Similarly, in the secondary loop a number of malfunctions, such as turbine trip, steam generator failure, etc., could influence conditions in the primary system; however, all of these events are less severe than the complete, instantaneous loss of access to the heat sink. As a consequence, instantaneous loss of the heat sink was the only event investigated under secondary loop abnormalities. Appropriate sensitivity studies were performed for each of the two broad categories investigated. These studies are discussed in detail in section 3.

The results of these calculations indicate that no fuel melting or cladding failure occurs for any transient so long as the protective system

functions normally. As to flow abnormalities in the primary loop, three levels of protection may be by passed before failure thresholds are approached. If one postulates such partial failure of the protection system and a rapid flow decay, then high cladding temperatures occur in the hot pin. These temperatures are probably sufficient to cause some cladding failure.

On the basis of these studies it can be concluded that no irreversible damage results from identifiable flow abnormalities unless partial failure of the protection system is postulated. At least three levels of protection must fail (three simultaneous faults) before even limited cladding failure can occur. Thus, the probability that flow abnormalities at full power will lead to gross core damage is extremely small.

3. DESCRIPTION OF WORK

3.1. Objective

These studies were undertaken to provide data and initial conditions for Activity 220, Accident Analysis and DBA Selection. In addition, information on the relative importance of various core parameters may be useful in designing the protective systems. The work performed under Activities 210 and 211 is based on information generated during Phase I of the Study, particularly the malfunction catalog and fault trees. The various aspects of primary and secondary loop abnormalities are discussed in detail in this section.

The technical approach to the entire problem of analyzing initiating conditions is discussed. The methods, models, and calculations for primary and secondary system abnormalities are reviewed in detail. Finally, the results of the calculations, including sensitivity studies, are presented. The impact of the results on the Study is discussed in section 4.

3.2. Technical Approach

The conditions arising from faults in the primary or secondary coolant systems can be analyzed in several ways. The approach used here emphasizes the analysis of identifiable accidents. In certain cases, however, it has been expedient to postulate an accident representing an upper bound on the severity of credible accidents. For example, consider malfunctions arising in the secondary loop. No malfunction can be identified whose impact on the reactor core is more severe than complete and instantaneous loss of access to the heat sink (secondary loop). Hence, if the analysis of loss-of-heat sink indicates that the core can be protected, there is no point in analyzing other secondary loop malfunctions. This scheme works well for certain types of accidents and substantially reduces the computing time required. However, this

method cannot and should not be applied generally, so that the causal sequence leading to the abnormalities must be defined for most of the analyses.

In order to define the causal sequence, the Phase I fault trees and malfunction survey were reviewed. These malfunctions were then analyzed to assess the conditions arising from them. The conditions, in turn, were used as input to various dynamic computer codes, and the core response was observed. The most sensitive and/or uncertain parameters were varied in order to evaluate the effect of such uncertainties on the response of the reactor.

The transients arising from the various malfunctions or faults were recorded for selected parameters, such as fuel temperature, cladding temperature, power level, coolant temperature, and the time-dependent values of the reactivity coefficients. These monitored variables were used to evaluate the time and extent of cladding failures, if any. The failure criteria for the various failure mechanisms are presented in the appendix. The course of the transient beyond significant fuel failure is more properly the subject of Activity 220, Accident Analysis, and is discussed in the report.

3.3. Methods and Analytical Models

The results and the reliability of safety analyses are likely to be quite sensitive to the models and analytical methods used. Therefore, the methods and models used in this segment of Activity 210 are discussed in some detail.

3.3.1. Flow Coastdown Model

A digital computer program, FLODN, was written to describe more accurately the flow transients arising from either complete or partial loss of pumping power. FLODN solves the LMFBR primary pump and system hydraulic equations for the case of loss of electric power to any number of pumps. FLODN is similar to the flow coastdown model in the TART code, but contains some improvements. The static fluid moment operating against the pump is included, backward impeller rotation and backflow through an inactive pump is allowed, and the fluid inertia terms are included.

The pump-speed equation, neglecting rotational friction and windage losses, is taken to be

$$\frac{I}{g}\frac{d\omega}{dt} = \frac{550(HP_e)}{\omega} - \frac{144}{\rho}\left(\frac{W\Delta P}{\omega}\right) - f(\omega, \Delta P, W) \tag{1}$$

where I is the pump inertia, g is the gravitational constant, ω is the pump speed (radius/second), HP_e is the electric power supplied to the pump, ρ is the fluid density, W is the flow rate through the pump, and P is the pressure rise across the pump. The second term on the right represents the dynamic fluid torque, and the third term represents the static fluid torque. These two terms give the total brake torque on the pump and can be defined as

$$\text{Brake torque} = \left[\frac{T}{\omega^2}\right] \omega^2 \tag{2}$$

where the $\left[\frac{T}{\omega^2}\right]$ term can be determined using the pump affinity laws and the pump-performance data supplied by the manufacturer.

This term can be expressed as a function of $\left[\frac{W}{\omega}\right]$ for the pump; thus, if the flow through the pump and the pump speed are known, then the total brake torque can be found. Also, the pressure rise across the pump can be found from the similar characteristic function of $\left[\frac{\Delta p}{\omega^2}\right]$ versus $\left[\frac{W}{\omega}\right]$. These two characteristic functions for a typical centrifugal pump are shown in Figure 1, where $\left[\frac{\Delta p}{\omega^2}\right]$, $\left[\frac{T}{\omega^2}\right]$, and $\left[\frac{W}{\omega}\right]$ are all normalized to the standard operating point. It should be noted that for an inactive pump, the (HP_e) term is set to zero, since by definition no power is supplied to an inactive pump.

The hydraulic equations for the primary system are given by continuity of mass and momentum. The pressure rise across a pump must be equal to the system's pressure drops, which are taken to be the drop in the inlet pipes, the drop across the core, and the drop across the intermediate heat exchangers (IHX). That is, for an active pump,

$$\Delta P_\rho^a = \Delta P_{inlet}^a + \Delta P_{core} + \Delta P_{ihx} \tag{3}$$

and for an inactive pump,

$$\Delta P_{\rho}^{in} = \Delta P_{inlet}^{in} + \Delta P_{core} + \Delta P_{ihx}. \tag{4}$$

The pressure drops in the inlet pipes are given by

$$\Delta P_{inlet} = \frac{k_1 |W| W}{k, W^2} + \frac{1}{144g}\left(\frac{L}{A}\right)_1 \frac{dW}{dt}. \tag{5}$$

where W is the flow through either an active or an inactive pump. The pressure deop across the core is given as

$$\Delta P_{core} = k_2 |W_c| W_c + \frac{1}{144g}\left(\frac{L}{A}\right)_2 \frac{dW_c}{dt}. \tag{6}$$

By continuity of mass, the flow through the core is given as the sum of the flows through the active pumps; i.e.,

$$W_c = N_a W_a + N_{in} W_{in}, \tag{7}$$

where N_a is the number of active pumps and N_{in} is the number of inactive pumps. Note that W_{in} may be negative in the case of backflow through an inactive pump, but equation 7 still holds, since the backflow through an inactive pump must be supplied by the active pumps. The pressure drop across all the IHXs is given similarly as

$$\Delta P_{ihx} = k_3 W_x |W_x| + \frac{1}{144g}\left(\frac{L}{A}\right)_3 \frac{dW_x}{dt}. \tag{8}$$

where W_x is the flow through a single IHX. However, in the pot-type LMFBR system, this pressure drop must be equal to the differential head due to the elevation difference between the inner (core) and outer (pot) vessels. This head is given as

$$\Delta H = H_o + \left(\frac{g}{144 g_c}\right)\left(\frac{1}{A_{cr}} + \frac{1}{A_p}\right) \int_0^t \left[W_c(\tau) - N_x W_x(\tau)\right] d\tau \tag{9}$$

where ΔH is in psig, A_{cr} is the cross-sectional area of the inner (core) vessel, A_p is the area of the outer (pot) vessel, and N_x is the number of IHXs.

The foregoing equations can be written as a system of 10 first-order differential equations with four additional relationships given by the pump's characteristic functions. In FLODN the differential equations are solved using Euler's method, which is rather inefficient relative to truncation error but is straightforward to program.

The characteristic functions are given in FLODN as input tables, and a linear interpretation table look-up routine is used to determine $\left[\Delta p/\omega^2\right]$ and $\left[T/\omega^2\right]$ as functions of $\left[W/\omega\right]$ for both active and inactive pumps. No stability problems have been encountered with FLODN, and running times on the CDC-6600 are only a few seconds for typical problems.

3.3.2. Fuel Pin Representation

The two fuel pin representations used in the TART program during the flow abnormality studies are briefly discussed below.

3.3.2.1. Nonrestructured Representation

The first pin model assumed no fuel densification effects and no central void. The fuel pin was divided into five nodes of equal radius and nine axial segments. The seven central axial segments represented the core region; the two end segments represented the upper and lower axial blankets, respectively. Axial conduction was neglected. The conductivity function used in this representation was

$$K_{fuel} = 1.7666 \times 10^{-4} + 0.277778/(T_{ji} - 32) \qquad (10)$$

where T is the temperature in the radial node j at a specific axial location i. This representation was found to disagree significantly with TAMPA[4] for end-of-cycle conditions; specifically, the model produced higher fuel temperatures higher than were predicted by TAMPA. As a result, a more sophisticated representation was adapted for end-of-cycle conditions.

3.3.2.2. Restructured Representation

The EOC pin was modeled using nine axial segments with 10 radial nodes. Again, axial conduction was neglected. A central void of 0.003-foot radius was assumed. The conductivity function was taken from the TAMPA code. By these means the effect of fuel densification in the EOC pin was approximated. The results agreed quite well with the conditions predicted by TAMPA; the centerline temperatures agreed to within 50 F.

The conductivity function used in TART is presented graphically in Figure 2. It should be noted that no true discontinuities were assumed and that the function has a finite slope everywhere. This differs from the TAMPA approach. This approximation to the TAMPA function was made to improve convergence in TART.

3.3.3. Protection System Model

The protection system contains 25 rods, of which seven are safety rods and are thus out of the core during operation. The remaining 18 rods, used as shim rods throughout the cycle, may be inserted at various positions at various times. The distribution of rods among the five TART regions is as follows:

Region	No. of rods (configuration)	Reactivity available for scram
1	1 (all out)	0.00335
2	3 (half-in)	0.0042
	3 (all out)	0.0084
3	2 (half-in)	0.0028
	4 (all out)	0.0112
4	2 (half-in)	0.0028
	4 (all out)	0.0112
5	6 (all out)	0.0168

This distribution represents the rod configuration at some point early in life and thus approximates the minimum worth available at scram.

The worth of the central safety rod was assumed to be $0.92 and that of all other rods to be worth $0.77. The rod worth curve, percentage worth versus percentage insertion, is presented in Figure 3.

The scram set points for the core instrumentation were 2621 MW for the power monitor (107% power) and 1139 F for the bulk outlet temperature monitor. The bulk outlet temperature thermocouple was located just above the upper axial blanket outlet in the outlet plenum. A 5-second time constant was assumed for this thermocouple.

The scram delay time for the system (300 ms) is defined as the elapsed time between the detection of an out-of-limit condition and the first motion of the rods. The normal rod speed for shim motion is 15 in./min; the scram speed of 0.7g is backed up by a secondary motor-driven 30 in./s.

3.3.4. Pipe Break Model

The model describing the flow transient following a double-ended break in a 28-inch primary pipe is quite simple and rests upon the approximation that the flow rate following the break will eventually approach the asymptotic equilibrium flow for five pumps at a pressure differential characteristic of the core only. The double-ended break is assumed to occur at the inlet nozzle. Figure 4 shows the flow rate as a function of differential pressure for five and six operating pumps and for the core and the core plus inlet nozzle. The asymptotic equilibrium flow for five pumps and the core, exclusive of the inlet nozzle, is 20,000 lbm/s. The normal core flow with six pumps operating is 25,738 lbm/s. The nature of the transient between the two equilibrium flow conditions is not known from this analysis. It was assumed that the new equilibrium flow is reached 0.010 second after the break occurs. The transient flow was assumed to follow the relation

$$\text{flow}(t) = \text{flow}(0) - \left(\frac{t}{\Delta t}\right)^{1/2} \Delta\,\text{flow} \qquad (11)$$

where flow(t) = time-dependent flow,

flow(0) = initial flow,

t = 0.01 s,

Δflow = 5738 lbm/s.

The flow transient corresponding to this relation is presented in Figure 5.

3.4. Description of Calculations

This section describes the calculations performed in this segment of Activity 210; pertinent input variables, initial conditions, and assumptions are discussed for each of the three major accident categories.

3.4.1. Flow Coastdown Calculations

One of the most serious malfunctions possible in a reactor core is the interruption of adequate cooling, which may arise from a number of faults such as loss of pumping power, loss of system integrity (due to pipe or vessel rupture), or blockage of flow channels. The latter category of initiating events, blockage of flow channels, is excluded from this study because flow blockages will be investigated under Activity 220, Accident Analysis and DBA selection. A loss of pumping power has a high probability of occurring during the operating lifetime of the plant, so that it is very important to be able to predict the behavior of the reactor system during loss of pumping power transients.

3.4.1.1. Scope of Calculations

A number of variables strongly influence the nature of the flow transient arising from a loss of pumping power. The two variables having the greatest effect on the transient are (1) the number of disabled pumps and (2) the pump's moment of inertia. In principle, it is possible to lose power to any number of pumps; however, in B&W's reference design the loss of power to three, four or five pumps is highly improbable, at least in the sense that multiple simultaneous faults are required.

The six B&W primary pumps are distributed among four nonvital busses, so that at no time will more than two primary pumps draw power from a single bus. This means that the failure of a single bus can effect two primary pumps at most. The simultaneous failure of more than one bus is considered incredible for any event other than the loss of off-site power. In the event that off-site power is lost, all six primary pumps will coast down simultaneously. Since this flow transient is more severe than the transient arising from the loss of three to five pumps, and since the loss of six pumps or two pumps is the most probable failure mode, only six-pump and two-pump coastdowns were investigated. The six-pump coastdown bounds the severity of credible coastdown accidents.

3.4.1.2. Reference Calculations

The flow coastdown calculations were performed with the TART computer code. The reactor was represented by nine axial and seven radial regions; the seven central axial regions represent the active core, while the first and last axial regions represent the lower and upper axial blankets. Of the seven radial regions, one represents the hot pin, one represents the peak (or maximum powered pin), and one represents the radial blanket; the remaining regions represent the remainder of the active core.

The nominal reactivity coefficients, nuclear parameters and sodium worth distribution are as follows:

Doppler coefficient	$\left(T \frac{dk}{dT}\right)$	- 0.00533
Sodium density coefficient	$\left(\rho \frac{dk}{dp}\right)$	0.0253
Axial expansion coefficient	$\left(R \frac{\delta K}{\delta R}\right)$	- 0.532
Linear expansion coefficient	$\left(\frac{1}{L} \frac{\delta L}{\delta T}\right)$	0.0000104
β_{eff}		0.00364
ℓ^*, (s)		0.29×10^{-6}

Two pump inertias were considered in these investigations: the reference design inertia of 15,000 lb-f^2, and an inertia of 6000 lb-ft^2. The flow transients were calculated by the digital code FLODN. The transient resulting from the loss of six primary pumps with a pump inertia of 15,000 lb-ft^2 is shown in Figure 6. The transients for the loss of six primary pumps and two primary pumps, each with pump inertias of 6000 lb-ft^2, are presented in Figures 7 and 8.

Two series of calculations were performed for the flow coastdown accident. The first used the nonrestructured fuel pin model; later, many of these calculations were rerun using the restructured fuel pin model.

3.4.1.3. Results

The results for the reference accident—the accident in which all systems function in their most probable mode—are presented in Figures 9,10, and 11 for six pump, 15,000; six pump, 6000; and two pump, 6000. The loss of pumping power was detected in these cases, and a scram with a 300 ms delay was produced. Figure 9 is a power trace for the loss of six primary pumps with pump inertias of 15,000 lb-ft^2; Figure 10 is a power trace resulting from the loss of six pumps with pump inertias of 6000 lb-ft^2; Figure 11 presents the power transient arising from the loss of two primary pumps, each with a pump inertia of 6000 lb-ft^2. The restructured fuel pin model was used in all cases. It is readily seen that the power (and temperature) transients arising from these reference accidents are of no significance from the safety standpoint.

3.4.1.4. Sensitivity Studies

A number of parameters may influence the course of the coastdown transients. Because of uncertainties in many of these parameters it was necessary to investigate the influence of the most sensitive or uncertain parameters on the response of the reactor. The parameters investigated are as follows:

1. The reactivity coefficients.
2. The fuel pin model.
3. The control system parameters, in particular the rod worths and the delay time.
4. Partial failure of the protection system.
5. Pump inertia.

The reactivity coefficients, pump inertias, and fuel pin model were varied independently. In order to assess the relative importance of the various parameters, the transient was allowed to develop until terminated by a scram initiated by either the power monitor or the bulk outlet temperature monitor. This arrangement is equivalent to bypassing the first three levels of protection: (1) the pump electric power monitors, (2) the flow monitors, and (3) the power to flow ratio monitors. Any of these three detectors will produce a scram much earlier than either the power monitor or the bulk outlet temperature monitor. The use of this analytical scheme in no way implies that one would ever expect three simultaneous faults in the protection system; it is merely expedient from a calculational point of view because it allows enough time for the effect of each parameter to become evident.

The following values of the reactivity coefficients were used in the sensitivity studies with delayed scram: (1) nominal values, (2) 0.5 nominal Doppler with all other coefficients nominal, and (3) zero axial expansion coefficient with all other coefficients nominal, and (4) 1.5 times the sodium density coefficient with all other coefficients nominal. The calculations were performed for pump inertias of 15,000 and 6000 lb-ft^2 with the nonrestructured fuel pin model. The power traces for a 15,000 lb-ft^2 pump inertia and parameters of reactivity coefficients are presented in Figure 12. The corresponding maximum cladding temperatures are presented in Figure 13. Since these calculations included no hot pin, the temperatures presented are for the peak or maximum powered pin. The same variables are plotted for a 6000 lb-ft^2 pump inertia in Figures 14 and 15.

The most important aspect of these results is that, in general, any "worsening" of the reactivity coefficients, that is, increasing of positive coefficients or decreasing of negative coefficients, leads to a more rapid than nominal power rise. This power rise in turn

leads to an earlier than nominal scram and a consequent lowering of the integrated power (and hence the maximum temperatures) for the transient. One can see that increasing the sodium-density coefficient has the most pronounced effect on reactor dynamics.

From Figure 15 it can be seen that the maximum cladding temperatures continue to rise after scram. This effect is produced by the rapid decay of coolant flow for the 6000 lb-ft^2 pump inertia, so that after about 7 seconds the flow is essentially stagnant. Since the calculation does not include the pickup of flow from the pony motors, this is equivalent to decay heating in stagnant sodium. Use of the pony motors would reduce the cladding temperatures to an acceptable level.

Figures 19-A and 20-A of the appendix indicate that some pin damage may occur at cladding temperature of 1300 F, as it does in the steady state. Any failures are expected to occur principally in damaged or defective pins and are not expected to be violent. The consequences of these limited failures will be investigated in Activity 220, Accident Analysis.

Some of the calculations described above were repeated using the restructured fuel pin model and a hot pin representation in TART. Hot pin factors of 1.10 for power and 1.13 for channel enthalpy rise were applied to the peak pin in order to arrive at a consistent hot pin representation. As before, the scram was delayed until either the bulk outlet temperature monitor or the power monitor produced a scram signal.

Figure 16 presents the power traces for a 15,000 lb-ft^2 pump inertia with parameters of reactivity coefficients. Figures 17 and 18 show the centerline fuel and maximum cladding temperatures for the hot pin. As in the previous cases, no fuel melting occurs although relatively high cladding temperatures occur. Figures 19, 20, and 21 present the same information for a coastdown with 6000 lb-ft^2 pump inertia. Again, the cladding temperatures are somewhat high. The effect of the pony motors has been neglected in Figure 21, but if they were taken into account, a single maximum would have occurred in the cladding temperature trace. It can be seen that the

improved heat transfer characteristics of the restructured fuel pin model lead to early scram relative to the nonrestructured model.

The effect of varying certain of the protection system's parameters on the excess integrated energy in a flow coastdown transient were investigated. Here, excess integrated energy is defined as that generated above the energy that would have been generated had the reactor remained in steady-state operation. The two parameters varied were the scram delay time and the total reactivity worth at scram. The base case was the restructured, 6000 lb-ft^2 flow coastdown. The scram delay times were varied from 150 to 500 ms. The total reactivity worths were reduced to 0.25 nominal. The results, in terms of excess integrated energy as a function of magnitudes of the parameters, are presented in Figures 22 and 23.

The excess integrated energy exhibits a weak dependence on the total reactivity worth available at scram over the range of the variables investigated and a strong dependence on scram delay time. As to terminating flow coastdown transients, one can thus conclude that there is little incentive to increase the scram reactivity. However, there may be some incentive to reduce the scram delay.

Consideration of Figures 14-, 19-, and 20-A of the appendix indicates that some failures may occur among damaged or defective pins, but in the absence of molten fuel they are not expected to be violent. If the protective system performs as designed, then no failures are expected.

Selected cases from among all the foregoing analyses were performed with the protection system completely inoperable. Predictably, the transient so induced quickly leads to gross fuel melting, sodium voiding, and cladding failure. While complete failure of the protective system is deemed incredible, certain of these cases may be analyzed further under Activity 220.

The scram mechanisms were deactivated to study the loss of two primary pumps. The power trace produced by this event is displayed in Figure 24. The maximum centerline fuel temperature rise was 150 F, and the maximum cladding temperature rise was 152 F. A new equilibrium power level of 2542 MWt was reached in 3.13 seconds.

3.4.2. Pipe Break Accident

The accident considered here is a double-ended break in a 28-inch primary pipe. The break is assumed to occur at the inlet nozzle and to be complete in 0.01 second. The reactor was represented by seven radial regions and nine axial regions. The fuel pin model was the restructured model. All coefficients were assumed to be nominal, and the scram mechanisms were deactivated. The power trace is displayed in Figure 25.

The results of this event are quite similar to those for the loss of two pumps, since the equilibrium flows are nearly equal. The equilibrium power of 2538 MWt was reached in 1.5 seconds. The maximum fuel and cladding temperatures were 4237 and 1295 F, respectively. It is evident that this transient is acceptable from a safety standpoint even without a scram. No sensitivity studies were performed.

3.4.3. Loss-of-Heat Sink Accident

Many malfunctions of the secondary system could affect the primary system. Since the only couplings between the primary and secondary systems are the intermediate heat exchangers, any secondary system malfunction will be felt by the primary system through the IHXs. The most severe condition that can arise is the complete and instantaneous loss of access to the secondary loop. Consequently, this is the only malfunction studied here.

3.4.3.1. Results

Since this accident is hypothetical in the sense that it is non-mechanistic but bounds the severity of all mechanistic malfunctions, the investigations assumed the form of a parametric study. The TART computer code was used, and the loss of access to the secondary loop was simulated by setting the heat transfer coefficient in each IHX to zero. The reactor was divided into six thermal-hydraulic regions. The hot pin was not included and the nonrestructured fuel pin model was used. The reactivity coefficients were set at their nominal value except for the axial expansion coefficient. Calculations were made with and without axial expansion reactivity coefficients and

with various degrees of coolant channeling in the vessel (defined by a channeling coefficient, α, equal to the ratio of effective mixing volume to the total available volume). Two values of the axial expansion coefficient have been investigated—the nominal value and zero—and all calculations were terminated at 120 seconds real time. Values of α ranging from 0.25 to 1.0 were also considered. All protective functions were bypassed in order to determine the time available to shut down and activate the emergency decay heat removal system.

The effect of coolant channeling in the reactor inlet plenum on core power is illustrated in Figure 26. Values of the channeling coefficient α vary from 1 (perfect mixing) to 0.25 (equivalent to perfect mixing in one-quarter of the available volume); the nominal value of the axial expansion coefficient was used in these calculations. In every case, the power is slowly varying over the duration of the calculation. In only one case, $\alpha = 0.25$, does coolant boiling occur.

The fraction of molten fuel as a function of time after loss of the secondary loops is displayed in Figure 27 for parameters of the channeling coefficient. For the case of perfect mixing, the molten fraction was not significant even at 120 seconds.

The bulk coolant outlet temperature and the coolant outlet temperature of the hottest channel as a function of time are presented in Figure 28 as parameters of the channeling coefficient. In all these calculations, a voiding inception temperature corresponding to 92 F superheat was assumed.

Figures 29 and 30 display the temperatures in the cladding and fuel as a function of time after a loss of heat sink for various values of α. Figure 31, which shows the power trace with and without axial expansion feedback, indicates that feedback is significant in reducing the power rise.

From the various curves it is obvious that for a bulk outlet temperature scram set point of 1139 F, scram will be produced before any fuel melting occurs even for $\alpha = 0.25$. In addition, the cladding temperature rise will be minor if a bulk outlet scram is produced.

From these results, it can be seen that the time available to scram and activate the decay heat removal system is ample. This, in effect, removes secondary loop malfunctions from the category of potential DBAs.

Figure 1. Pump Characteristics Curve

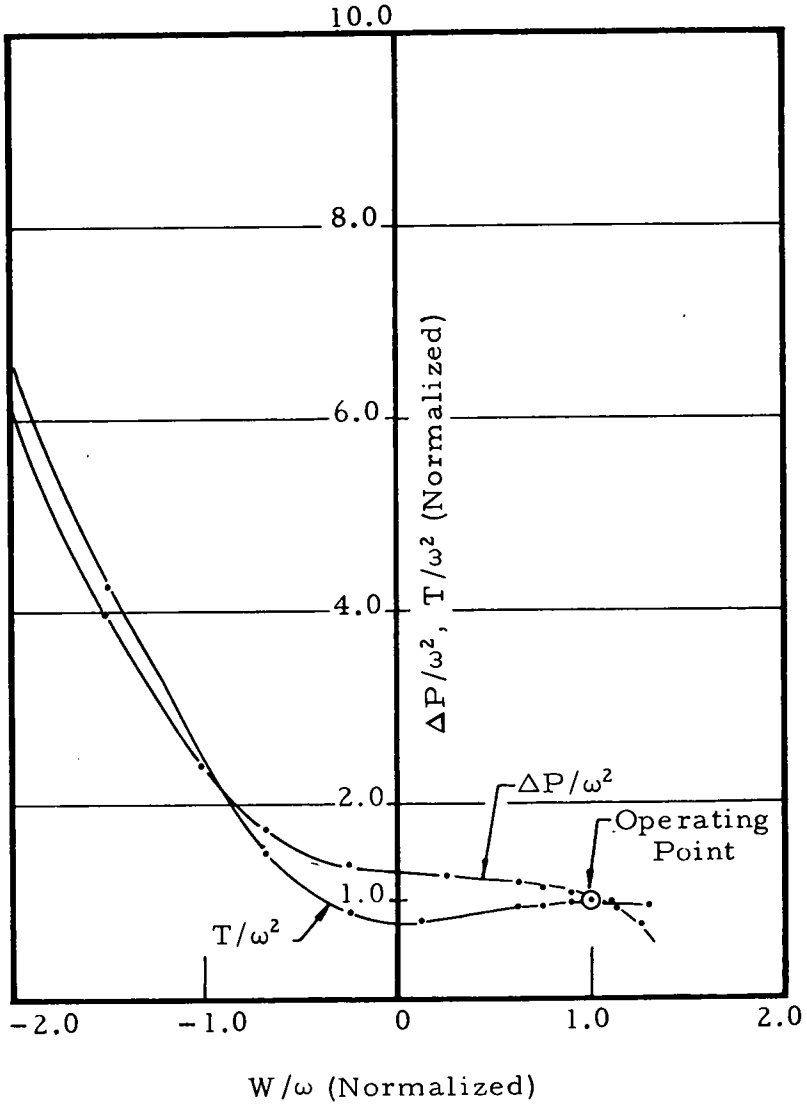

Figure 2. Fuel Conductivity Vs Temperature

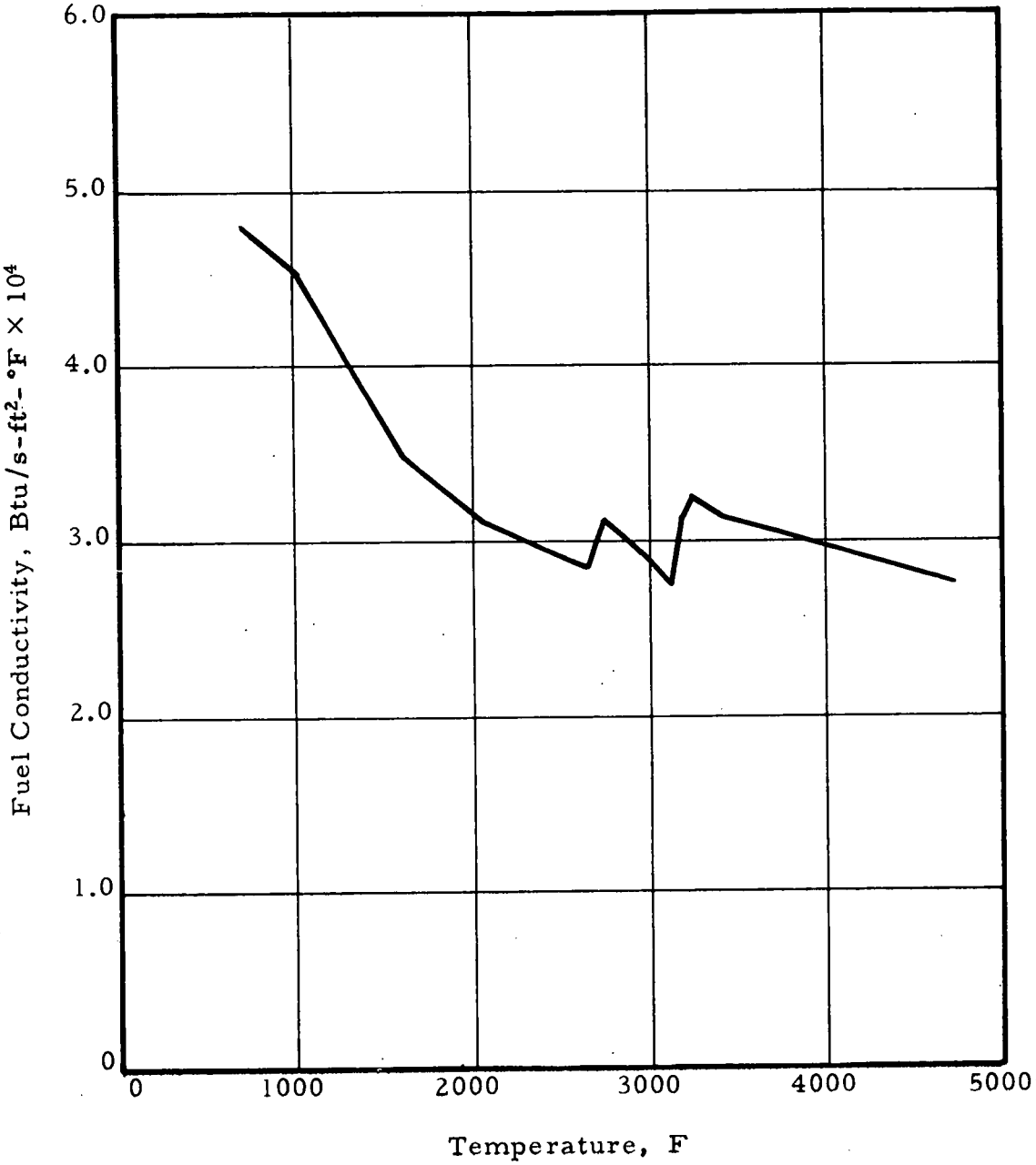

Figure 3. Rod Worth Vs Fraction Inserted

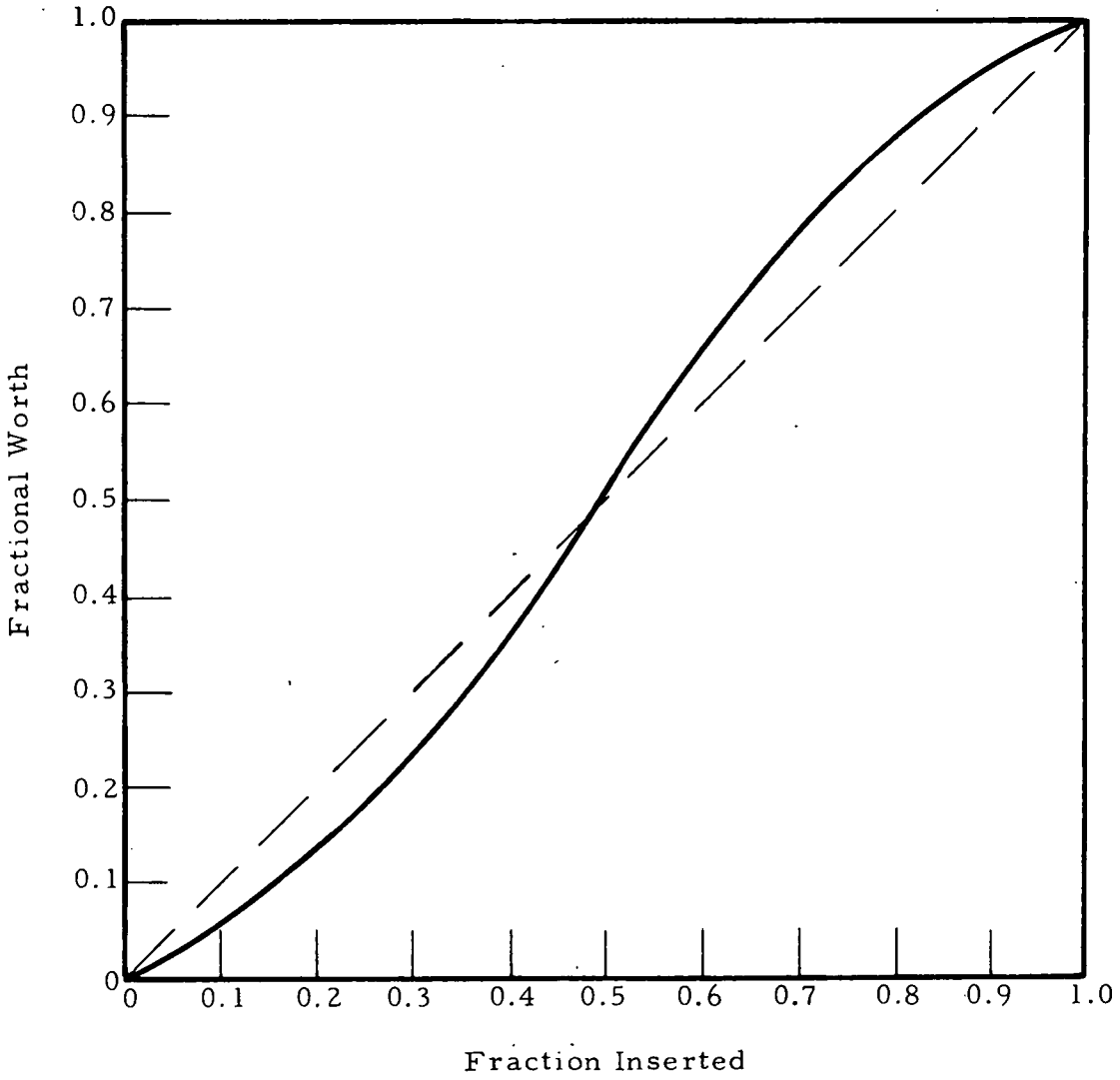

Figure 4. Asymptotic Flows

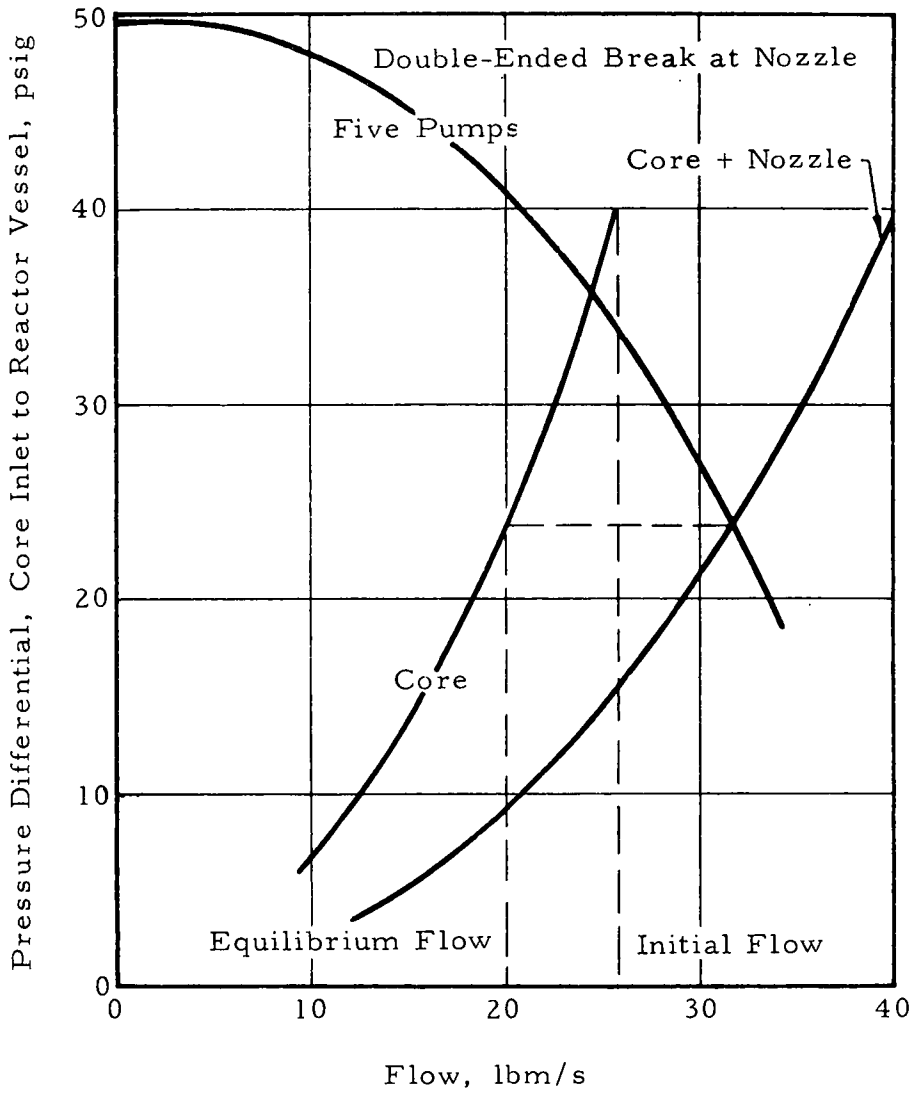

Figure 5. Flow Transient Following Pipe Break

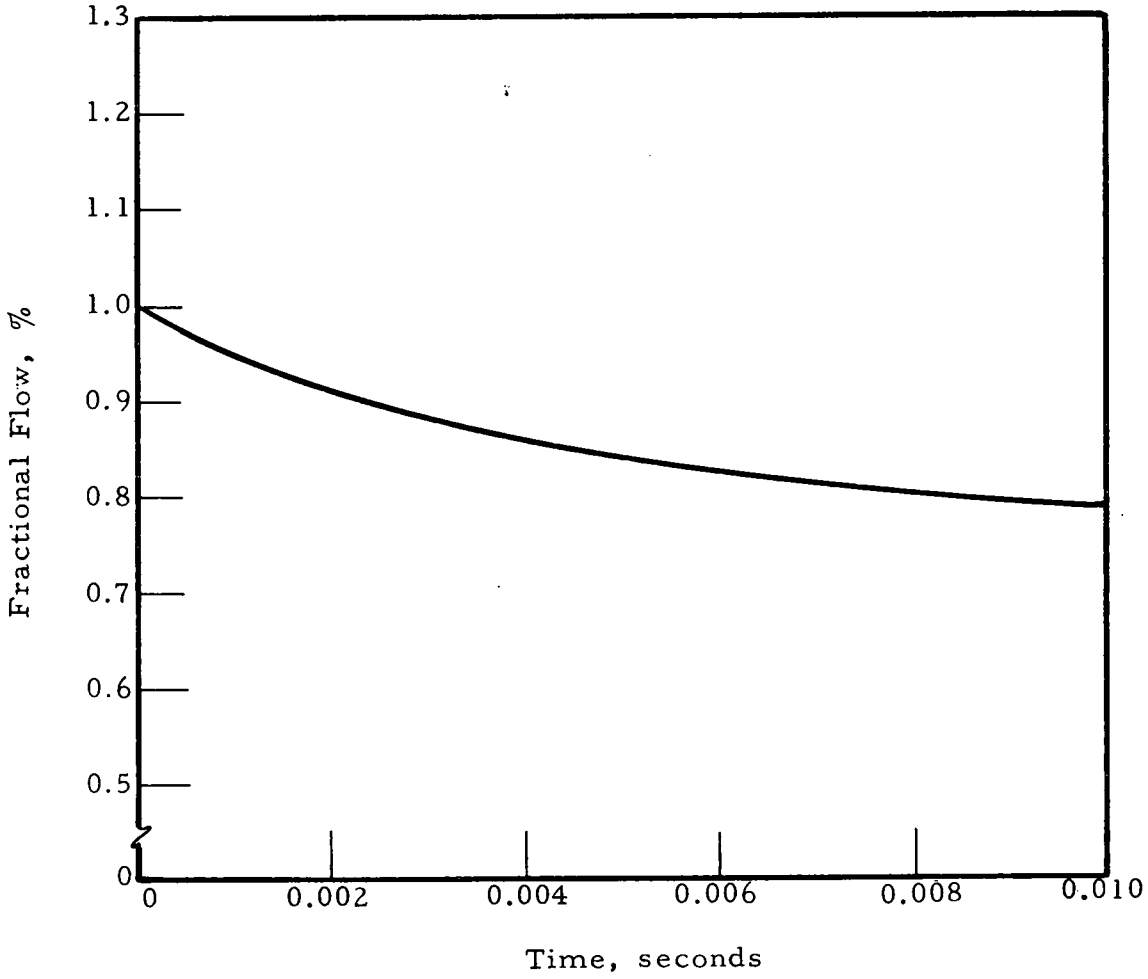

Figure 6. Pump Inertia Flow Decay (15,000 lb-ft^2)

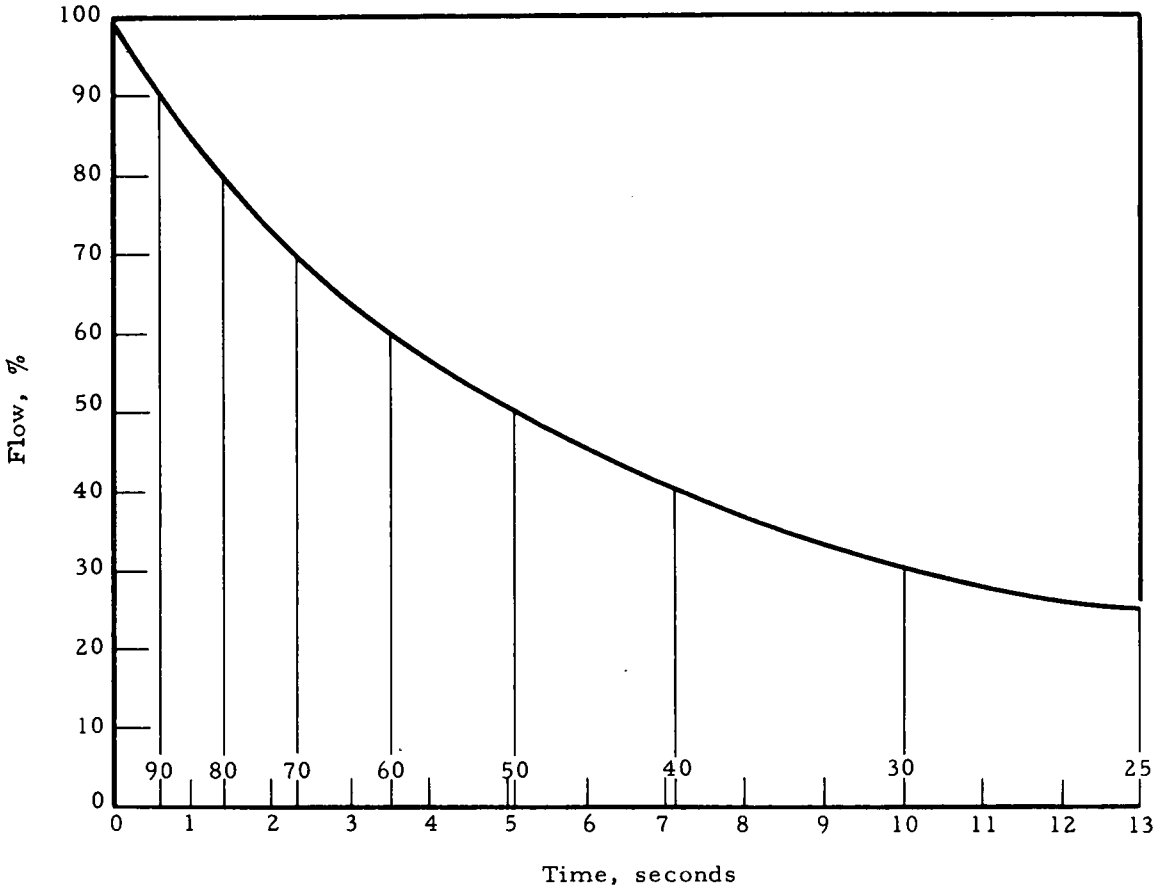

Figure 7. Pump Inertia Flow Decay (6000 lb-ft^2)

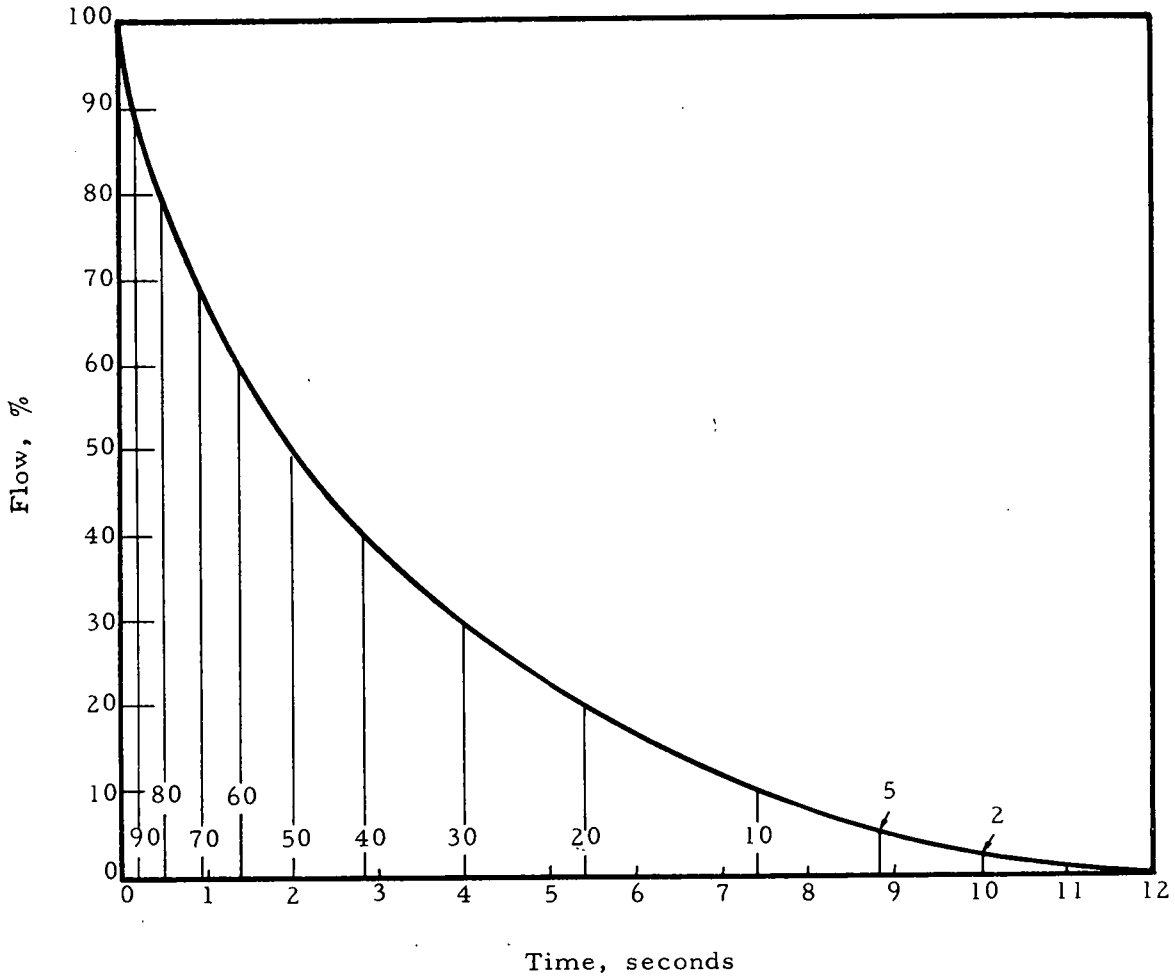

Figure 8. Two-Pump Coastdown — 6000 lb-ft^2 Pump Inertia

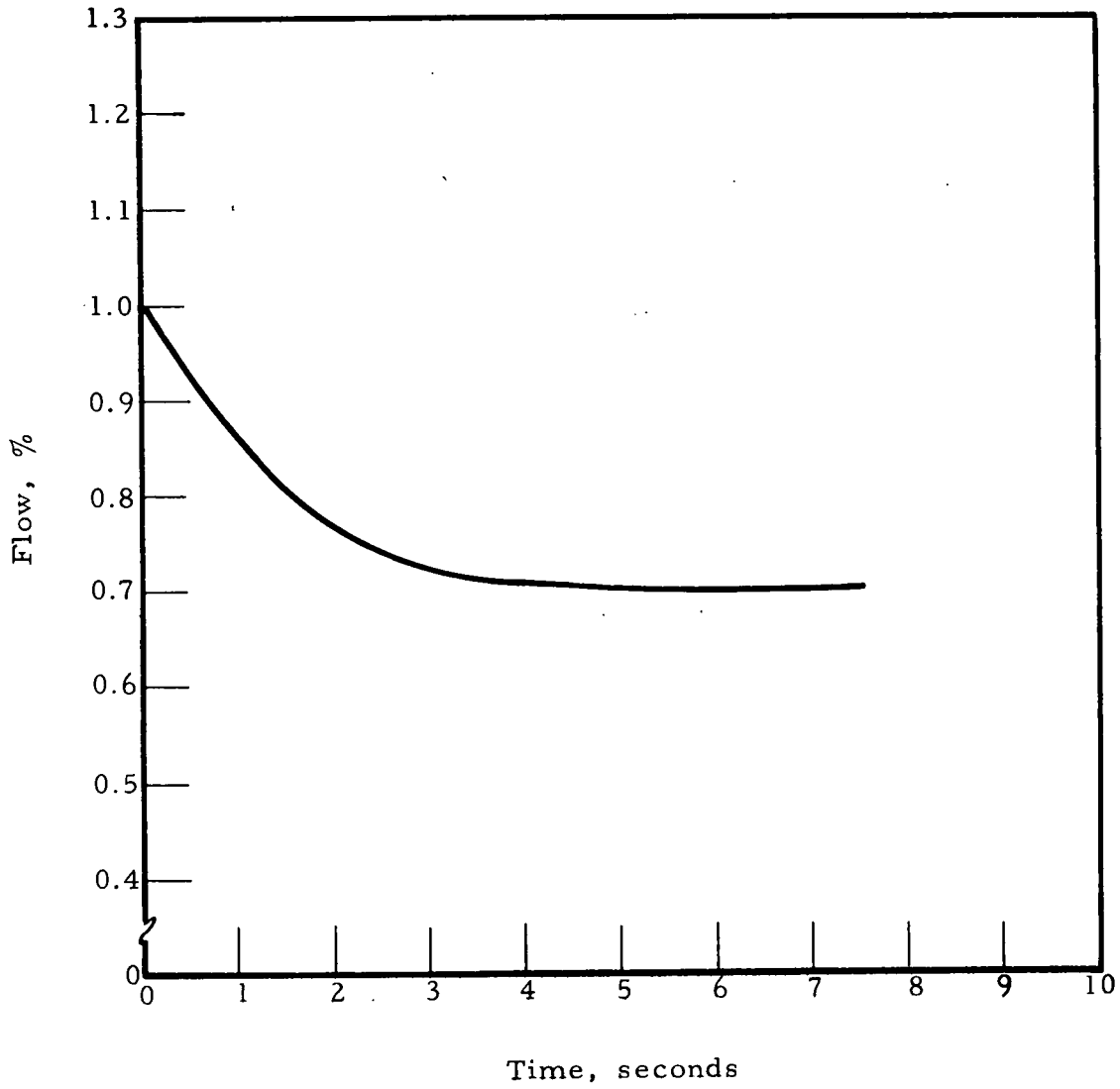

Figure 9. Power Trace — Nominal Coastdown, 15,000 lb-ft^2 Pump Inertia

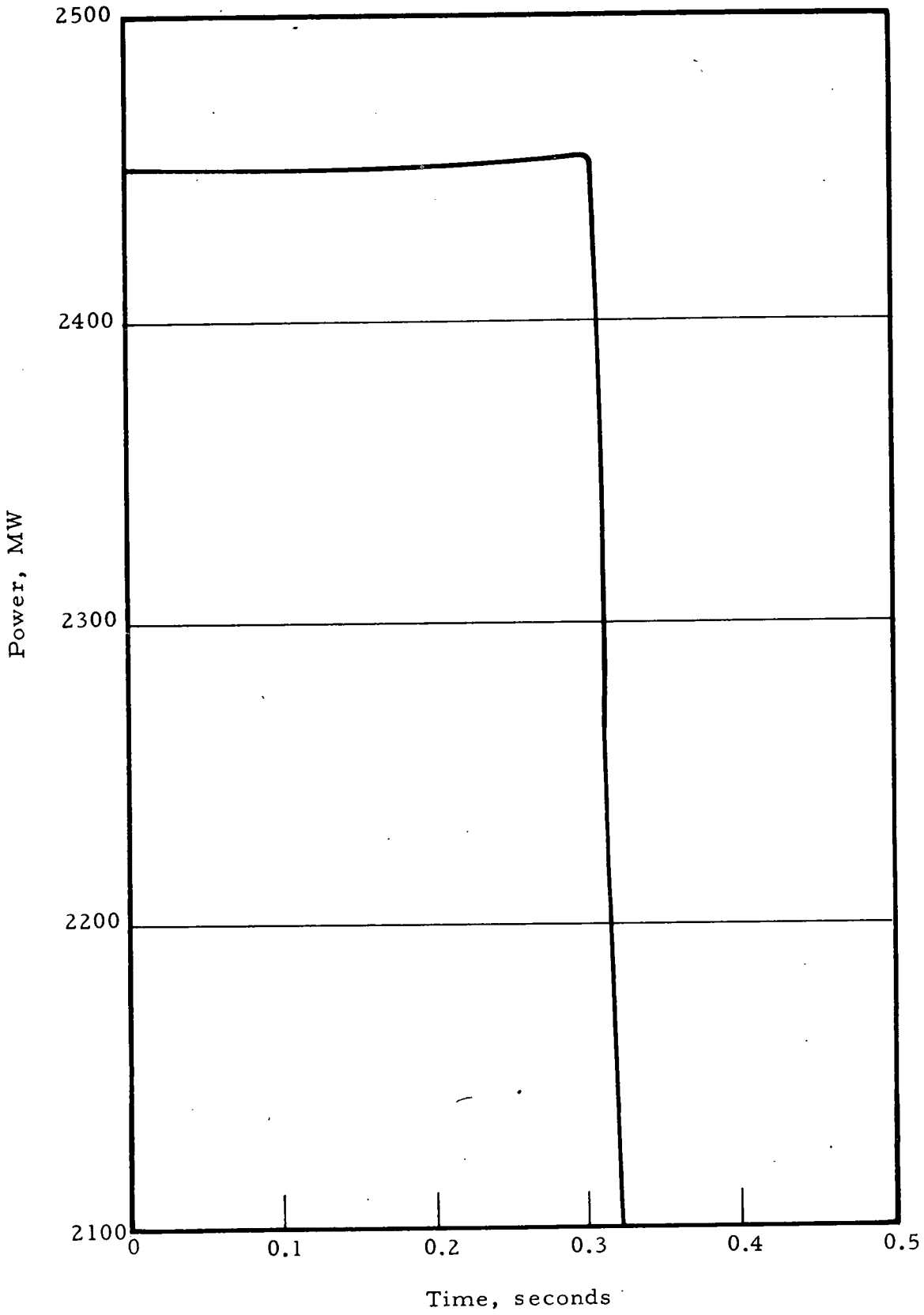

Figure 10. Power Trace — Nominal Coastdown, 6000 lb-ft^2 Pump Inertia

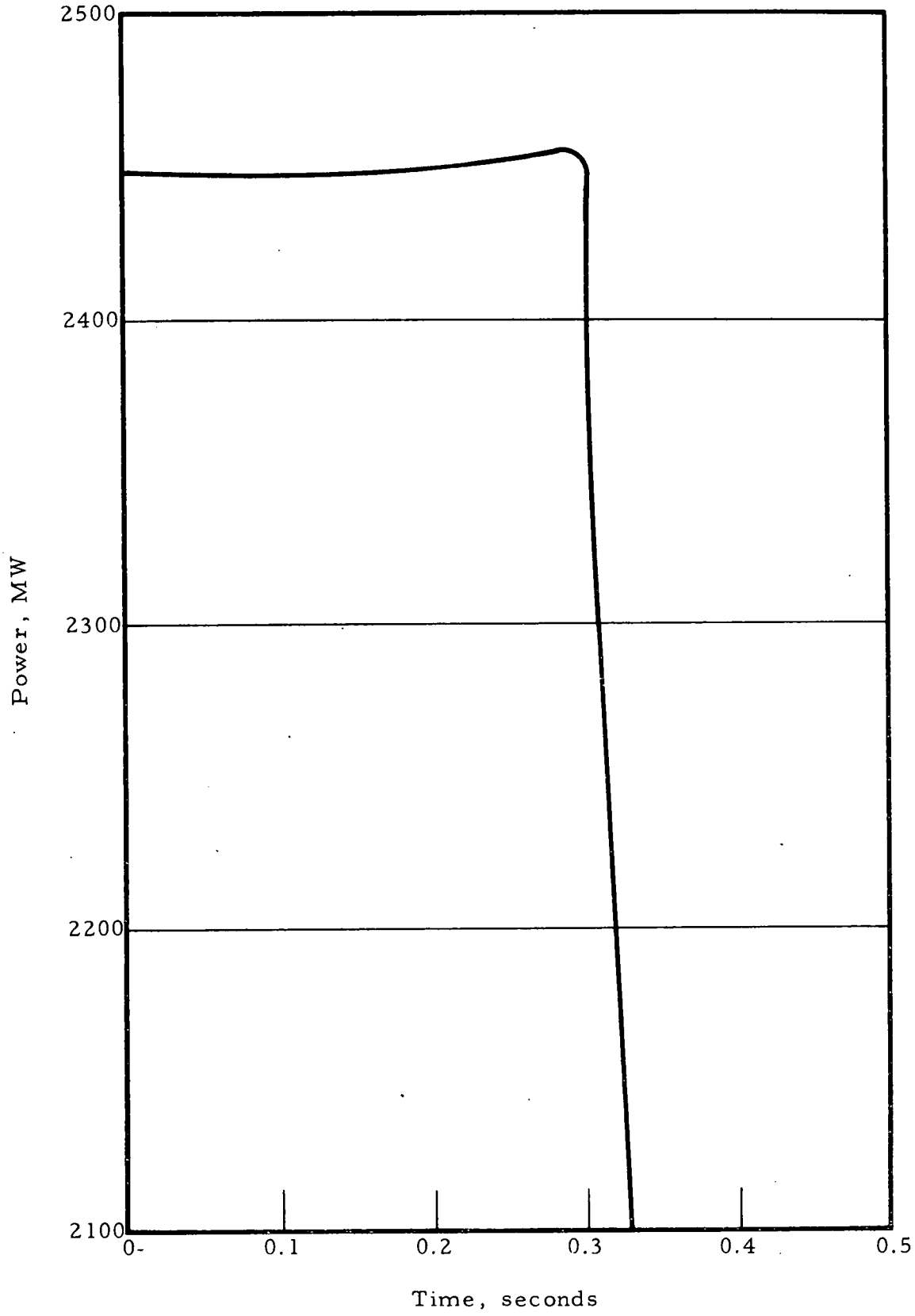

Figure 11. Power Trace — Nominal Two-Pump Coastdown, 6000 lb-ft^2 Pump Inertia

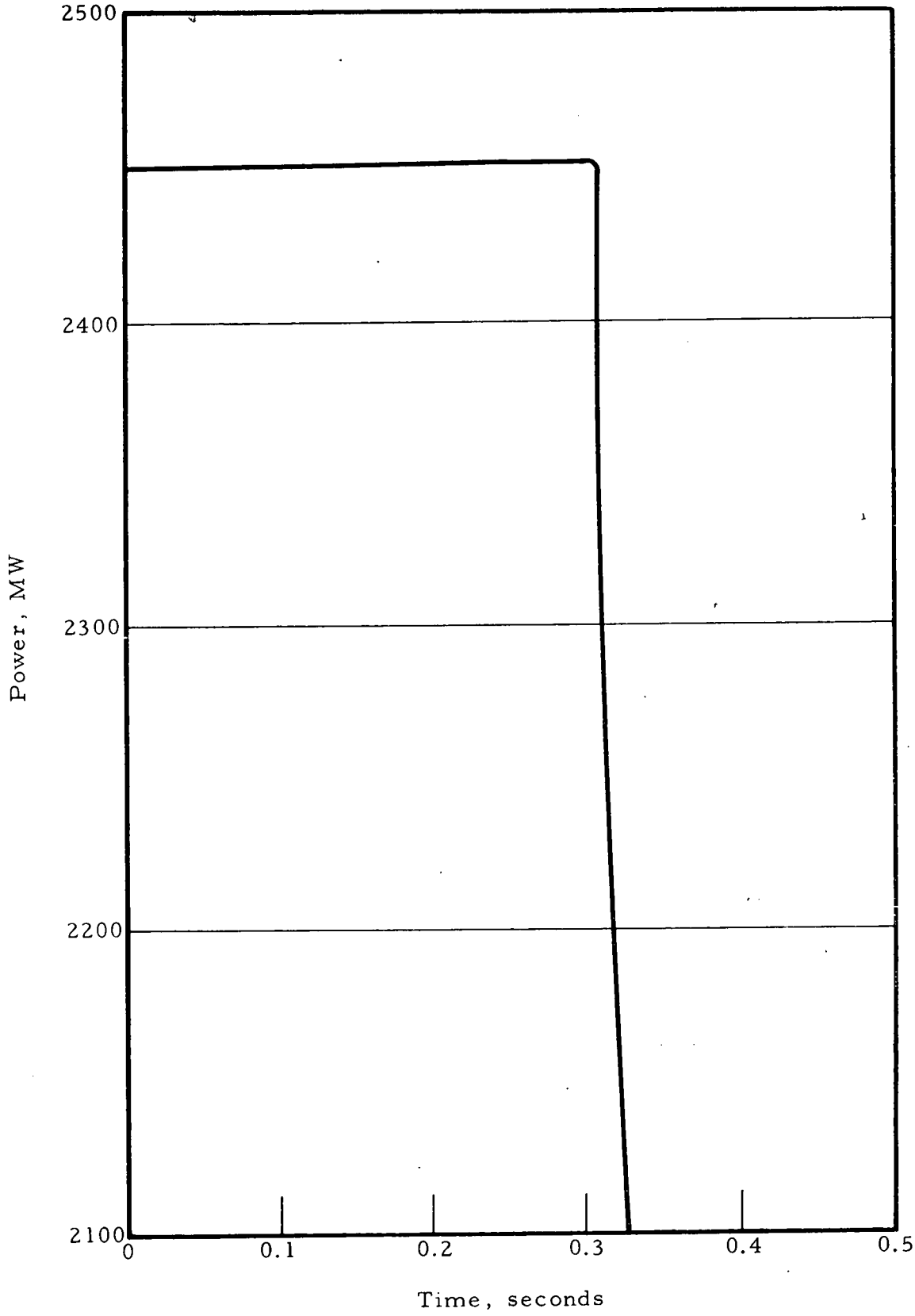

Figure 12. Power Traces — Six-Pump Flow Coastdown (15,000 lb-ft^2 Pump Inertia — No Central Void)

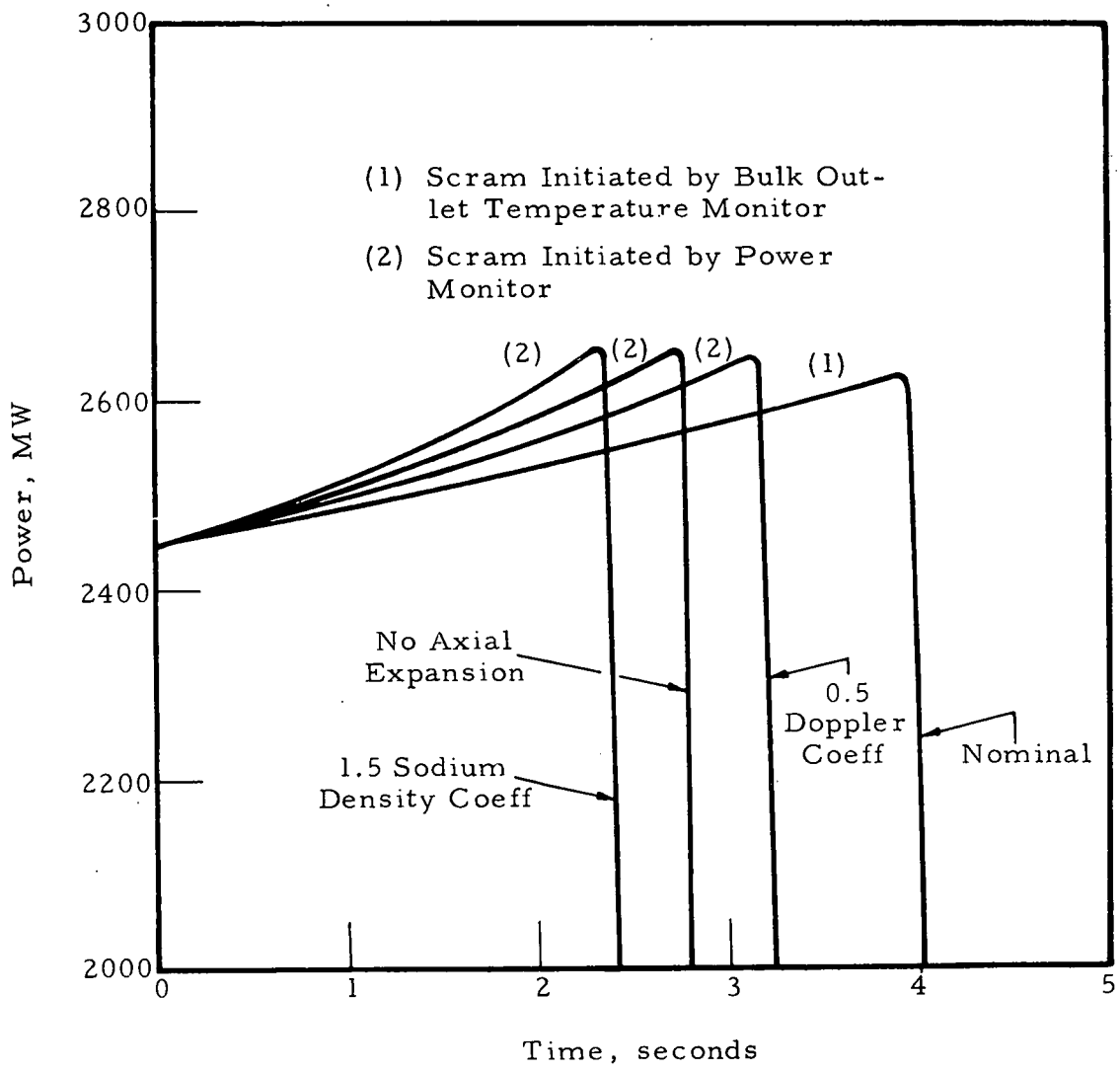

Figure 13. Cladding Temperature — Six-Pump Flow Coast-down (15,000 lb-ft^2 Pump Inertia — No Central Void)

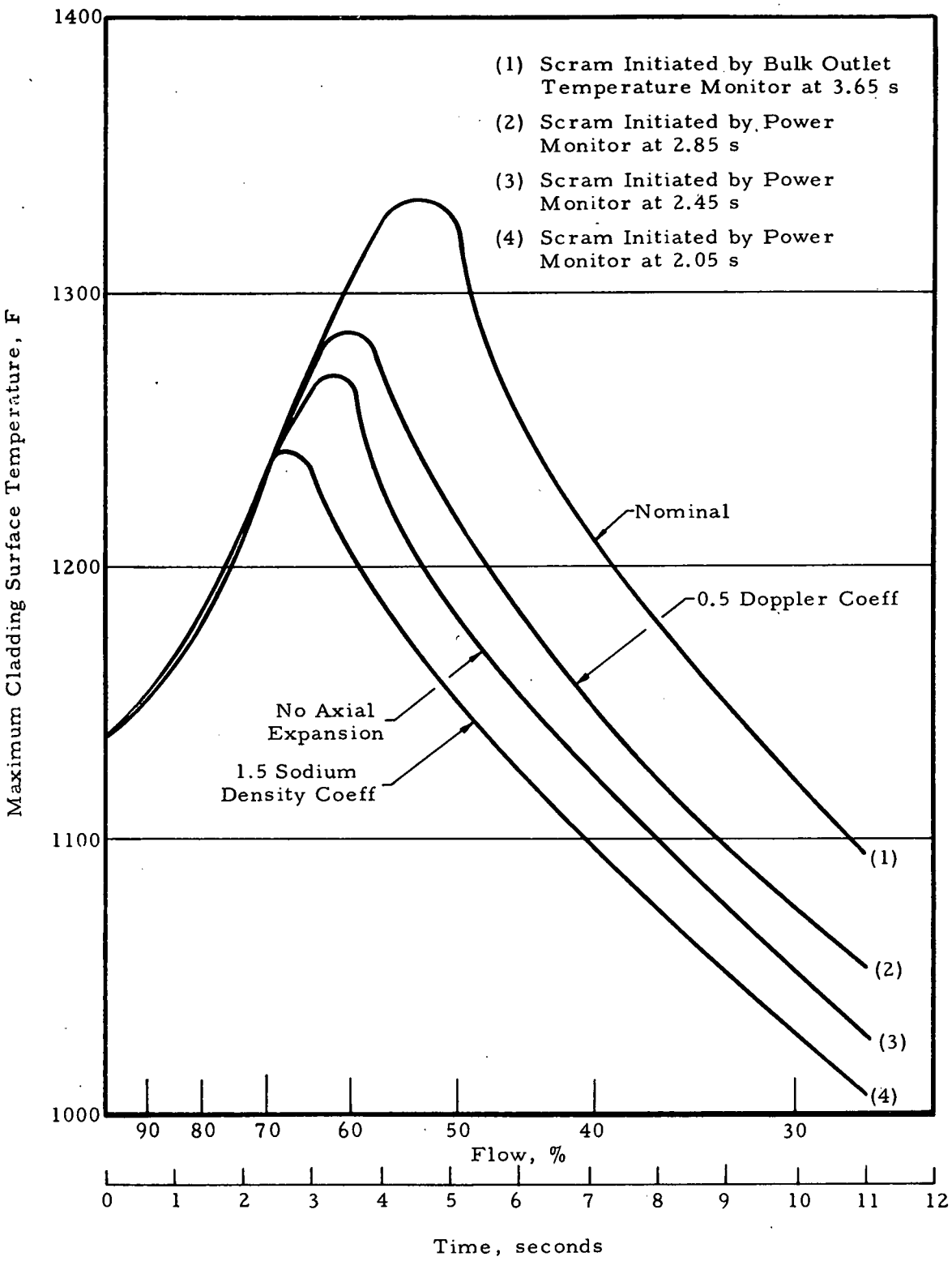

Figure 14. Power Traces — Six-Pump Flow Coastdown (6000 lb-ft^2 Pump Inertia — No Central Void)

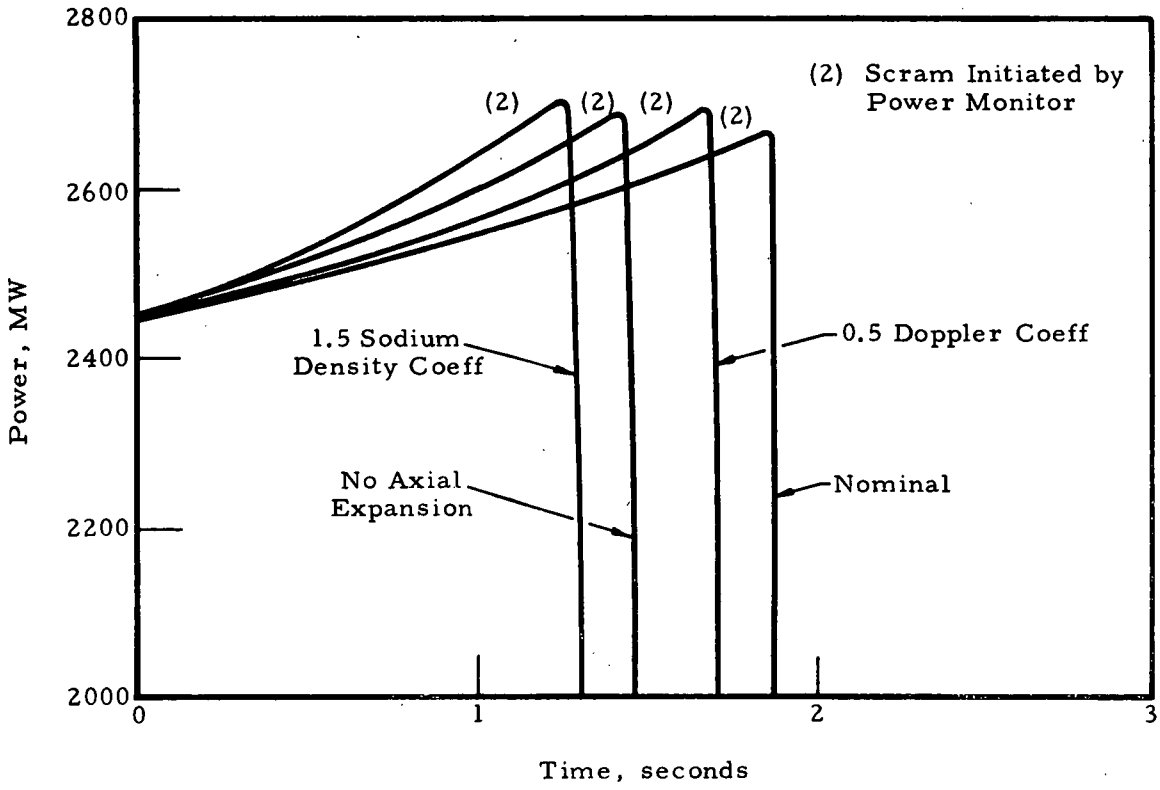

Figure 15. Cladding Temperature — Six-Pump Flow Coast-down (6000 lb-ft^2 Pump Inertia — No Central Void)

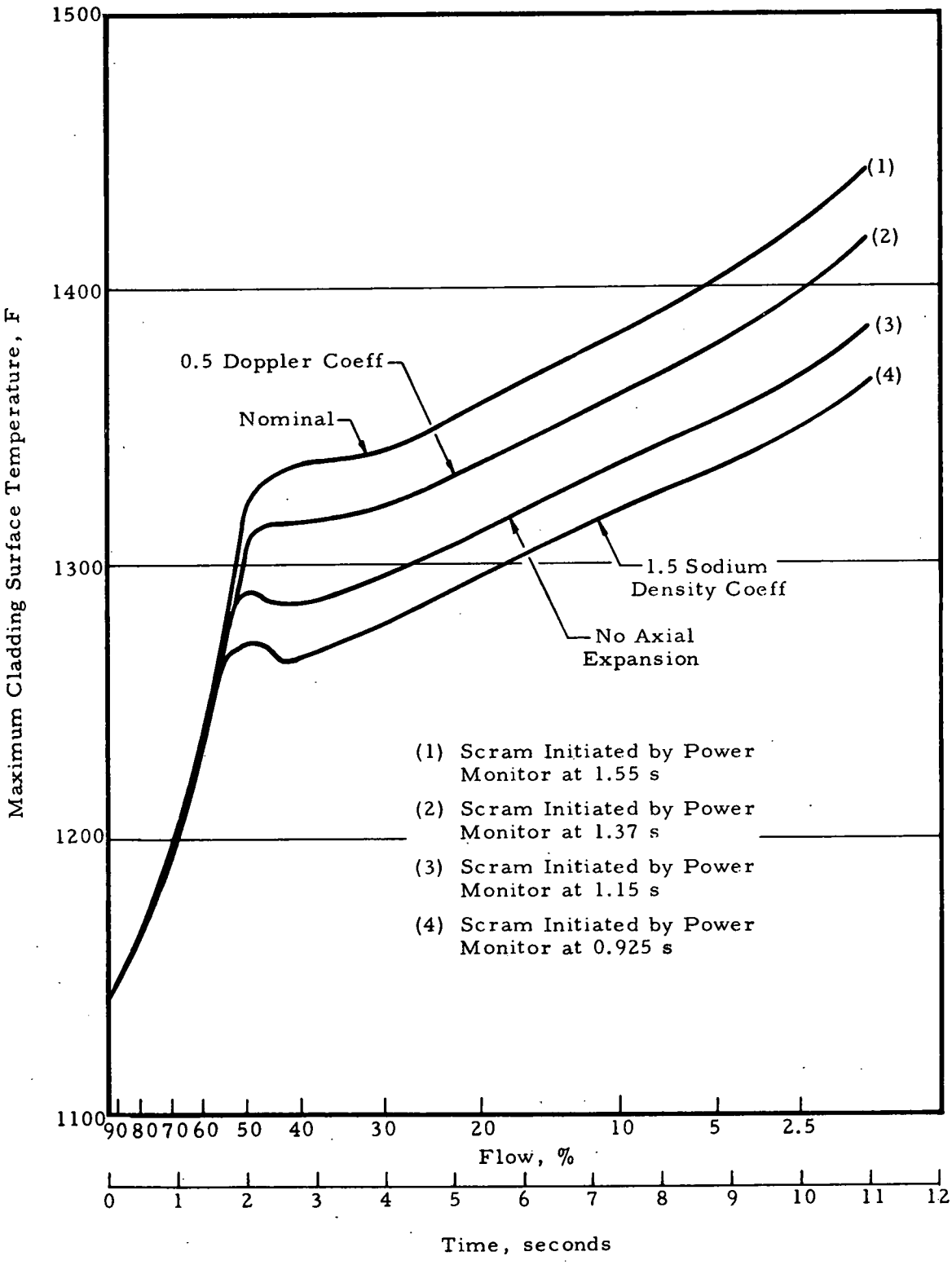

Figure 16. Power Traces — Six-Pump Flow Coastdown (15,000 lb-ft^2 Pump Inertia; Includes New K)

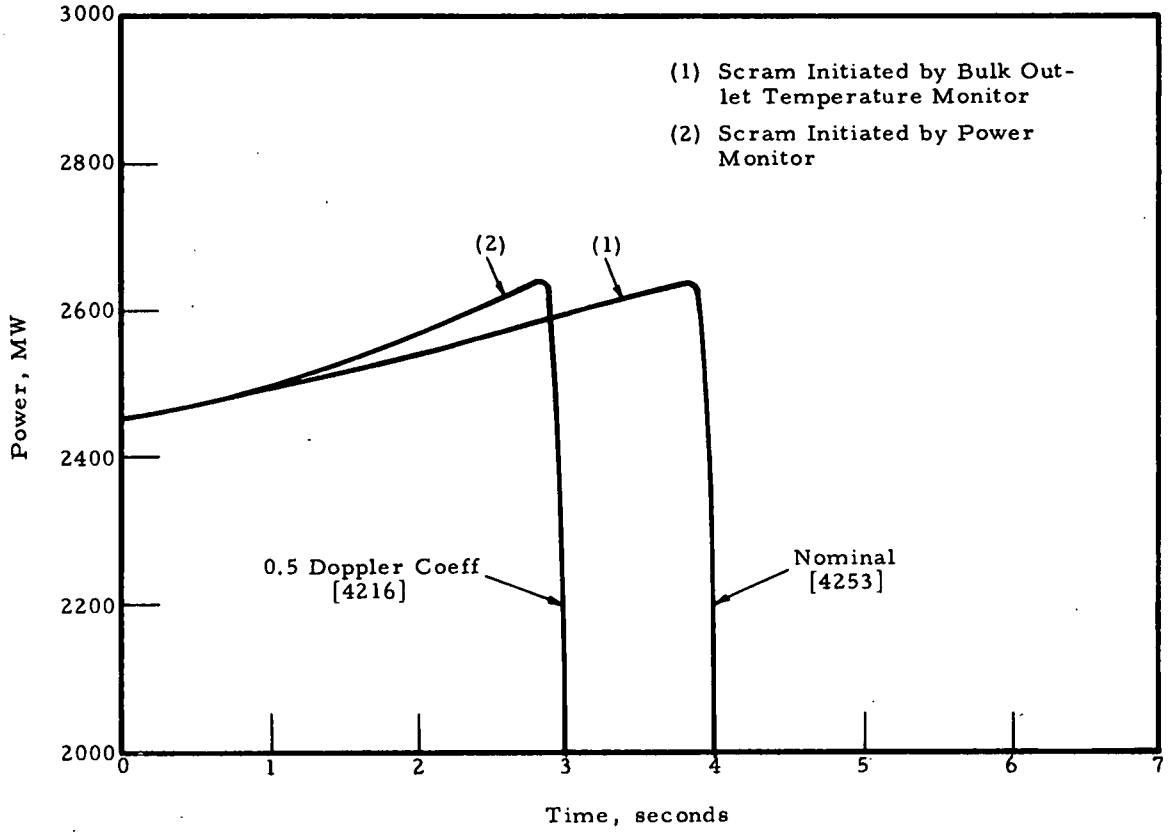

Figure 17. Centerline Fuel Temperature — Six-Pump Flow Coastdown (15,000 lb-ft^2 Pump Inertia — Hot Pin)

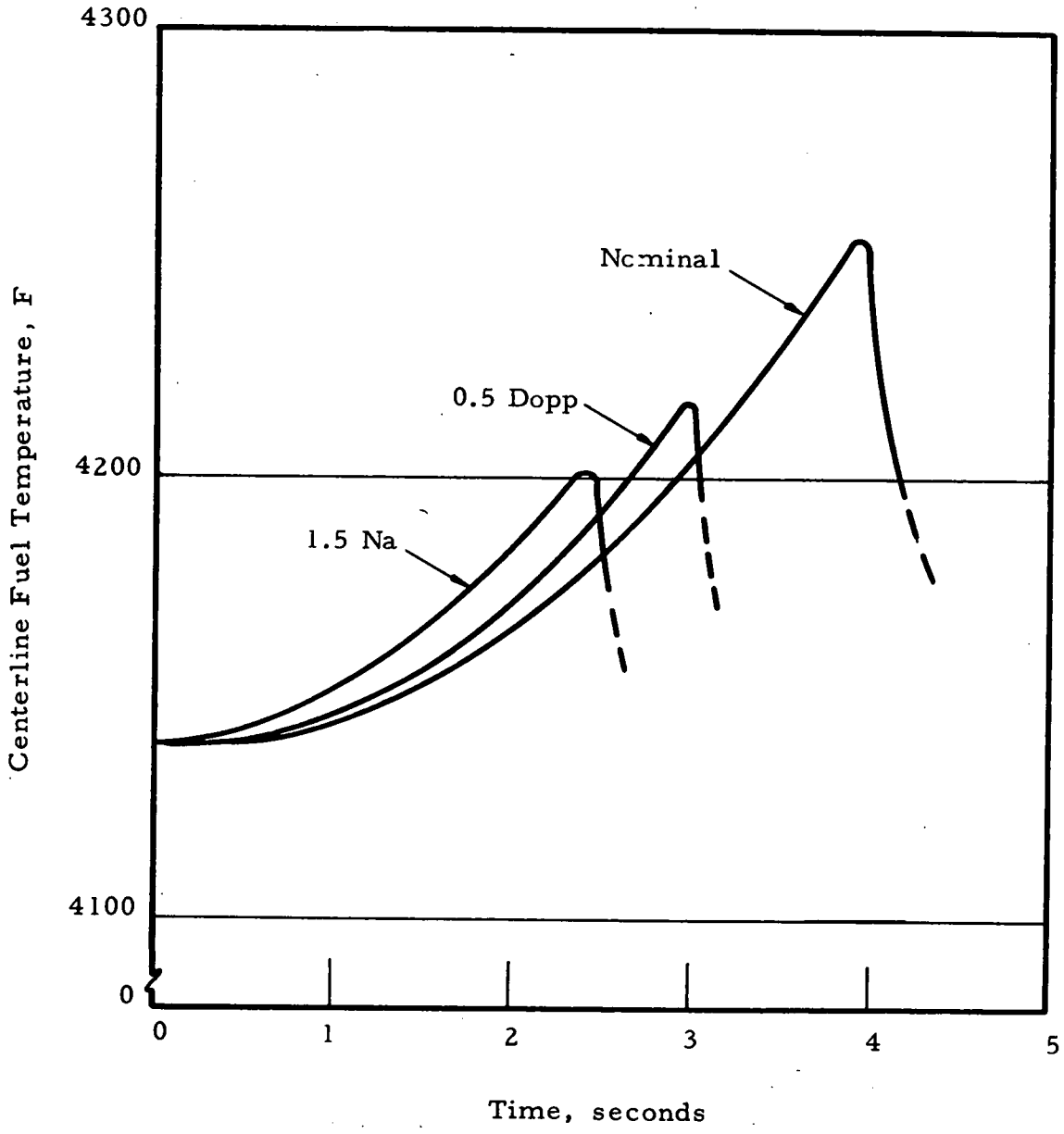

Figure 18. Cladding Temperature — Six-Pump Flow Coast-down (15,000 lb-ft^2 Pump Inertia — Hot Pin)

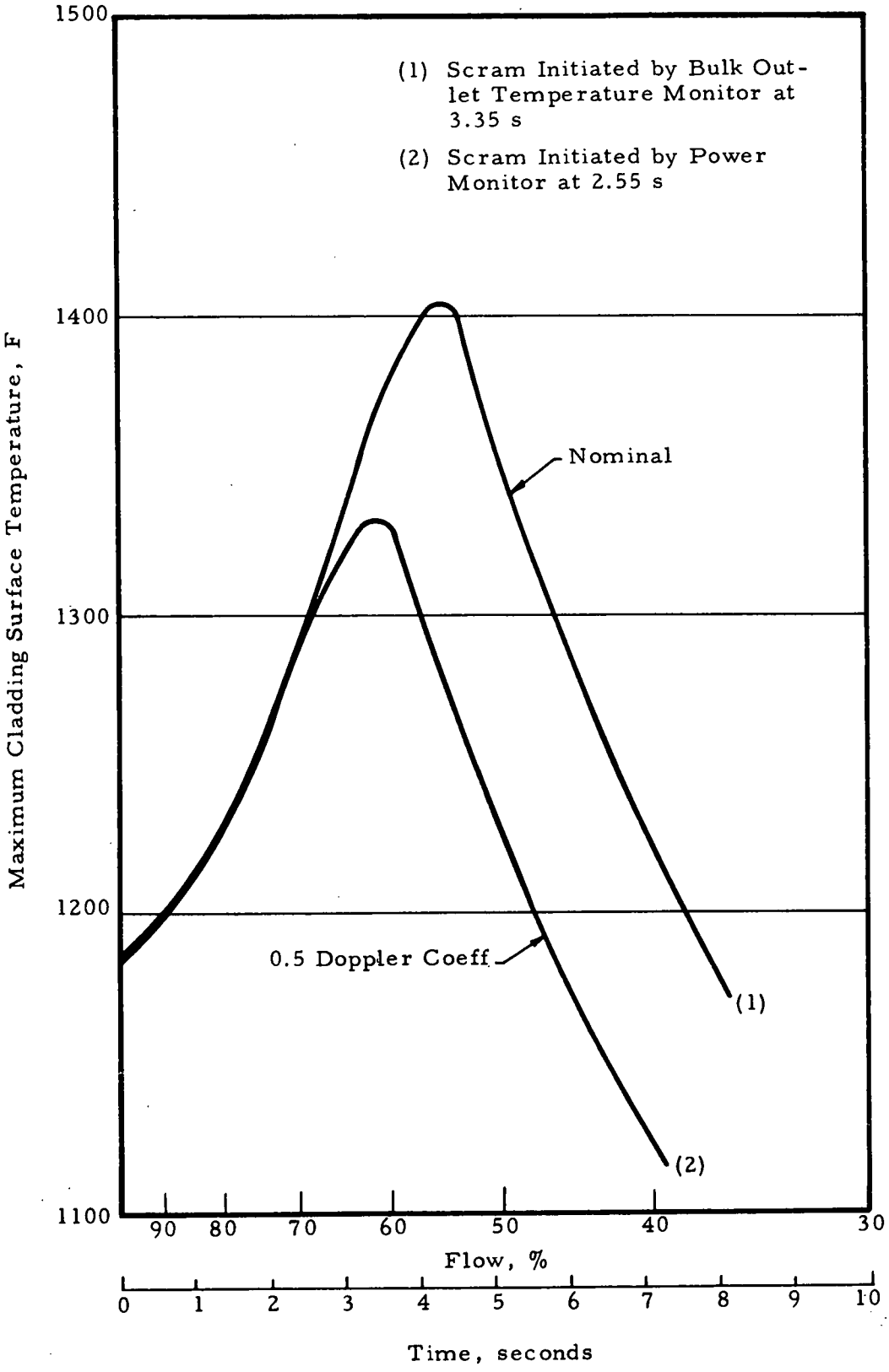

Figure 19. Power Traces — Six-Pump Flow Coastdown (6000 lb-ft^2 Pump Inertia; Includes New K)

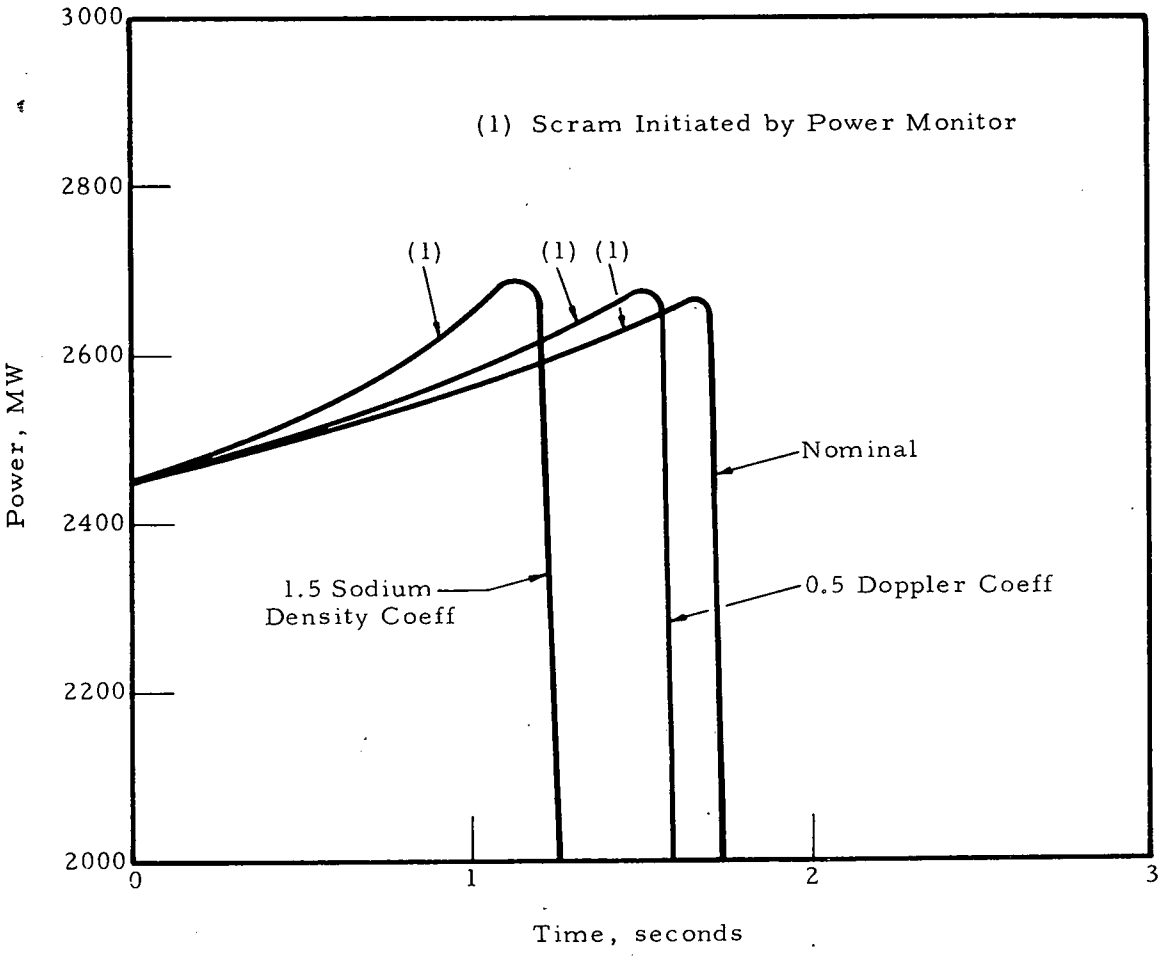

Figure 20. Centerline Fuel Temperature — Six-Pump Flow Coastdown (6000 lb-ft^2 Pump Inertia — Hot Pin)

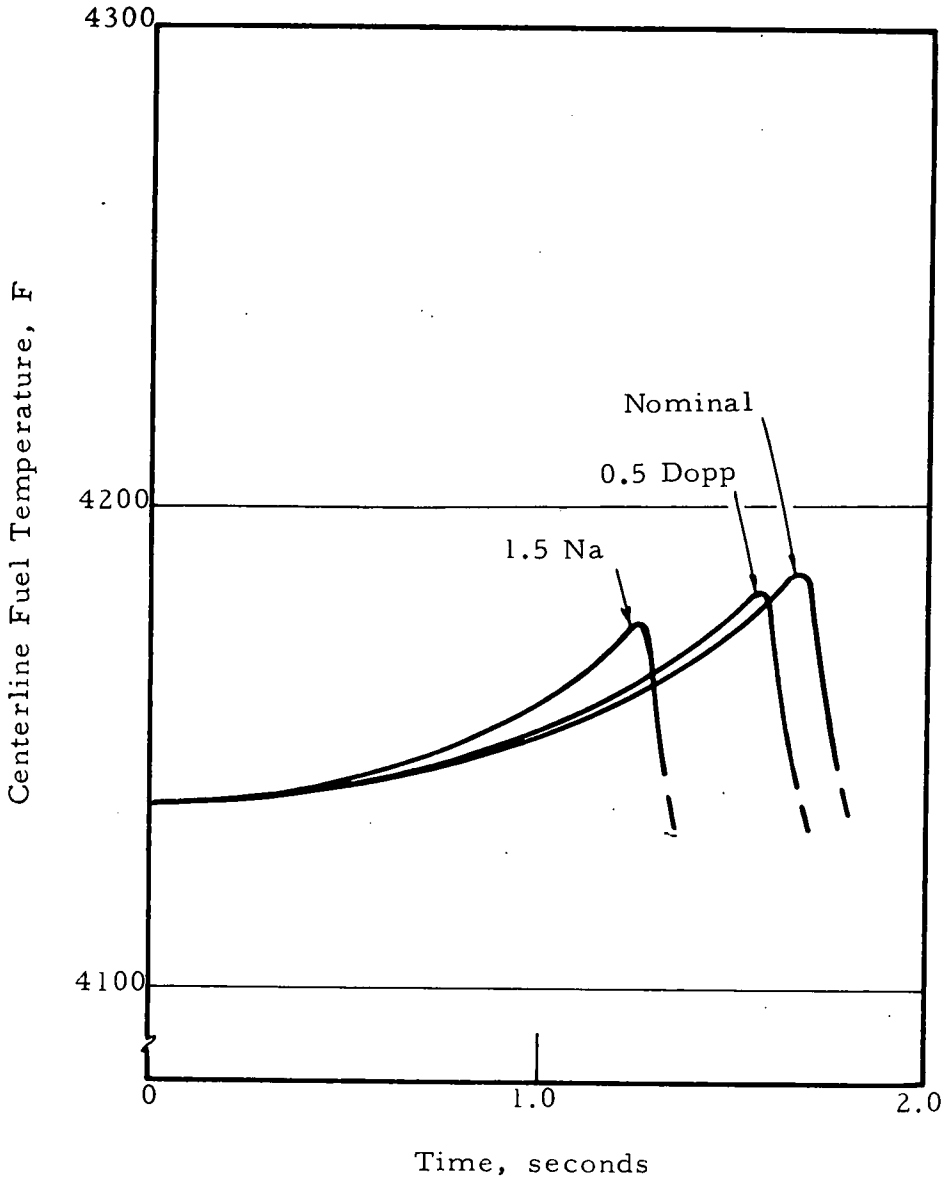

Figure 21. Cladding Temperature — Six-Pump Flow Coast-down (6000 lb-ft^2 Pump Inertia; Includes New K)

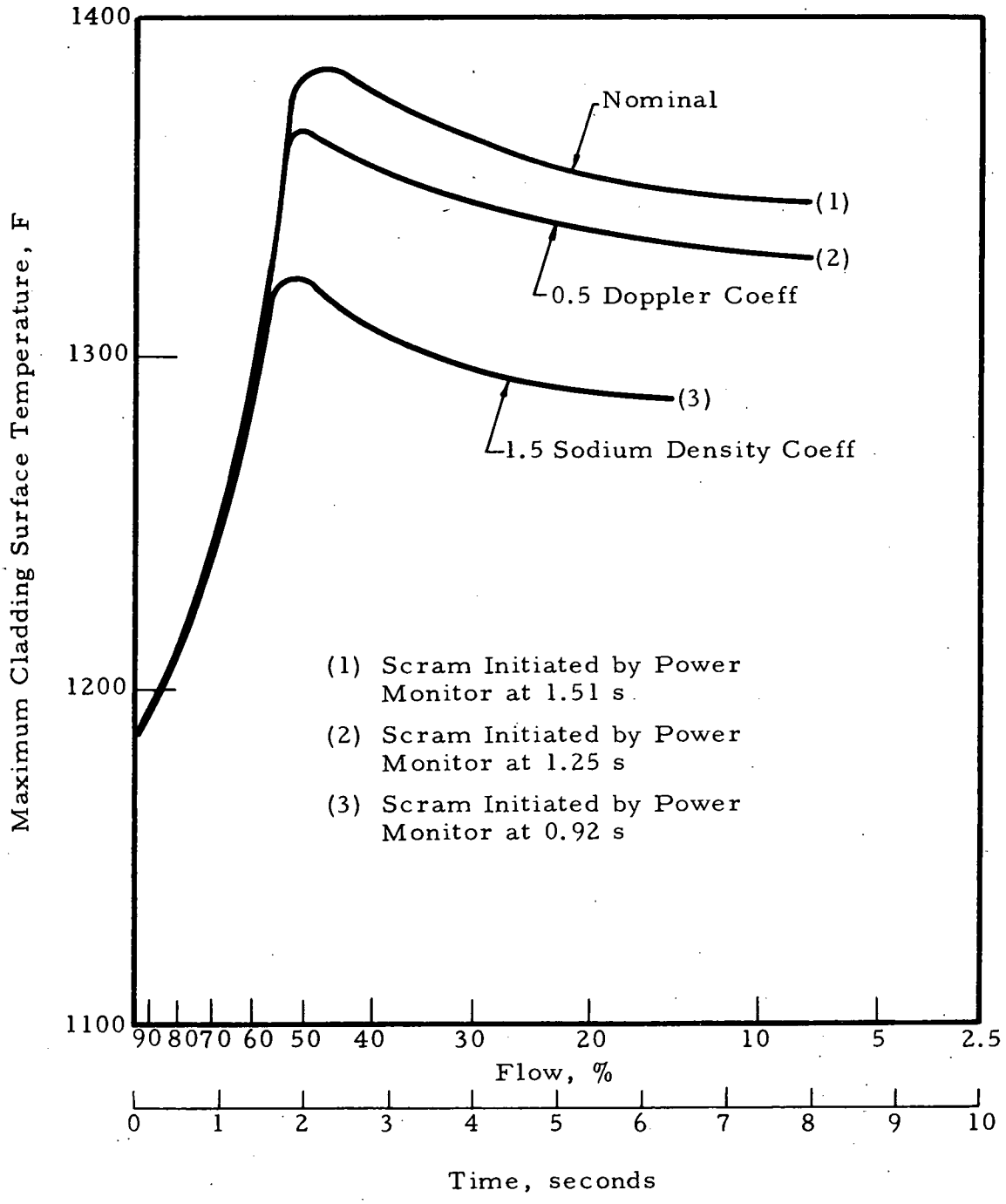

Figure 22. Reactor Response Vs Scram Delay — Six-Pump Flow Coastdown (6000 lb-ft^2 Pump Inertia)

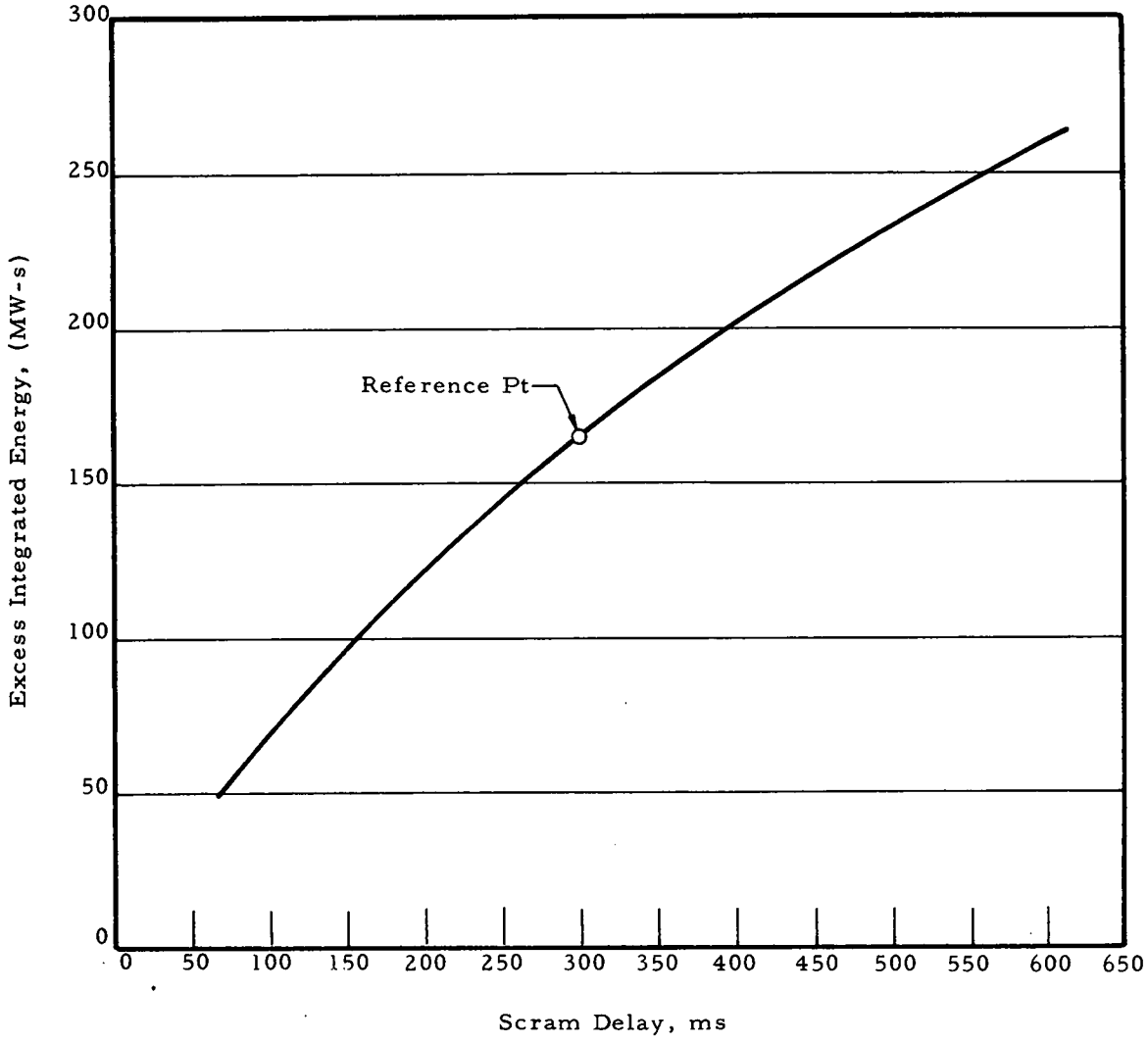

Figure 23. Reactor Response Vs Scram Reactivity

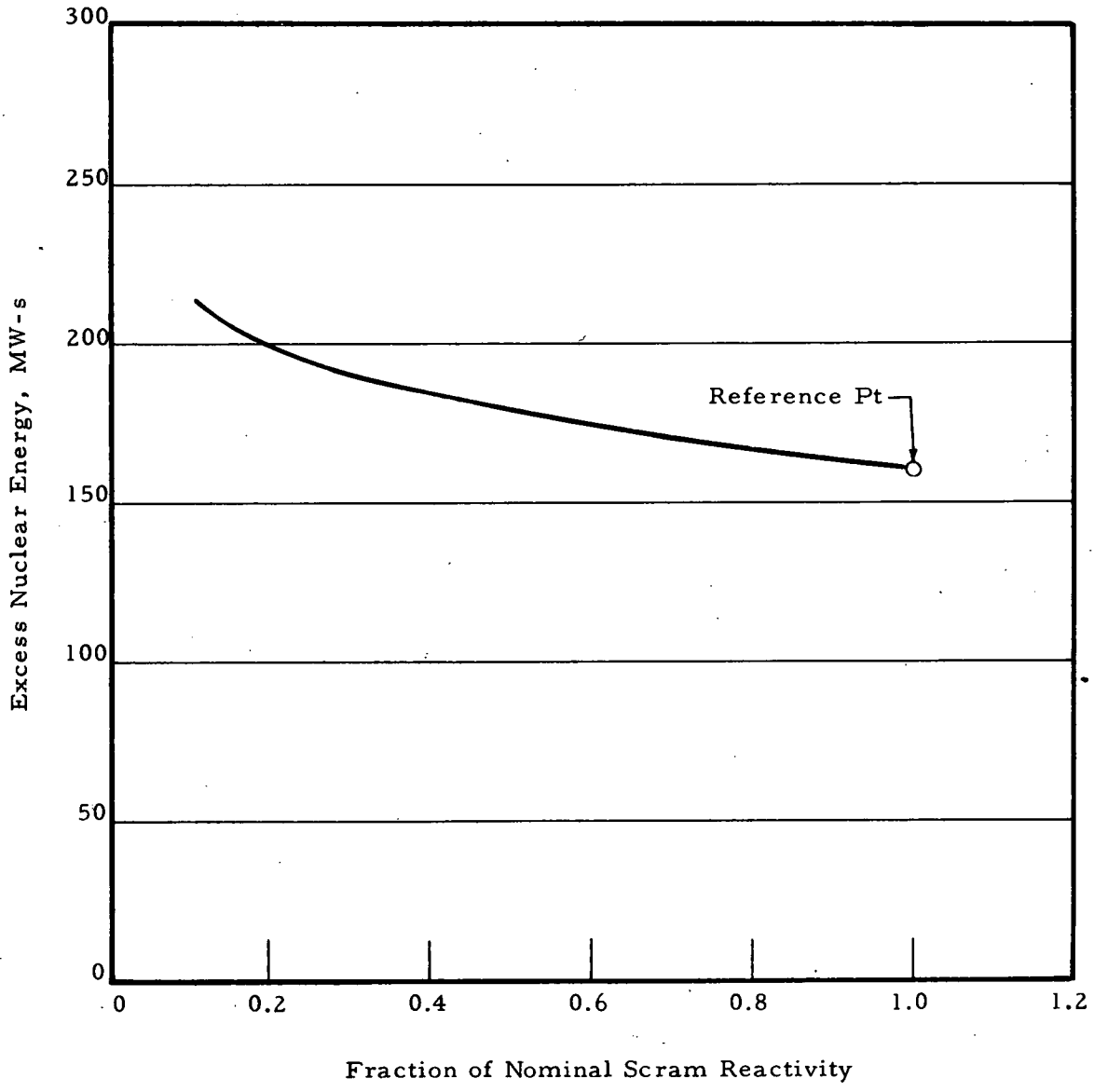

Figure 24. Power Trace — Two-Pump Coastdown (6000 lb-ft^2 Pump Inertia — No Scram)

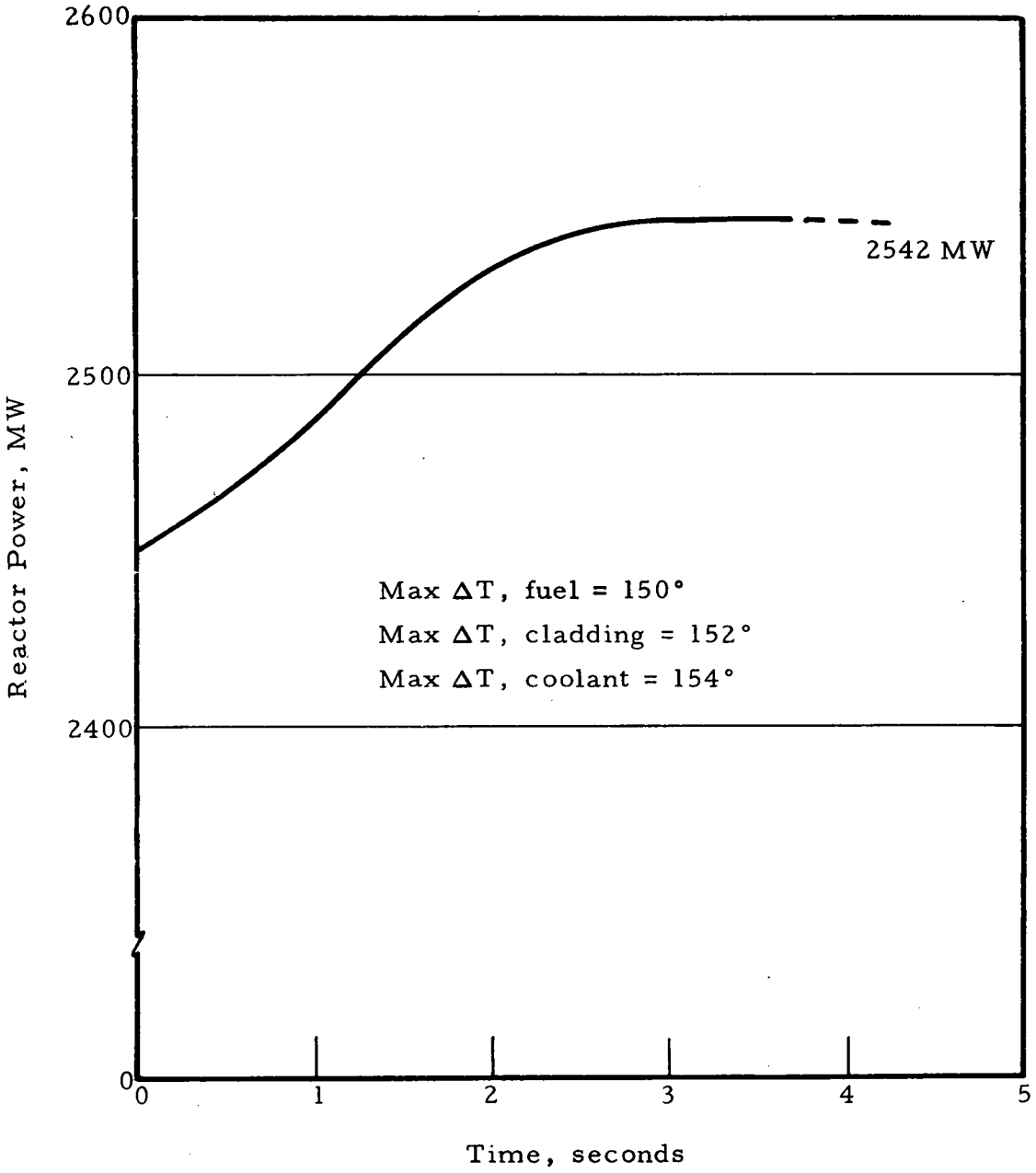

Figure 25. Power Trace — Double-Ended Pipe Break (Transient Time = 0.01 s)

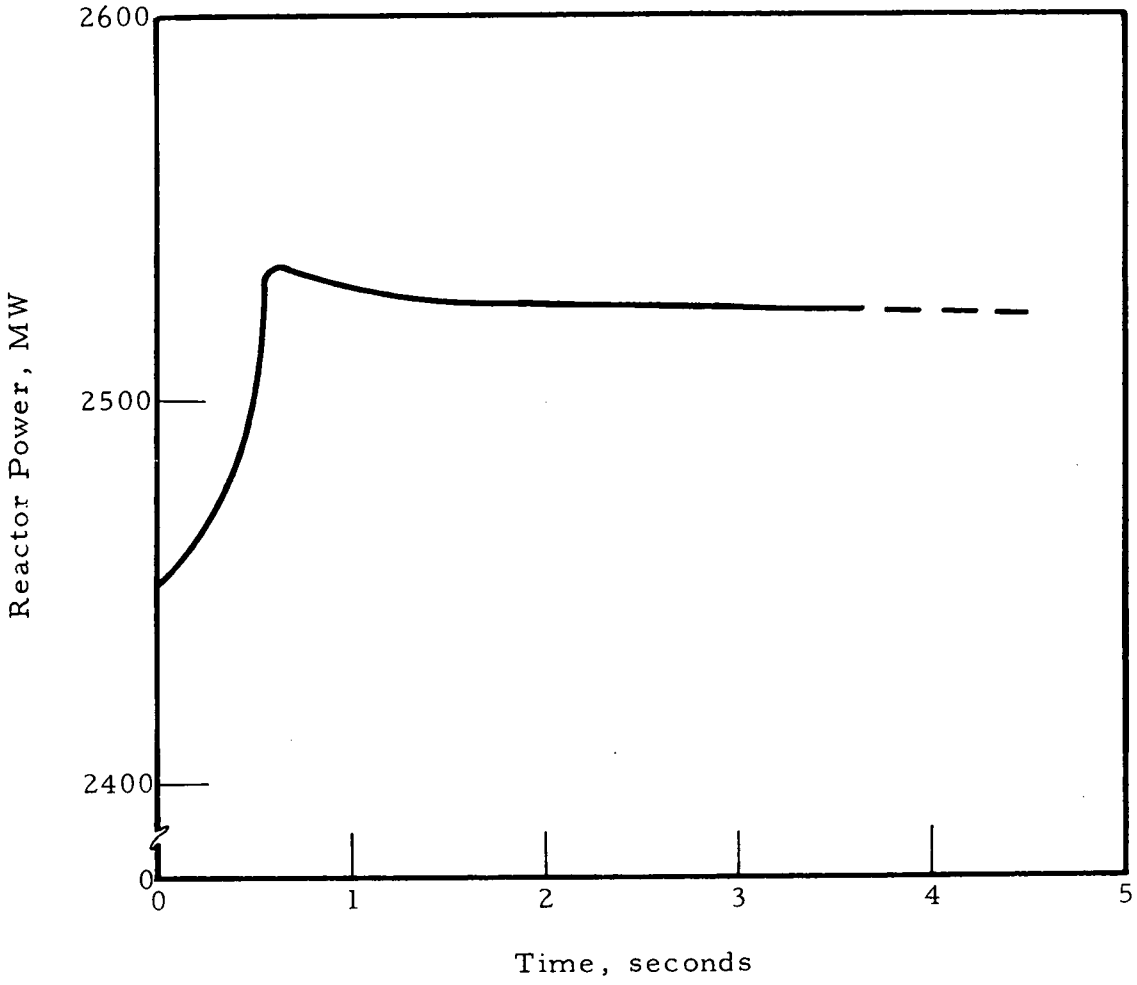

Figure 26. Effect of Coolant Channeling With Axial Expansion Feedback

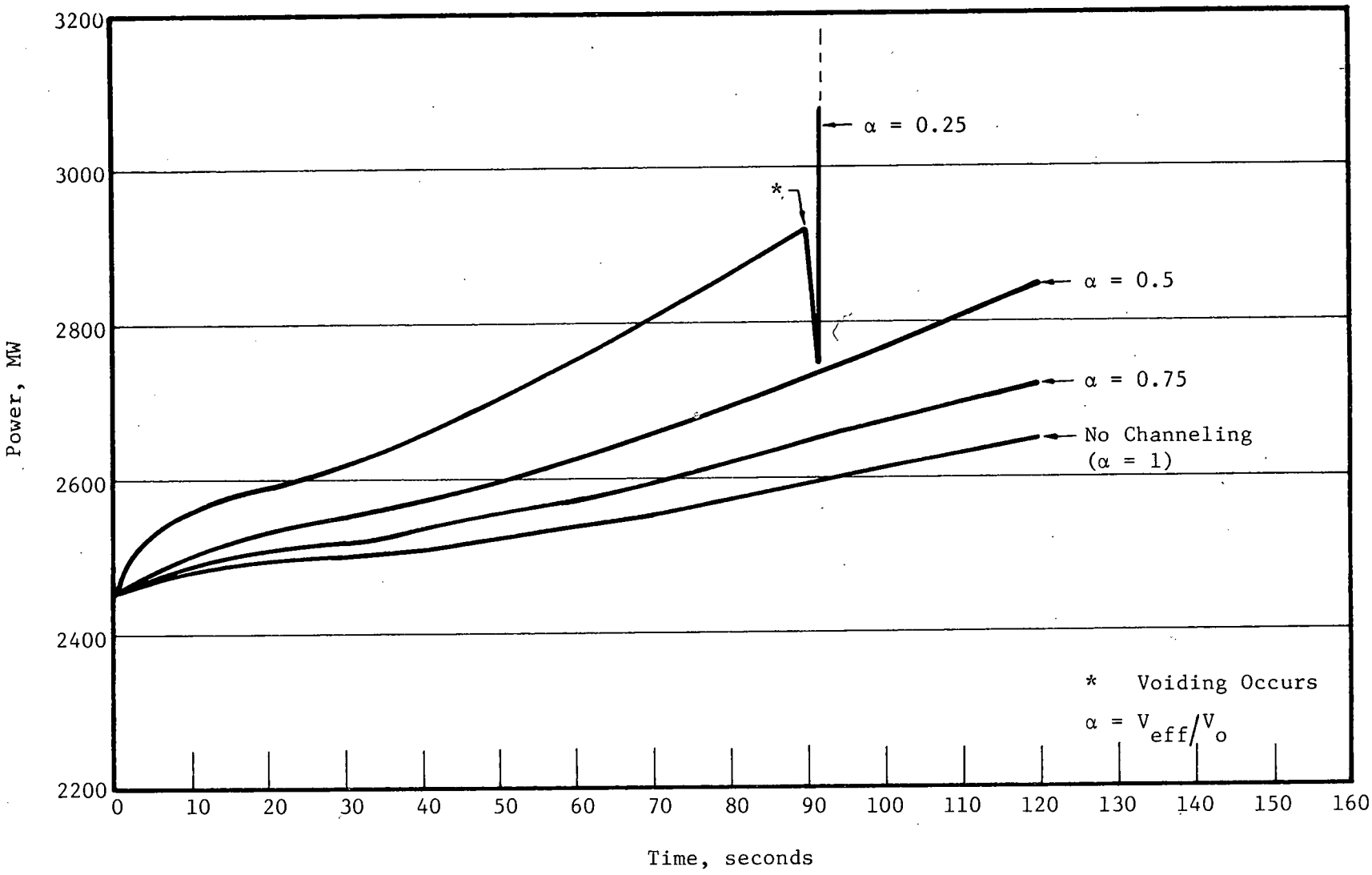

Figure 27. Molten Fuel Fractions — Loss of Heat Sink With Axial Expansion

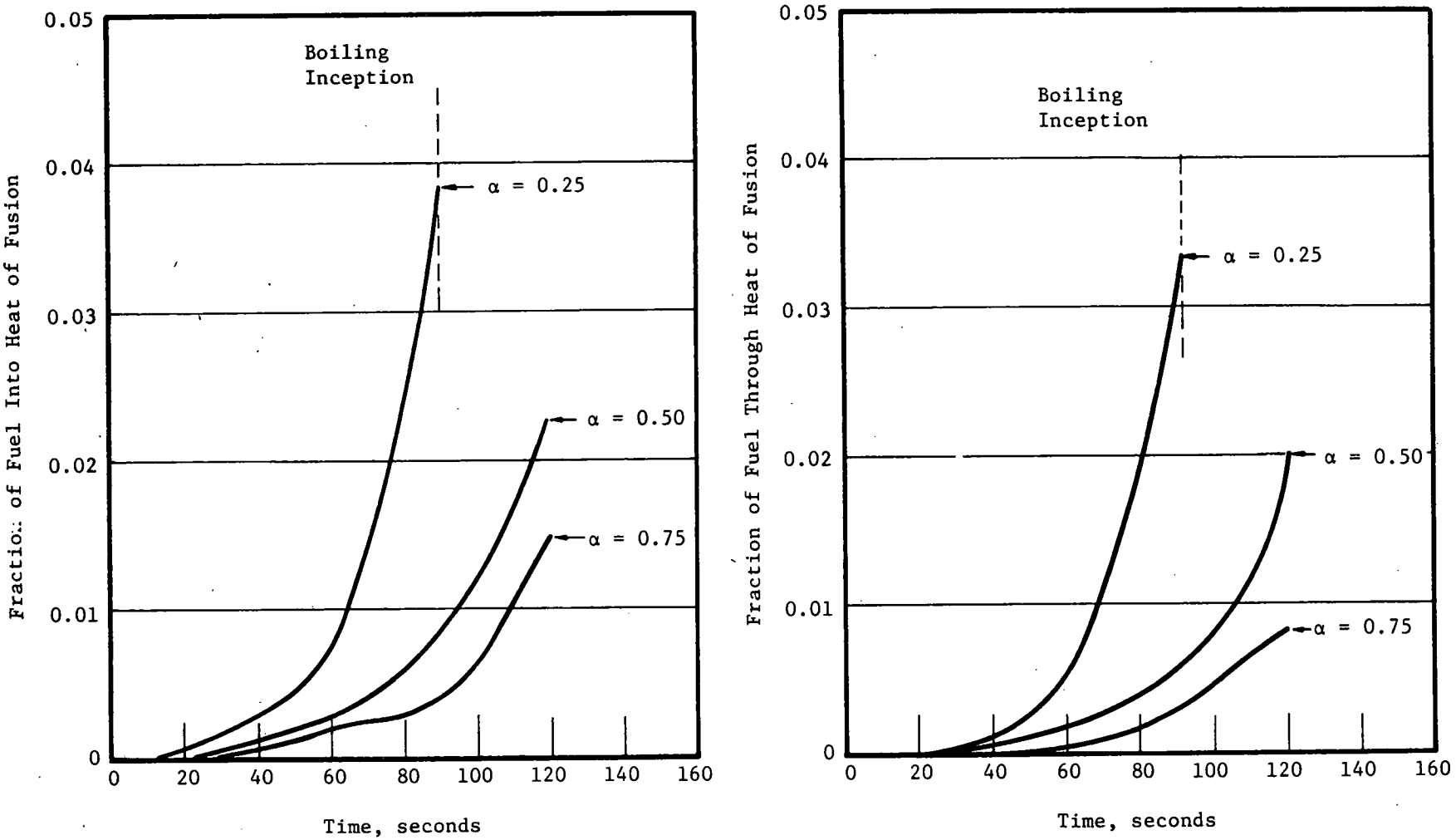

Figure 28. Coolant Outlet Temperature — Loss of Heat Sink, Various Degrees of Channeling

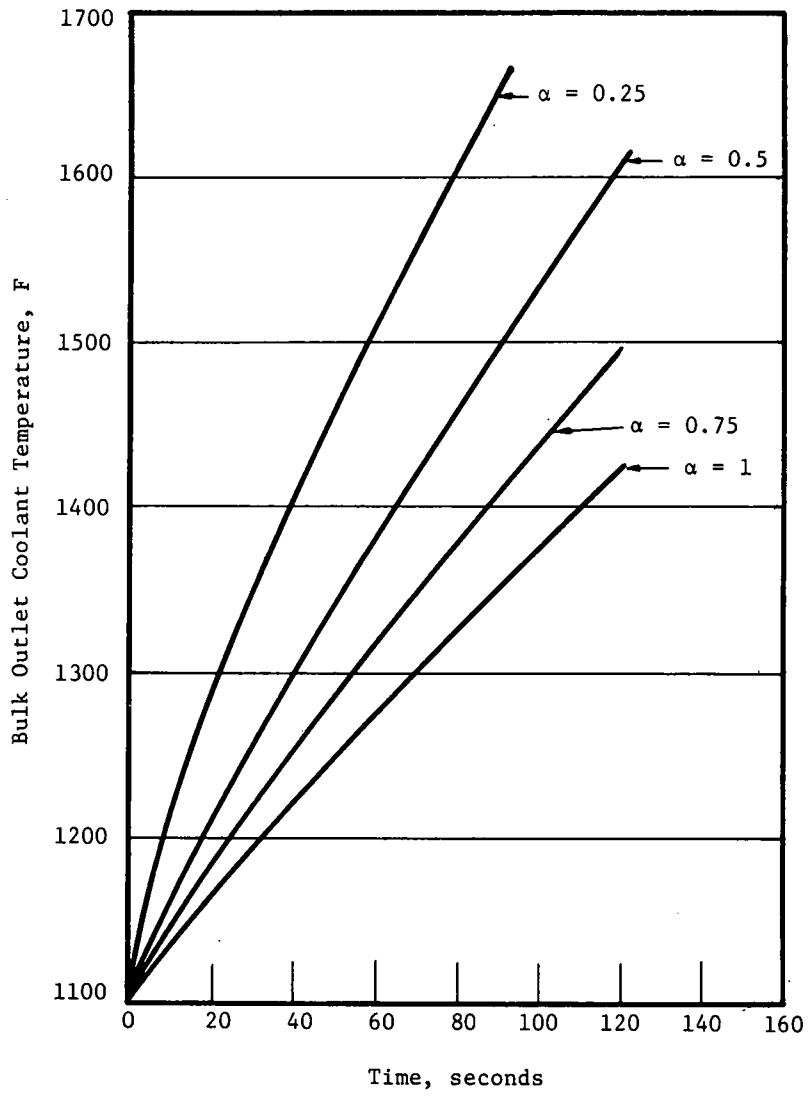

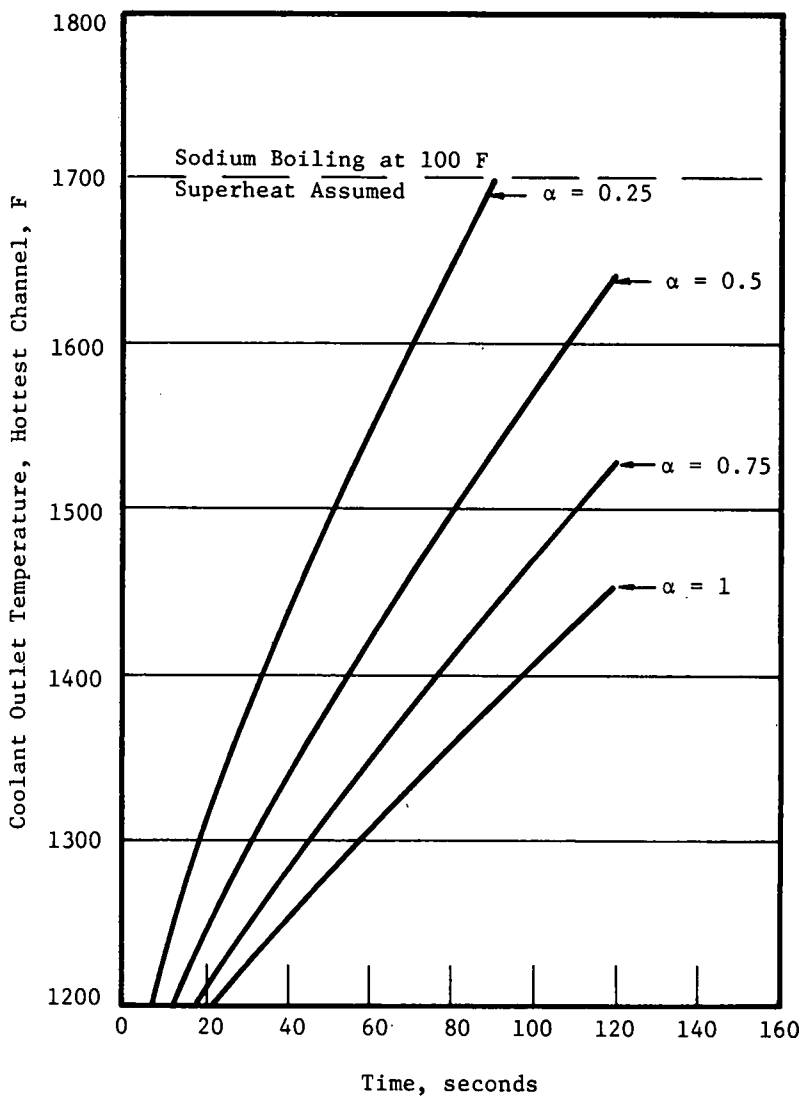

Figure 29. Cladding Temperatures — Loss of Heat Sink

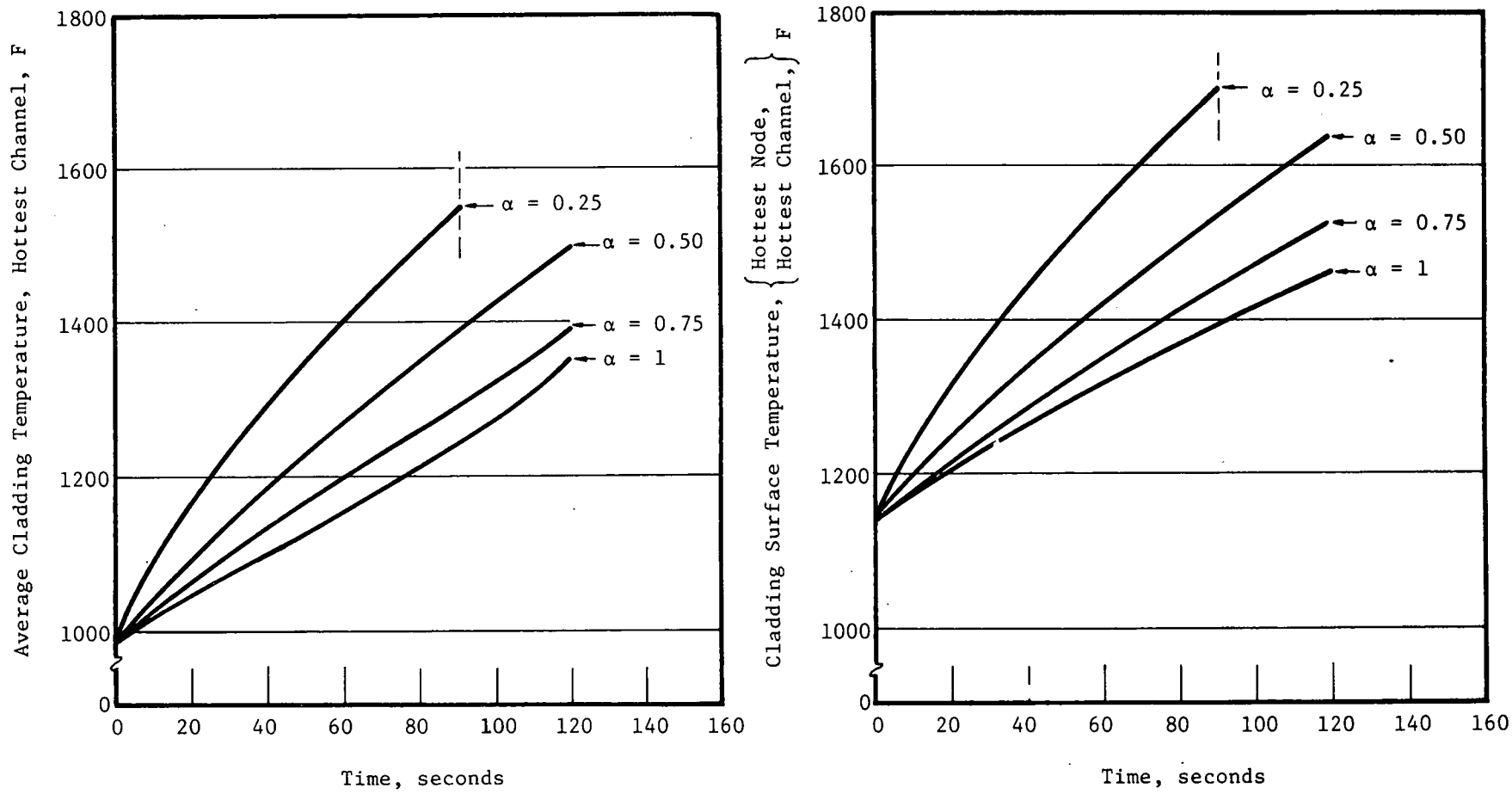

Figure 30. Maximum Fuel Temperatures — Loss of Heat Sink

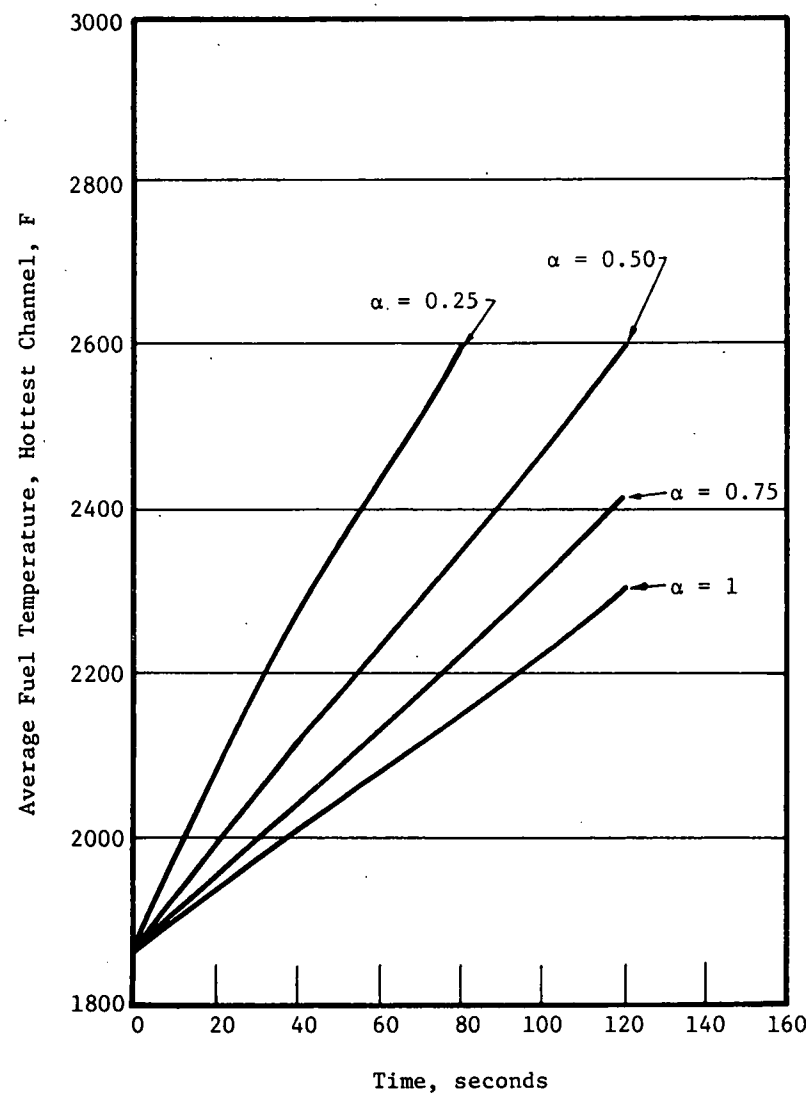

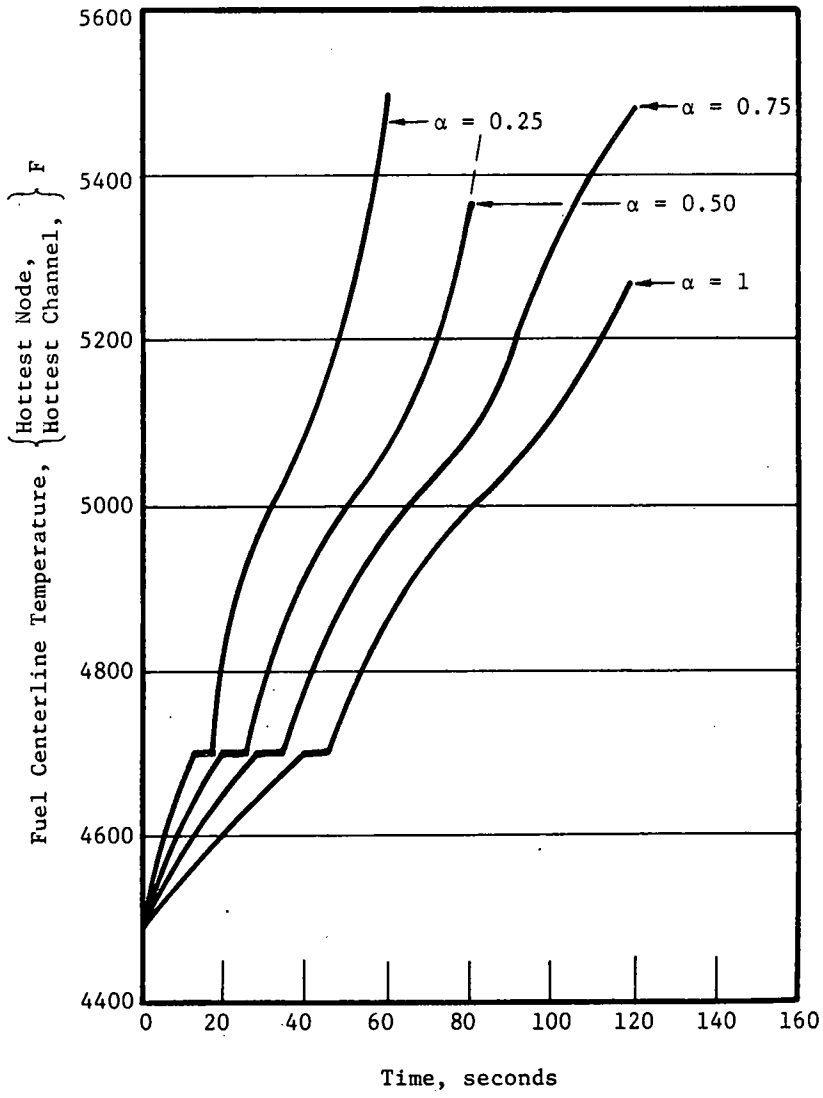

Figure 31. Effect of Axial Expansion Feedback, Perfect Mixing in Inlet Plenum

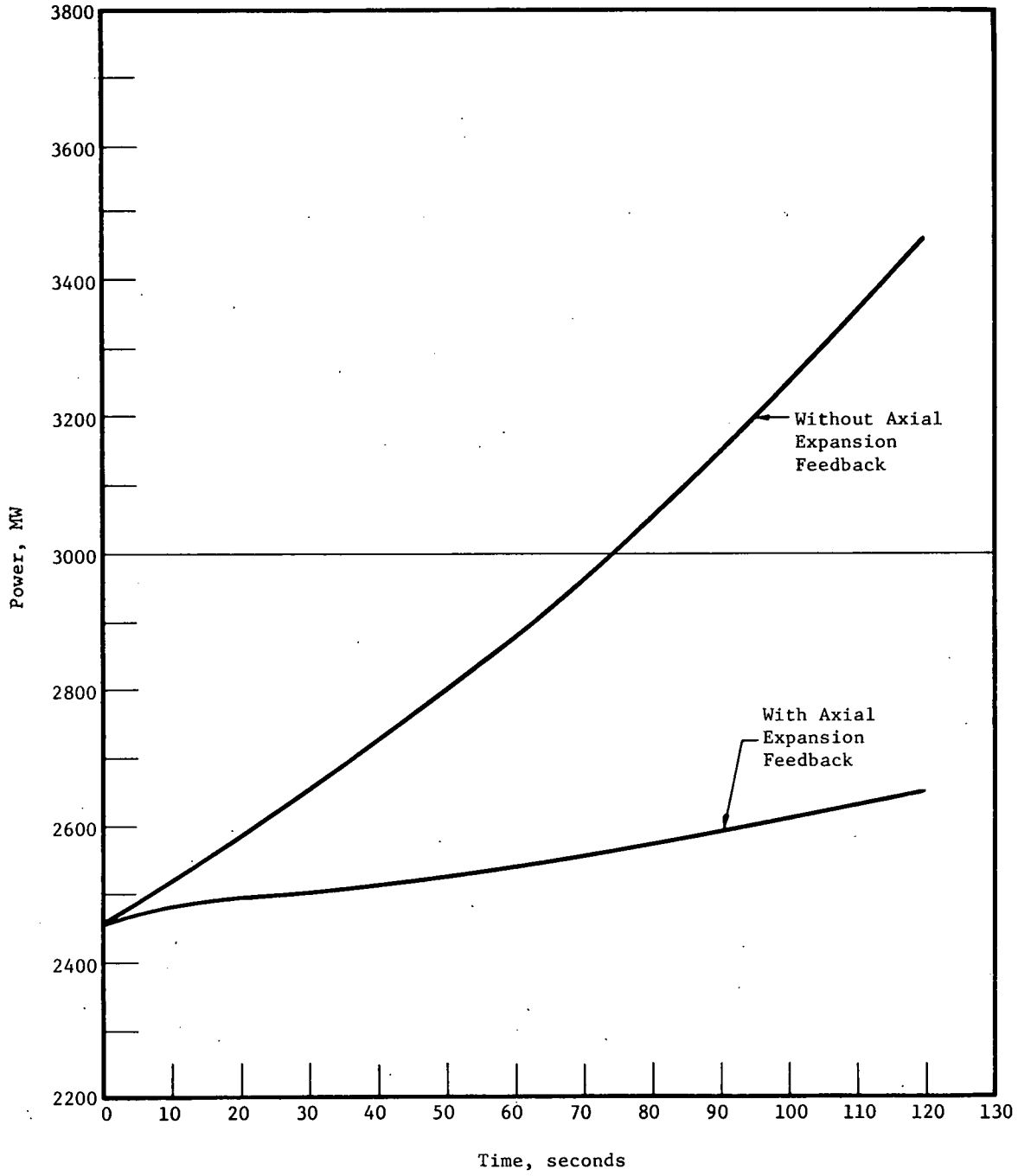

4. EVALUATION

The ultimate goal of the Accident Analysis and Safety System Design Study is the selection of a design basis accident and a conceptual design for protective systems and safety features. To this end, certain malfunctions affecting coolant flow have been investigated. The results indicate that the condition arising from definable malfunctions with the reactor at power will not lead to irreversible damage of the fuel, core, or components unless at least partial failure of the protection system is postulated. In most instances, at least three independent, simultaneous failures are required before irreversible damage occurs; this means, of course, that such events are extremely unlikely. The implication for the Study is that flow abnormalities are effectively removed from the category of initiating conditions likely to lead to a serious accident or a DBA.

Although failure of the protection system is deemed incredible, certain accidents arising from failure of the protection system coupled with flow abnormalities will be investigated under Activity 220, Accident Analysis.

REFERENCES

[1] 1000-MWe LMFBR Follow-On Study, Babcock & Wilcox, BAW-1328, Vol 1, Lynchburg, Virginia, March 1969.

[2] 1000-MWe LMFBR Accident Analysis and Safety System Design Study—Phase I Report, Babcock & Wilcox, BAW-1344, Lynchburg, Virginia, December 1969.

[3] Stevenson, M. G., and Bingham, B. E., "TART—An LMFBR Transient Analysis Project," Conference on the Effective Use of Computers in the Nuclear Industry, University of Tennessee, April 21 - 23, 1969.

[4] Trost, R. J., TAMPA — Computer Program for Analyzing Reactor Fuel and Cladding, Babcock & Wilcox, NPGD - TM-37, Lynchburg, Virginia, April 1969.

APPENDIX

Preliminary Fuel Failure States

Foreword

One of the principal considerations in the analysis of reactor transients is the state of the fuel pin. It is important for the analyst to be able to predict, at least in an approximate fashion, the time and mode of fuel pin failure, should such occur, since the failure of substantial numbers of fuel pins can materially alter the course of the transient.

The consequences of fuel pin failure could compound the problems associated with large reactor transients. In certain transients, the potential exists for a release of molten fuel to the coolant channels; therefore, it is important to be able to predict cladding behavior in transient conditions. Also, there is some question about the possibility of pin failure propagation for certain failure modes.

This appendix presents some preliminary analytical considerations of cladding failure and failure states. The results are intended to be used as an analytical tool to augment the analyses typically performed in a safety evaluation.

One may conclude (tentatively in the case of some failure mechanisms) that the causes of failure are: (1) melting and (2) overstressing and excessive deformation of the cladding due to fuel expansion or gas pressure. Of course overstressing and melting could occur simultaneously.

Little consideration of the failure mechanism of melting should be required in this evaluation. The causes of melting can be traced to two events: (1) sodium boiling and the consequent vapor blanketing or (2) molten fuel and cladding contact. Vapor blanketing of the fuel pin effectively removes the heat "sink" of the pin. Melting of the cladding as a result of contact between molten fuel and cladding would indubitably be accompanied by sodium boiling for normal reactor flows, but we have listed molten fuel and cladding contact as the initiating failure mechanism. The second failure mechanism mentioned above is discussed in the following section.

The mechanism of fuel thermal expansion is examined as a possible cause of cladding rupture during abnormal reactor operating conditions. Although we considered only the effects of (1) very rapid power transients and (2) relatively slow power transients, the range of variables for the latter case is broad enough to allow use of the results for flow

coastdown accidents. Failures resulting from this mechanism may be important relative to the initiation of (1) sodium boiling (solid-fuel and sodium contact), (2) gas release, or (3) flow blockage. Possible failure propagation may then affect the course of the accident.

1. Gas Pressure Failure Mechanism

1.1. Fission Gas

In attempting to determine the states of incipient failure for fuel pins due to gas pressure, the important parameters are: the (1) amount of gas (moles), (2) gas temperature and (3) gas volume. Contributing to the amount of gas are the initial charge gas, vent performance, gas release upon fuel melting, and fuel vaporization. Here we will assume that the effects of the initial charge gas are negligible and that the vent passes a negligible amount of fission gas or fuel vapor during a transient.

During steady-state operation, some fraction of the fission gas formed is retained in the fuel. Thus, upon melting of the fuel during an abnormal operating condition (for these purposes, an increase in power), the fuel may release this stored fission gas. The amount of fission gas released from the molten fuel is a function of the amount stored and the solubility of the gas in the liquid fuel. We will assume negligible solubility of the gas in the liquid fuel, so that any stored gas becomes available upon melting of the fuel.

There is some uncertainty in determining the amount of stored fission gas held in the fuel, but some evidence indicates that the fraction of stored fission gas depends on fuel density, surface area, temperature, stoichiometry, burnup, and fission rate. For simplication, we shall consider the fission gas release fraction (1.0 minus the stored fraction) as a function of temperature only. Two release fraction models are used:

1. 1.00, $T > 3400°F$
   .50, $3400 > T > 2700°F$
   .04, $2700°F > T$

2. 1.00, $T > 2700°F$
   .04, $2700°F > T$

where T is the steady-state, operating fuel temperature in degrees Fahrenheit. Model 1 is very similar to the release fraction values

used by Hanson and Field.[1] The difference, however, lies in the temperature values, which correspond to columnar and equiaxed grain formation temperatures, taken as 3400 and 2700 F, respectively. The values in 2, above, give good agreement with release fractions measured for pellet fuels at greater than 6 atom % 2 burnup .

In Figure A-1, a section of a fuel pin, the dashed lines correspond to molten fuel contours that would reasonably result from a very rapid power increase. The following parameters are pertinent to this pin configuration:

1. Smeared fuel density of 85%.
2. Peak power of 12.9 kw/ft at 100% core power.
3. Uniform cladding temperature of 1050 F.
4. Inner cladding radius of 0.130 inch.
5. Gap conductance of 1500 Btu/ft^2-h-°F. (For determination of initial temperature distributions).

In calculating the molten fuel boundaries, the following assumptions were made:

1. No heat transfer to the cladding.
2. Constant radial temperature gradients at a given axial location.
3. Constant fuel specific heat.
4. Fuel latent heat of vaporization equivalent to a temperature rise of 1240 F.
5. Fuel melt temperature of 5000 F.
6. Constant axial power peaking factor.

The molten fuel boundaries were used in calculating the fuel mass melted as a function of the fraction of the fuel pin's inner radius melted at the core's midplane. The fuel density distribution was taken into account where the columnar grain density was taken as 0.99 of the theoretical. The equiaxed grain density between operating isotherms of 2700 and 3400 F was taken as 0.98 of theoretical. The axial distribution of stored fission gases was assumed to be identical to the axial power shape.

Figure A-2 shows the amount of fission gas released upon the melting of fuel in a transient. The burnup designations pertain to the

peak fuel burnup in the hot pin. The moles of gas were determined by the relationship

$$n = \frac{(Bu)\,(2.678 \times 10^{21}\ \text{fissions/MWd}) \times Y_{fg} \times M(1-RF)}{A_v} \qquad (A-1)$$

where

n = number of g-moles,

Bu = burnup (MWd/g),

Y_{fg} = fission gas yield (atoms/fission),

M = mass of molten fuel (g),

RF = release fraction for steady state,

A_v = Avagadro's number (atoms/g-mole).

Given the mass of fission gas, the volume and temperature distribution can be calculated if the fission gas pressure is known. We have assumed that the released fission gas is at the fuel melting temperature of 5000 F. The determination of gas volume is dependent upon void size, porosity of the fuel melted, and volumetric expansion of fuel, as well as the extent of cladding deformation.

Figure A-3 shows the gas volume as a function of the fraction of fuel radius melted at the core's midplane. This curve was obtained under the assumption that the volumetric fuel expansion upon melting is 0.096. No account of unmelted fuel porosity or fuel thermal expansion was taken. These two effects oppose each other, and the porosity effect is likely to be dominant. The effects of fuel swelling on the available volume were not accounted for.

To simplify the determination of cladding stresses resulting from fission gas pressure, the gas volume with no cladding deformation was taken as 0.05 inch.[2] From Figure A-2 it can be seen that no appreciable gas release occurs below a fractional melt radius of 0.60. From Figure A-3, then, we see that 0.05 inch is a reasonable choice of gas volume for melt radii ranging from 0.60 to 1.00 of the inner cladding radius.

Figure A-4 gives the gas pressure and the cladding hoop stress as functions of gas mass and gas volume. The gas pressure is taken as

$$p = C \cdot \frac{n\bar{R}T}{V} \qquad \text{(A-2)}$$

where
- p = pressure (psi),
- C = 0.497 (psi × in^3/°R)/(atm × cm^3/°K),
- n = number of g-moles,
- $\bar{R}$ = universal gas constant = 82.06 (atm × cm^3/g-moles °K),
- T = temperature = 5460 °R,
- V = gas volume (in^3).

The hoop stress is calculated by the thin-cylinder relationship

$$\sigma = P(r/t)$$

where
- σ = cladding stress (psi),
- P = gas pressure (psi),
- r = inner cladding radius = 0.130 in.,
- t = cladding thickness = 0.010 in.

The scale shown in Figure A-4, which shows the cladding circumferential deformation corresponding to certain values of gas volume, is for the case of uniform deformation over the active fuel length. For the case examined, this length is 34.7 inches.

A calculation of the cladding deformation required to prevent rupture is possible if information on the ultimate cladding strength is available. Tensile test data for unirradiated 304 SS has been used as shown in Figure A-5[3] The lack of materials property data forces us to neglect any effects of fluence and the rate of loading on the ultimate strength.

The ultimate strength values in Figure A-6 were used to calculate the required values of cladding strain (radial or circumferential)

as a function of cladding temperature and fission gas mass. The gas volume may be expressed as

$$V = 0.05 + 0.07369\ \Delta D/D \qquad \text{(A-3)}$$

where V = volume (in.^{3}) and $\Delta D/D$ = cladding strain (%). Solving for the cladding strain and expressing the gas volume in terms of the mass of gas and cladding stress (accounting for the correspondence between stress and gas pressure) gives

$$\frac{\Delta D}{D} = \frac{1}{0.07369} \left[\frac{223.11\ n \times 10^3}{(\sigma_u/13.0)} - 0.05 \right] \qquad \text{(A-4)}$$

where $\Delta D/D$ and n are as defined previously and σ_u is the ultimate cladding strength.

Figure A-6 shows two possible cladding ductility limits. The upper shaded area represents the ductility limits for a fluence of 1.7×10^{22} nvt at the various cladding temperatures.[4] The lower ductility limit (indicated by the lower shaded area) is arbitrarily placed to some extent. We have utilized this limit in the succeeding analyses as the high burnup cladding ductility limit. The semiquantitative justification for this limit is as follows:

1. Transient tests of fuel pins of ≈70,000 MWd/tonne burnup have indicated 1% cladding deformation as the point of incipient failure.[1]
2. The maximum average cladding temperatures (calculated) for these tests were slightly in excess of 1200 F.
3. We therefore selected 1% deformation at 1200 F as a reasonable limit for high-burnup pins and reduced the ductility for the other temperatures shown by proportional amounts (1/5) from the upper ductility limit.

This lower limit of ductility was considered representative of burnups ranging from 50,000 to 150,000 MWd/tonne one. This limit,

therefore, effectively limits the amount of fission gas that may be released before failure. Noting the allowable fission gas mass and the relationship between gas release and the fraction of fuel radius melted (see Figure A-2), the curves of Figure A-7 result. This figure shows the calculated molten fuel radius at the midplane for which cladding failure should occur. The dashed lines represent steady-state fission gas release rates that might reasonably be expected at low burnups, as discussed previously. The solid lines are more representative of high burnup gas release. We therefore have shown a "faired-in" broken line which may be a truer relationship of molten radius at failure versus burnup.

The failure states in Figure A-7 have been calculated for a particular set of thermal conditions; i.e., rapid power rise, no heat transfer to cladding, etc. To translate these results into usable results under other conditions, Figure A-8 is presented. From this figure, which shows the fraction of pin fuel melted as a function of the fraction of radius melted, one may obtain an equivalent melt radius for use in Figure A-7. Of course, the slower the transient, the more error obtained in this equivalent radius value, since the molten fuel boundaries change for a given fraction of the radius (at the core midplane) melted (see Figure A-1).

1.2. Gaseous Fuel

Considerable uncertainty exists in determining the vapor pressure of the molten fuel. Figure A-9 shows possible values of vapor pressure as given by Osborn and Sherer.[5] The difference in the vapor pressure determinations has been attributed to the formation of the more volatile U_2O_4 vapor. These are equilibrium values, of course, and the gaseous fuel pressure is expected to be somewhat lower depending on the rate of fuel temperature rise and the gas volume available.

If we assume no significant fuel movement away from the core midplane upon fuel melting, we can calculate the maximum central fuel temperatures in a fuel pin in a manner identical to that used in the preceding section. We will again assume a rapid power rise in which heat transfer from the fuel is negligible. Assuming a constant shape of the radial temperature profile (except in the fuel area in which the heat of

fusion is being supplied), we can calculate the maximum temperature in the hot pin as a function of molten fuel radius. Figure A-10 illustrates the result. (All the figures are based on the hot pin of 0.130-inch inner cladding radius.) Figures A-9 and A-10 may be combined to show the gaseous fuel pressure as a function of melt radius as is shown in Figure A-11. Using the ultimate stress information from Figure A-5, we obtain Figure A-12, which shows the melt fractional radius (at the core's mid-plane) at which failure should occur as a function of cladding temperature. The limitations of Figure A-5 apply here; that is, irradiation and loading rate effects have been neglected.

2. Conclusions

Cladding failure may occur by melting in the event of a loss of flow (and subsequent sodium boiling) or by contact with molten fuel. The conditions under which cladding is expected to fail due to fission gas pressure are presented in Figure A-7. A number of assumptions for materials behavior are inherent in this figure. These are primarily values of ductility and ultimate strength. Assuming sufficient cladding ductility, this failure mechanism is not operative at low burnup values (before molten fuel and cladding contact occurs). Calculations show that this value of low burnup is about 6000 MWd/tonne.

Figure A-12 shows the incipient failure states for the gaseous fuel mechanism. Assumptions about the cladding's ultimate strength were made in obtaining this figure.

3. Fuel Thermal Expansion Mechanism

During a reactor power increase from some given quasi-steady condition, the fuel and cladding temperatures will increase. The two bodies (fuel and cladding) will generally experience different rates of temperature increase depending on the magnitude of the power ramp and the core coolant flow rate and inlet temperature. The stainless steel cladding has a slightly higher coefficient of thermal expansion than does the fuel, but the fuel is likely to undergo much larger temperature increases in a transient (assuming that the cladding remains in contact with the sodium coolant). One would therefore expect that certain combinations of initial pellet–cladding gap (or initial cladding strain), fuel

temperature rise, and cladding temperature rise would result in mechanical interaction of the fuel and cladding and plastic deformation of the cladding and/or fuel. The failure state for the fuel pin has been determined by calculating the maximum allowable rate of fuel temperature rise as a function of cladding temperature and the maximum fuel melt temperature's isotherm radius. Failure is assumed not to occur if cladding exerts enough pressure on the fuel to balance the thermal expansion by plastic fuel deformation (creep). The analytical approach follows. Assumptions made for the mechanics analysis are:

1. The fuel structure that is assumed to be of importance consists only of the fuel that is below the melt temperature. In other words, fuel that has absorbed any fraction of its heat of fusion cannot contribute to loading the cladding. This, of course, assumes negligible internal void hydrostatic pressure.

2. The portion of the fuel below the fuel melt temperature is treated as a thick plastic cylinder.

3. The cladding is considered to be a thin cylinder; i.e., the hoop stress does not vary with the radial location.

4. Strain rates are considered in terms of engineering strain and not true strain rates.

5. The strain history of the fuel is neglected.

6. The effects of fuel grain size on the fuel creep rate is neglected.

7. The relationship between the intensity of the strain rate and the intensity of the stress for plastic deformation is assumed to be identical to the strain rate and stress relationship for uniaxial creep tests.

8. Axial fuel temperature gradients are neglected. Actually, for the uncracked fuel column, cooler portions of fuel will tend to restrain axially adjacent hotter portions of fuel (shear stresses are set up).

Assumptions for the fuel temperature calculations are as follows:

A. Fast Transients

1. Heat transfer to the cladding is negligible. This is a good assumption for the initial thermal effects of a step change in linear power to q' equal to 10.0 q'_o (where q'_o is the initial 100% power level).

2. Negligible time (or alternatively, negligible fuel thermal conductivity) for any appreciable radial heat transfer in the fuel.

3. Constant fuel specific heat up to the fuel melting temperature.

4. The fuel melting process does not significantly affect the slope of the radial temperature profile.

B. Slow Transients

1. Constant fuel effective thermal conductivity up to the melt temperature.

2. The fuel specific heat produces a negligible fuel temperature lag in a power transient.

3. Constant fluid heat transfer coefficient, constant cladding thermal conductivity, constant fuel—cladding gap conductance, and negligible cladding specific heat.

4. No axial fuel movement.

In the analysis, only the hot pin was considered. The 100% power operating condition was taken to be:

Linear power, - kW/ft	12.9
Max central fuel temp F,	4000
Central void radius, in.	0.34
Fuel surface temp F,	1470

The 100% power temperature profile for the hot pin, as determined by the computer code TAMPA, was fit by a second-degree polynomial

$$T(r) = 3680 + 1.8667 \times 10^6 (r) - 27.452 \times 10^4 (r)^2. \qquad \text{(A-5)}$$

The temperatures for fast and slow transients become

$$T(r) = 3680 + 1.8667 \times 10^6 (r) - 27.452 \times 10^4 (r^2) + \Delta T_{rise}, \qquad \text{(A-6)}$$

and

$$T(r) = \left\{\left[3680 + 1.8667 \times 10^4 (r) - 27.452 \times 10^4 (r^2)\right] - 800\right\} q'/q'_o + T_{inlet} \qquad \text{(A-7)}$$

where ΔT_{rise} is the temperature rise for a fast transient,

q'/q'_o is the normalized power (normalized with respect to initial power),

T_{inlet} is the core inlet temperature (F).

The fuel expansion may be calculated by assuming that it is determined by either the average fuel temperature rise or the fuel surface temperature rise of the fuels surface. An assumption is required for the pertinent temperature determining this expansion in the absence of a detailed calculation of the thermal strain and stress distributions in the fuel. The coefficient of fuel thermal expansion (α) is taken as[4]

$$\alpha = 6.797 \times 10^{-6} + 1.448 \times 10^{-9} (T) (\text{in./in.}^{\circ}\text{C}) \qquad \text{(A-8)}$$

where T is the fuel temperature in degrees centigrade. Using this coefficient of expansion, we can determine the fractional fuel expansions for fast or slow transients. Figure A-13 shows fuel expansion as a function of the average temperature rise of unmelted fuel. We consider only the unmelted fuel, since it has been assumed that the fuel beyond the melt temperature isotherm is the only structurally significant portion. There is a unique relationship between the average temperature rise and the maximum radius of the melt temperature isotherm for a given initial temperature profile; the values of these radii are shown in Figure A-13. Also, the effects of two fuel melt temperatures are shown. These temperatures correspond to 0 and 140,000 MWd/tonne fuel burnup.

Figure A-14 shows the calculated fractional fuel expansion for a slow transient. The figure is based on the assumption that the average temperature rise is the pertinent temperature. Core inlet temperatures of 800 and 1200 F are shown for comparison.

The creep strain rate of the fuel is a function of the fuel temperature (this is discussed in detail later). In order to calculate fuel stress distributions, we have determined the radial temperature distributions for fast and slow transients as shown in Figures A-15 and A-16. These temperatures have been normalized relative to the melt temperature. For the case of the lowered fuel melting temperature resulting from the effects of irradiation, it is assumed that the significant thermal effect is the ratio of the temperature to the melt temperature and not solely the effect of the absolute temperature of the fuel.

Wolf and Kaufman present data for the creep rate of UO_2 at various levels of temperature and stress.[6] Their data indicates that the steady-state creep rate (ϵ_{ss}) can be represented by a function of the form

$$\epsilon_{ss} = A_1 \sigma \exp\ (-Q_1/RT) + A_2\ \sigma^n\ \exp\ (-Q_2/RT) \qquad \text{(A-9)}$$

where A_1, A_2, Q_1, Q_2, and n are constants, σ is the stress, R is the universal gas constant, and T is the absolute temperature. If we neglect the first term in A-9 and use Wolf and Kaufman's creep data at 1430 and 1800 C, we can determine A_2 and Q_2 assuming n = 4.8. We then obtain the relationship

$$\epsilon_{ss} = 1.588 \times 10^{-8}\ (1/\text{h-psi}^{4.8})(\sigma)^{4.8}\ \exp(-9100/RT). \qquad \text{(A-10)}$$

A plastic analysis of the fuel allows us to determine the cladding pressure that must be exerted on the fuel to cause it to strain plastically at a given rate. If this strain rate is sufficient to counteract the rate of fuel thermal expansion, then the cladding strain rate may be taken as zero (neglecting cladding creep). Taking the fuel as a cylindrical annulus, the creep rates due to fuel stresses are as follows:

$$\dot{\epsilon}_\theta = 1/2\ (1-3b^2/r^2)\ \alpha\Delta\dot{T}. \qquad \text{(A-11)}$$

$$\dot{\epsilon}_r = 1/2\,(1 + 3b^2/r^2)\,\alpha\Delta\dot{T}. \tag{A-12}$$

$$\dot{\epsilon}_z = -\alpha\Delta\dot{T}. \tag{A-13}$$

The subscripts θ, r, and z refer to the cylindrical coordinate directions, b is the outside fuel radius, r is the radius, and $\alpha\,\Delta\dot{T}$ is the rate of fuel thermal expansion.

Following Zudans[7] plastic analysis of thick-walled cylinders, we obtain the intensity of the strain rate ($\dot{\epsilon}^*$):

$$\dot{\epsilon}^* = \alpha\Delta\dot{T}\left[3(b^4/r^4) + 1\right]^{1/2}. \tag{A-14}$$

We can obtain a relationship between the radial and tangential fuel stresses by employing the definition of the stress intensity and the equation for the axial strain rate in terms of the fuel stresses ($\sigma_z \neq o$; the fuel is axially restrained). We obtain

$$\sigma_\theta - \sigma_r = -\frac{2}{3}\,(\sigma^*)^2 - \dot{\epsilon}_z/\dot{\epsilon}^*_z\,, \tag{A-15}$$

which when substituted into the equation of equilibrium,

$$\sigma_\theta - \sigma_r - r(d\sigma_r/dr) = 0, \tag{A-16}$$

gives

$$d\sigma_r/dr = -\,1/r \times \frac{2}{3}\,(\sigma^*)^2 - \frac{\dot{\epsilon}_z}{\dot{\epsilon}^*}(\sigma^*)\,. \tag{A-17}$$

Zudans assumes that the relationship between the intensity of stress and the intensity of strain rate is identical to that for the stress and strain rate for uniaxial loading. If we make the same assumption, i.e., if

$$\dot{\epsilon}^* = 1.588 \times 10^{-8}\,(\sigma^*)^{4.8}\,\exp\,(-91000/RT), \tag{A-18}$$

then we can determine the distribution of the radial stress in the fuel. Rewriting the equation for the radial stress gradient, we obtain

$$\frac{d\sigma_r}{dr} = \frac{1}{r} \times \frac{2}{\sqrt{3}} \left[\frac{(\dot{\epsilon}^*)^{2/n}}{(Ae - Q/RT)^{2/n}} - \frac{a\Delta T(\dot{\epsilon}^*)^{\frac{1-n}{n}}}{(Ae - Q/RT)^{1/n}} \right]^{1/2}, \qquad \text{(A-19)}$$

where again the intensity of strain rate is a function of geometry, or

$$\dot{\epsilon}^* = a\Delta\dot{T} \left[3b^4/r^4 + 1 \right]^{1/2} \qquad \text{(A-20)}$$

as given previously.

Now the temperature is a function of the fuel radius as shown in Figures A-15 and A-16. Using the temperature values in these figures, the radial stress distributions in the fuel are calculated by numerical integration of A-19. The radial fuel stress at the inside surface of the fuel cylinder was assumed to be negligible. Figures A-17 and A-18 show the resultant tangential stress of the cladding as determined by equating the pressures on the fuel and the cladding at the interface and using the thin-walled cylinder relationship,

$$\sigma_\theta \Big|_{\text{cladding}} = \frac{(P)(r)}{t} . \qquad \text{(A-21)}$$

Knowledge of this cladding stress allows us to calculate the maximum permissible cladding temperature for given values of the cladding's ultimate strength. This calculation of maximum cladding temperature would apply only when the cladding strain was at the maximum permissible value (the maximum ductility). Likewise, we may calculate the allowable rate of fuel temperature rise for a given cladding temperature. Figure A-19 gives the values of the cladding's ultimate strength as a function of cladding temperature.[3]

To determine the conditions at which the cladding's ductility limit is reached, we must know:

1. Thermal expansion (or initial and final temperature) of the cladding.
2. Thermal expansion of the fuel.
3. Initial fuel-cladding gap or cladding strain.

The cladding strain (ϵ) resulting from a power transient can be expressed by

$$\epsilon = (\alpha\Delta T)_{fuel} - (\alpha\Delta T)_{cladding} - (d/D), \qquad \text{(A-22)}$$

or

$$\epsilon = (\alpha\Delta T)_{fuel} - (\alpha\Delta T)_{cladding} + \epsilon_o, \qquad \text{(A-23)}$$

where A-22 is for the case of an initial unit diametral gap (d/D), and A-23 is for an initial cladding strain (ϵ_o). In either case, the $(\alpha\Delta T)_{fuel}$ is the diametral fuel unit expansion, and $(\alpha\Delta T)_{cladding}$ is the diametral cladding unit expansion. The difference between the fuel OD and the mean cladding radius is neglected. Let us examine the case where no fuel-cladding gap exists and no initial cladding strain exists (we then exclude any effects of creep strain that might occur during normal operation); in other words, the fuel and the cladding are just touching. Figure A-20 shows the fuel unit expansion that will produce a given cladding strain depending on the temperature of the cladding. (The initial cladding temperature is taken at 1050 F). The shaded area represents the assumed ductility limit of the cladding, which varies with temperature.

Since the cladding stress required to cause a sufficient plastic fuel strain rate is given in terms of the maximum melt temperature isotherm in Figures A-17 or A-18, we should translate the fuel unit expansions in Figure A-8 to values of the melt temperature isotherm radius. This is done in Figure A-21, which expresses the information in Figures A-13 and A-14 in a more useful manner.

Figures A-22 and A-23 show the allowable rate of fuel temperature rise as functions of cladding temperature and the maximum radius of the

melt temperature isotherm for fast- and slow-power transients, respectively. The solid lines were plotted utilizing the information shown in Figures A-17, A-18, and A-19. The shaded areas are the actual limiting conditions, since these account for the fuel thermal expansion, cladding thermal expansion, and cladding ductility as obtained from the information in Figures A-20 and A-21. Two shaded areas are shown in the left portion of Figure A-20. The lower shaded area pertains to the case in which fuel thermal expansion is determined by the average fuel temperature rise, and the upper area to that in which expansion is determined by the temperature rise of the fuel's surface. All other shaded areas of Figures A-22 and A-23 pertain to the case in which fuel expansion is determined by the average fuel temperature rise.

The broken lines shown in the two parts of Figure A-11 represent the paths of slow transients in terms of cladding temperature and the maximum radius of the melt temperature isotherm. The abscissas of the rate of fuel temperature rise have no meaning in connnection with these lines (paths) except where they intercept the shaded areas. At the point(s) of interception, the abscissa indicates the maximum allowable rate of fuel temperature rise. The lines or paths of the slow power transients were established by considering the relationship between the linear power of the pin and the maximum radius of the melt temperature isotherm. This relationship is determined by the equation for the temperature profile for a slow transient, which was given earlier. Figure A-24 is a plot of the relationship between the pin's normalized linear power (normalized relative to the pretransient power) and the maximum radius of the melt temperature isotherm.

A number of limitations are inherent in the data of Figures A-10 and A-11. The primary ones are as follows:

1. The temperature profiles for a given maximum radius of the melt temperature isotherm are those given in Figures A-15 and A-16. These temperature profiles will represent the actual cases for:

   a. Very large step changes in power or very short times for fast transients.

   b. Very small rates of power increase or very short times for slow transients.

2. The grain size of the fuel must be less than 50 microns or thereabout. In a fuel pin, the columnar grains may be about 50×10^3 microns.

3. The creep data used were for unirradiated UO_2.

4. Cladding creep deformations are not accounted for.

3. Discussion and Conclusions

Figures A-22 and A-23 represent the results of the investigation of the effects of the failure mechanism for fuel thermal expansion. Although several rather limiting assumptions have been made in developing these results, we can still make some valid conclusions about the mechanism.

As mentioned previously, the two shaded areas on the left of Figure A-22 indicate the limiting rate of fuel temperature rise for (1) fuel expansion being a function of the average fuel temperature rise (lower shaded portion), and (2) fuel expansion being a function of the rise in the fuel's surface temperature (upper shaded portion). These two possibilities are presented since we have not considered the thermal stresses and certain subsequent plastic deformation and/or fracture of the fuel. The greater yield and creep strength of the outer fuel portions, which are of relatively low temperature, would tend to restrain the high-temperature inner fuel. Since the fuel deformation rates increase exponentially with temperature, it seems reasonable to assume that the net fuel growth will be determined in a transient by something less than the average temperature change.

The calculated allowable rate of fuel temperature rise is dependent upon the cladding's ductility. This is because a change in fuel expansion from, say, 1% to 2% is accompanied by movement of the maximum radius of the melt temperature isotherm (and consequently the width of the structurally significant fuel annulus) as well as by increased fuel plasticity resulting from increased fuel temperatures.

This sensitivity to the cladding's ductility is well illustrated by the shape of the shaded areas, indicating the limiting fuel temperature rise rates. The ductility curve displays a minimum (as shown in Figure A-20) at a temperature of approximately 1200 F. Likewise, the shaded portions of Figures A-10 and A-11 display minimums in the allowable rate of fuel temperature rise at cladding temperatures of 1200 F. From a strength

standpoint, one would expect a continuously decreasing allowable rate of fuel temperature rise with increasing cladding temperatures; however, the increase in ductility of the cladding beyond 1200 F requires higher fuel temperatures to maintain the cladding's deformation limit and results in a smaller, more plastic fuel annulus.

The results shown in Figure A-22 indicate that fuel with a melt temperature of 4450 F does not pose as severe a limitation on the allowable rate of fuel temperature rise as does the 5070 F melt temperature. If we consider the fuel expansion to depend on the average temperature rise (the lower shaded area for the 5070 F melt case and the sole shaded area shown for the 4450 F melt case), then the figure shows that at a cladding temperature of 1200 F, the two failure states are as follows:

	5070 F	4450 F
Melt Temp isotherm radius, in.	0.04	0.085
Allowable rate of fuel—10° temperature rise, 10^0 ° F/s		10^2

The difference is primarily due to this: in the 4450 F case, a smaller fuel temperature increase is required to reach the melting temperature at any given fuel radius. Consequently, the fuel has not expanded nearly as much in this case as in the 5070 F case.

Looking now at Figure A-23, we see that for a slow transient in which the core inlet temperature remains at the initial value of 800 F, the cladding apparently is in danger of rupturing as it approaches 1200 F and a value of the maximum radius of the melt temperature isotherm of 0.08 inch. From Figure A-24, these conditions correspond to an increase in power by a factor of 1.65. No cladding failure is indicated for a slow transient during which the core inlet temperature has increased by 400 F (800 to 1200 F) because the cladding's thermal expansion results in insufficient cladding strain to reach the ductility limit.

For the case of the 800 F inlet temperature, again, cladding rupture occurs for quite low values of the rate of fuel temperature rise when the cladding's ductility limit is reached. In safety analyses we can

generally say that the fuel has such strength that the cladding will rupture at any time in the slow transient when the cladding's ductility limit is reached (provided that the fuel temperature is rising; i.e., that the transient is not "turned around"). This points out the importance of determining thermal expansion of the fuel and values for the ductility of the cladding.

As in other mechanisms of failure, the initial temperature profiles play a significant role. Figure A-22 is applicable only to the case in which the initial temperature profile corresponds to that for the hot pin operating at 100% power. If a fast transient were to be initiated at some initially lower power, then the fuel temperatures would be significantly higher for any given value of the radius of the melt temperature isotherm. This would result in a more plastic fuel condition, which would tend to allow a higher rate of fuel temperature rise before the cladding failed. The thermal expansion of the fuel, however, would be greater than that shown in Figures A-13 and A-14.

Figures A-22 and A-23 are based on certain values of the cladding's ductility. We have considered primarily the effects of irradiation damage in determining these values. The ductility of the cladding is also affected by the extent of creep and fatigue damage in the cladding. Creep damage would probably further decrease the ductility by a very small amount corresponding to whatever safety margin was acceptable at the fuel pin's end-of-life condition. This value could be determined if sufficient materials data were available and if the design of the fuel pin properly accounted for the stress and strain history of the cladding. At this time, however, we do not know what this ductility margin might be. The effects of fatigue are different from those of the creep phenomenon, for fatigue damage is statistical in nature. The fatigue effect causes pins to suffer varying degrees of damage, so that we must treat the problem in terms of determining a certain proportion of pins that are likely to fail under certain conditions.[8] Indeed, in considering the distribution of "fatigue damage," we may say that a certain small proportion of pins is likely to fail even under normal conditions. In a transient, then, a small number of pins will probably fail even before the cladding deforms to the ductility limit as determined by tensile or creep tests. This means that even though the results of Figures A-22

and A-23 might be used for determining gross numbers of fuel pin failures in a power transient, there undoubtedly would be increasing numbers of failures as the transient progressed from the initial conditions.

Figure A-1. Molten Boundaries for Hot Pin Subjected to Rapid Power Increase (Isotherms Shown Correspond to 100% Power Level — Maximum Linear Power of 12.9 kW/ft)

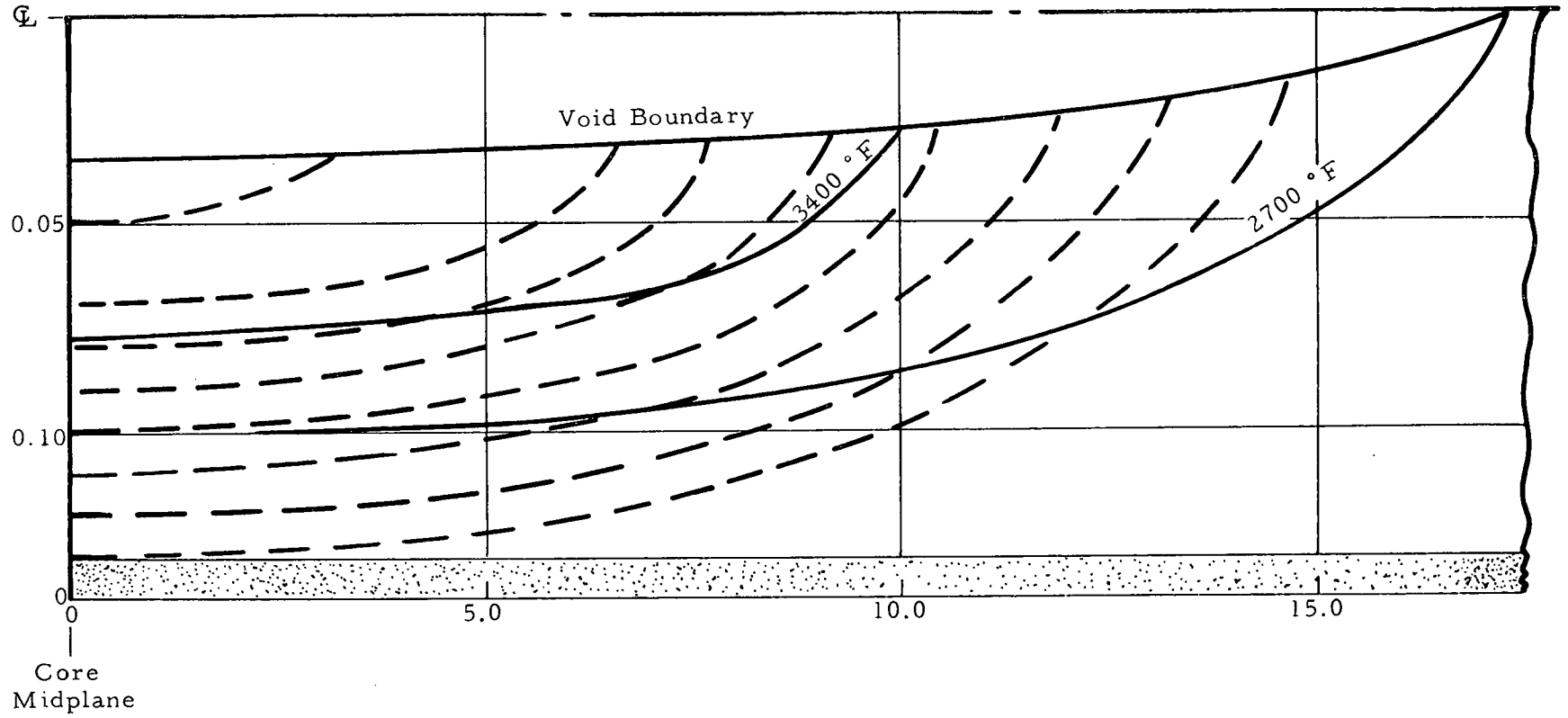

Figure A-2. Gas Released per Fuel Pin Upon Incidence of Fuel Melting

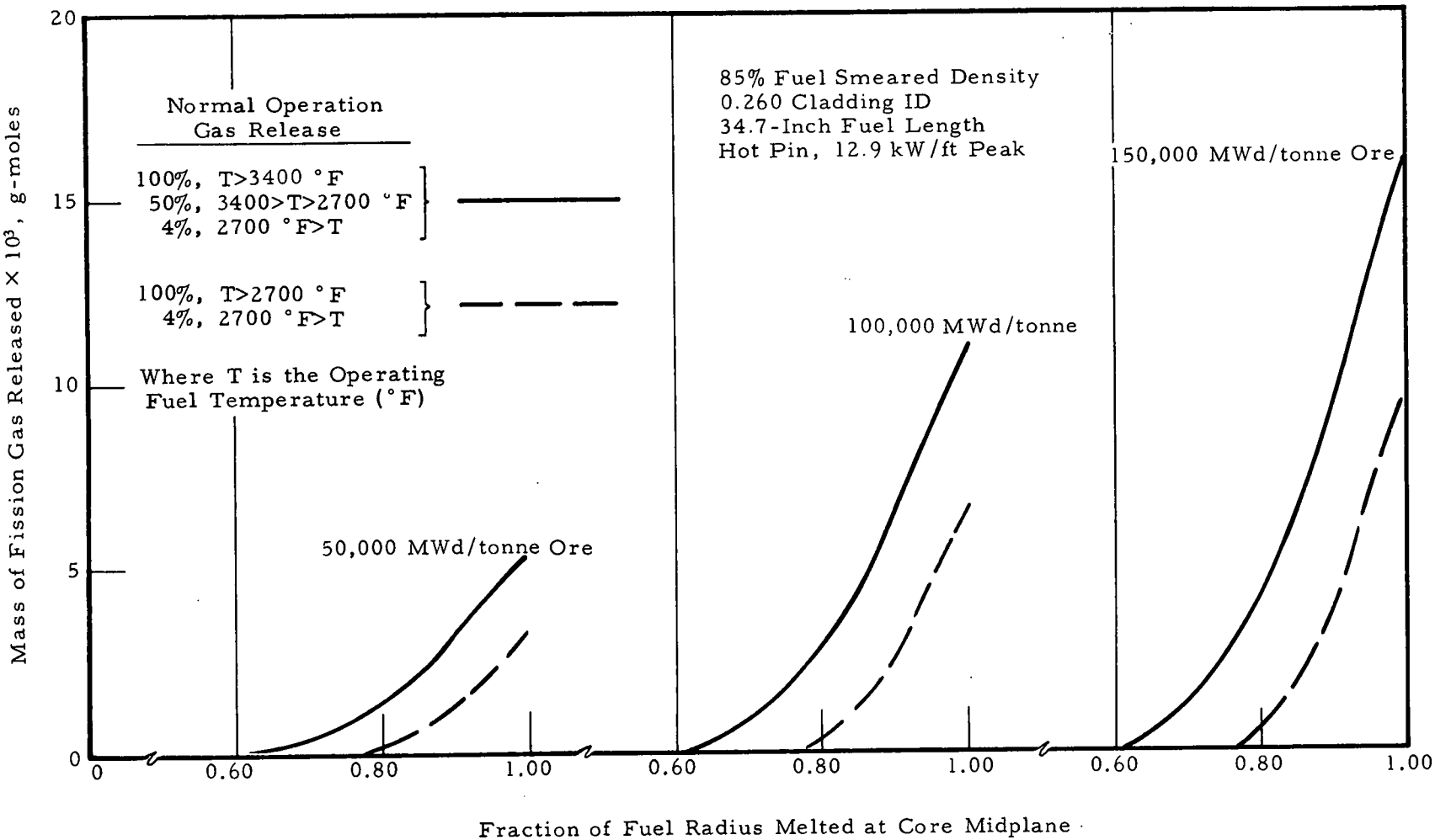

Figure A-3. Available Gas Volume per Pin With No Cladding Deformation (No Account Taken for Unmelted Fuel Porosity and Thermal Expansion — Cladding ID 0.260 Inch, Active Fuel Length 34.7 Inch)

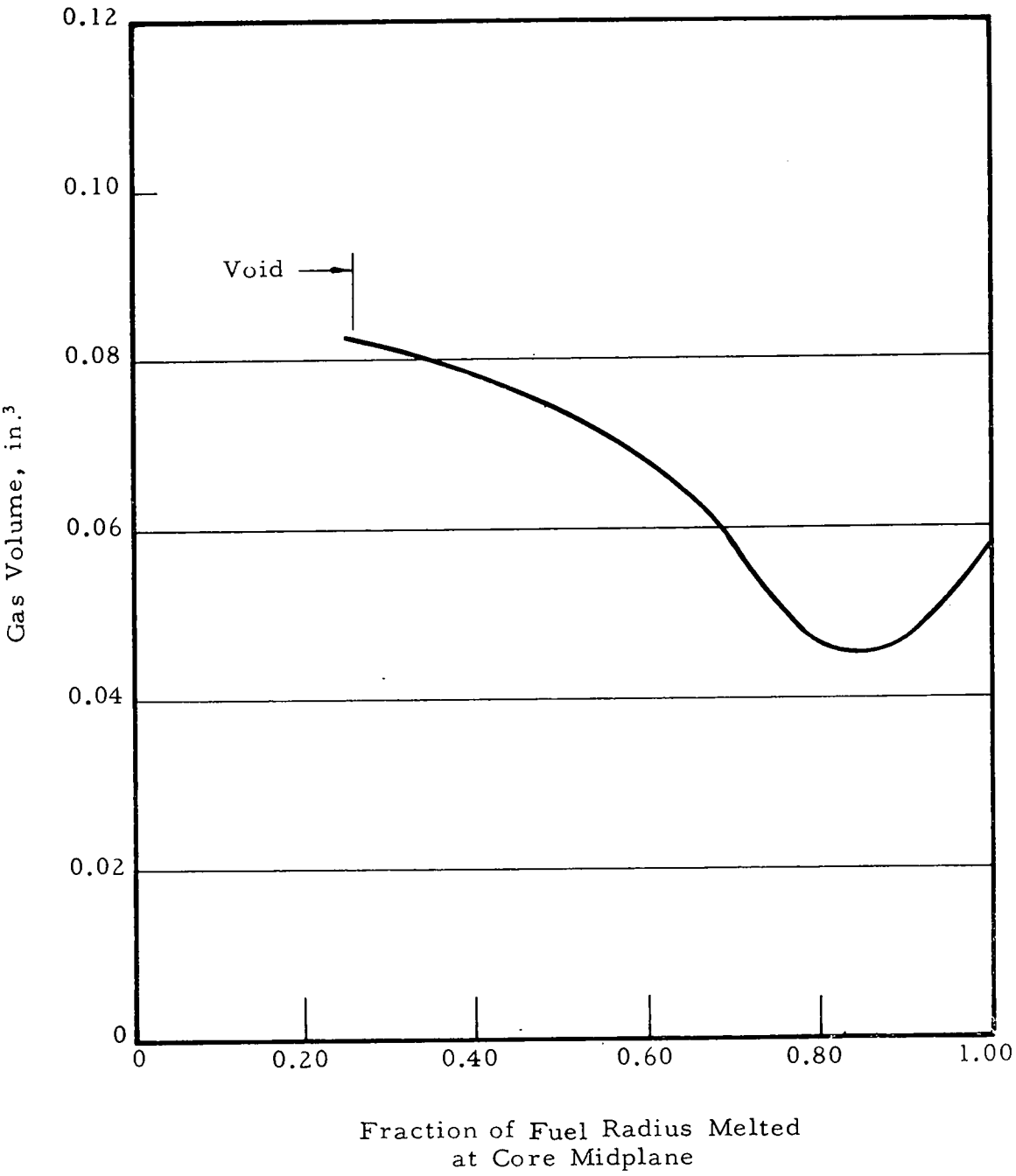

Figure A-4. Gas Pressure and Cladding Hoop Stress for Various Values of Gas Volume and Mass

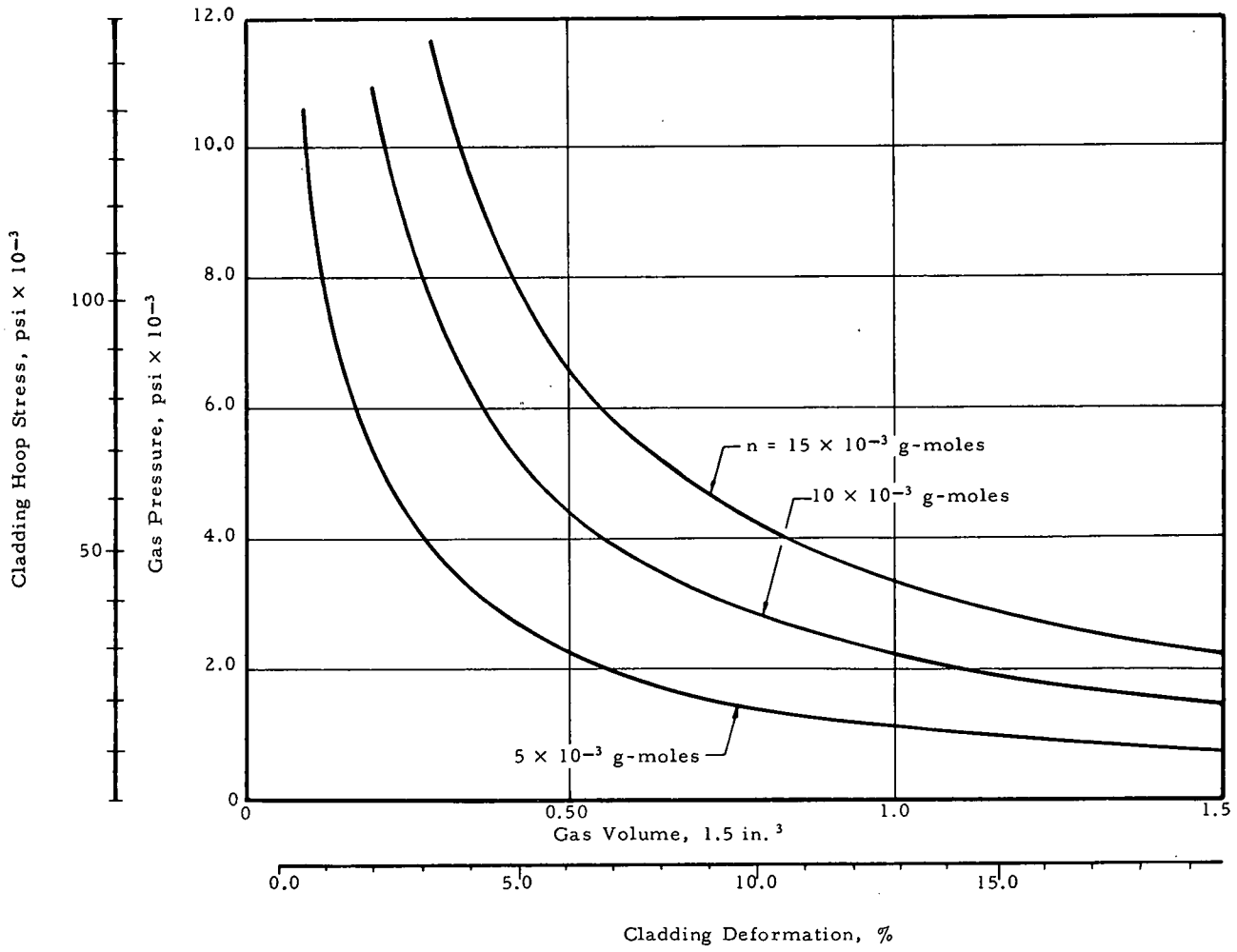

Figure A-5. Cladding Ultimate Strength — Variation With Temperature

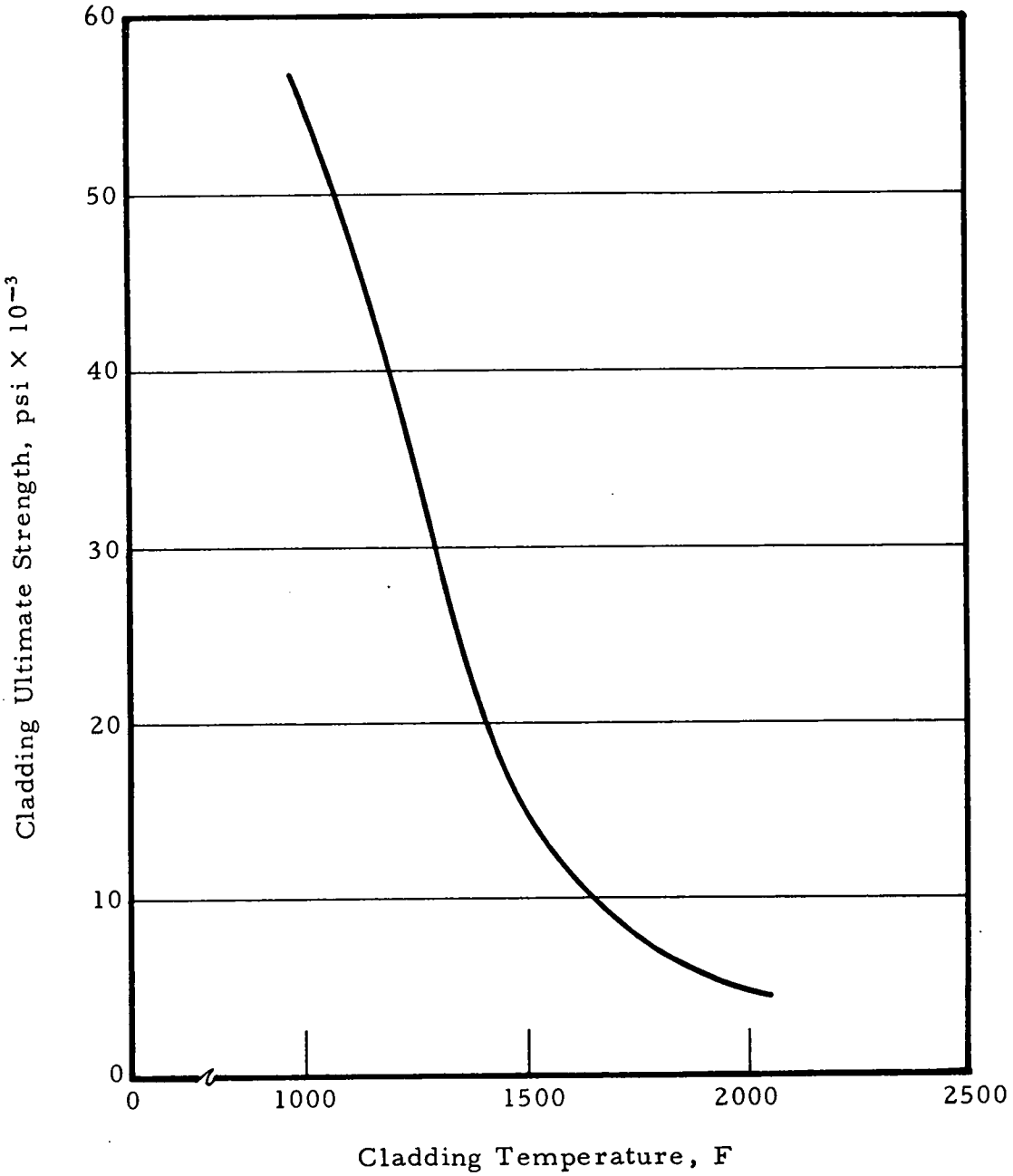

Figure A-6. Cladding Strain for Various Values of Fission Gas Mass and Cladding Temperatures

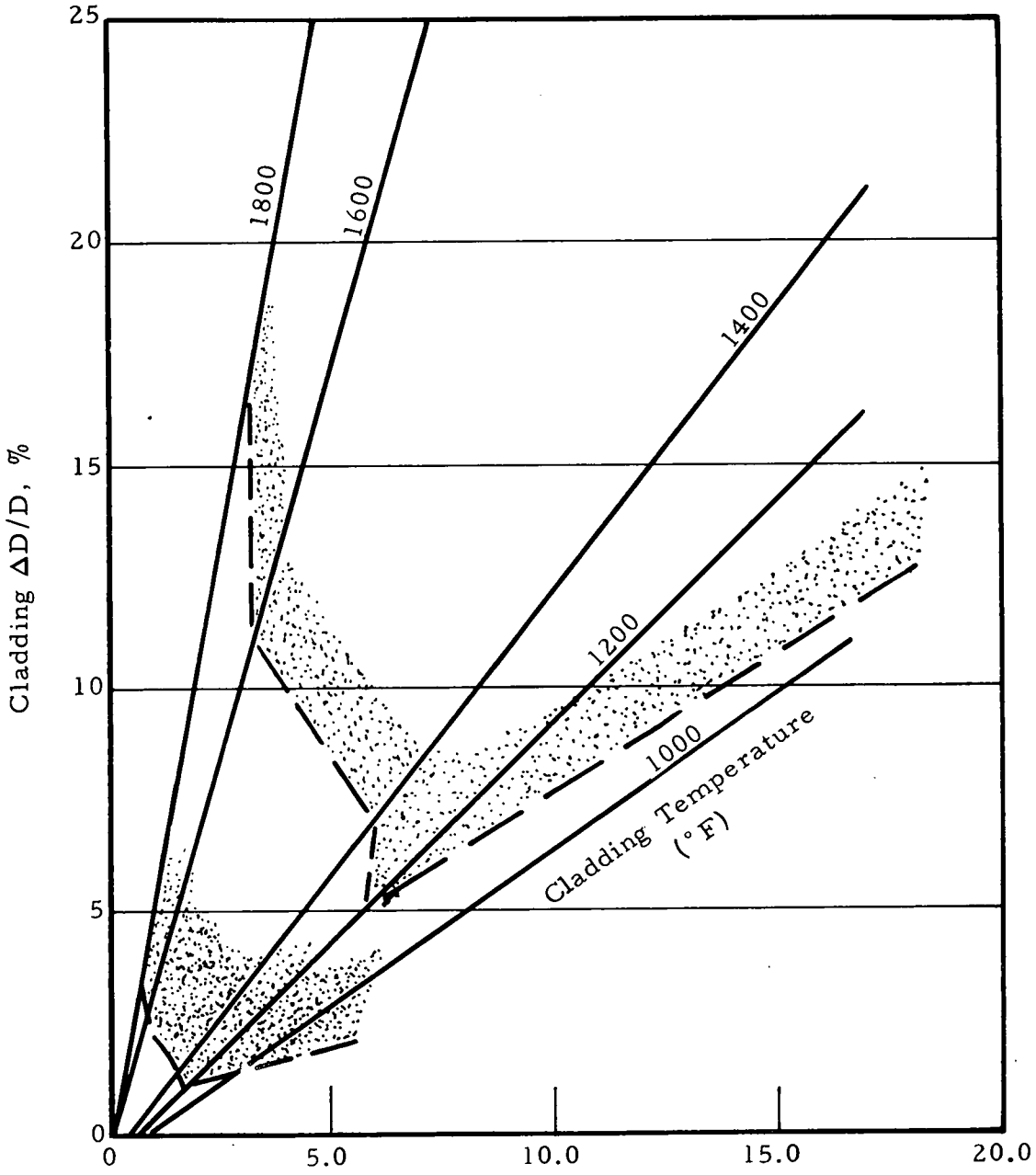

Figure A-7. Molten Radii at Which Failure Will Occur as a Result of Fission Gas Pressure

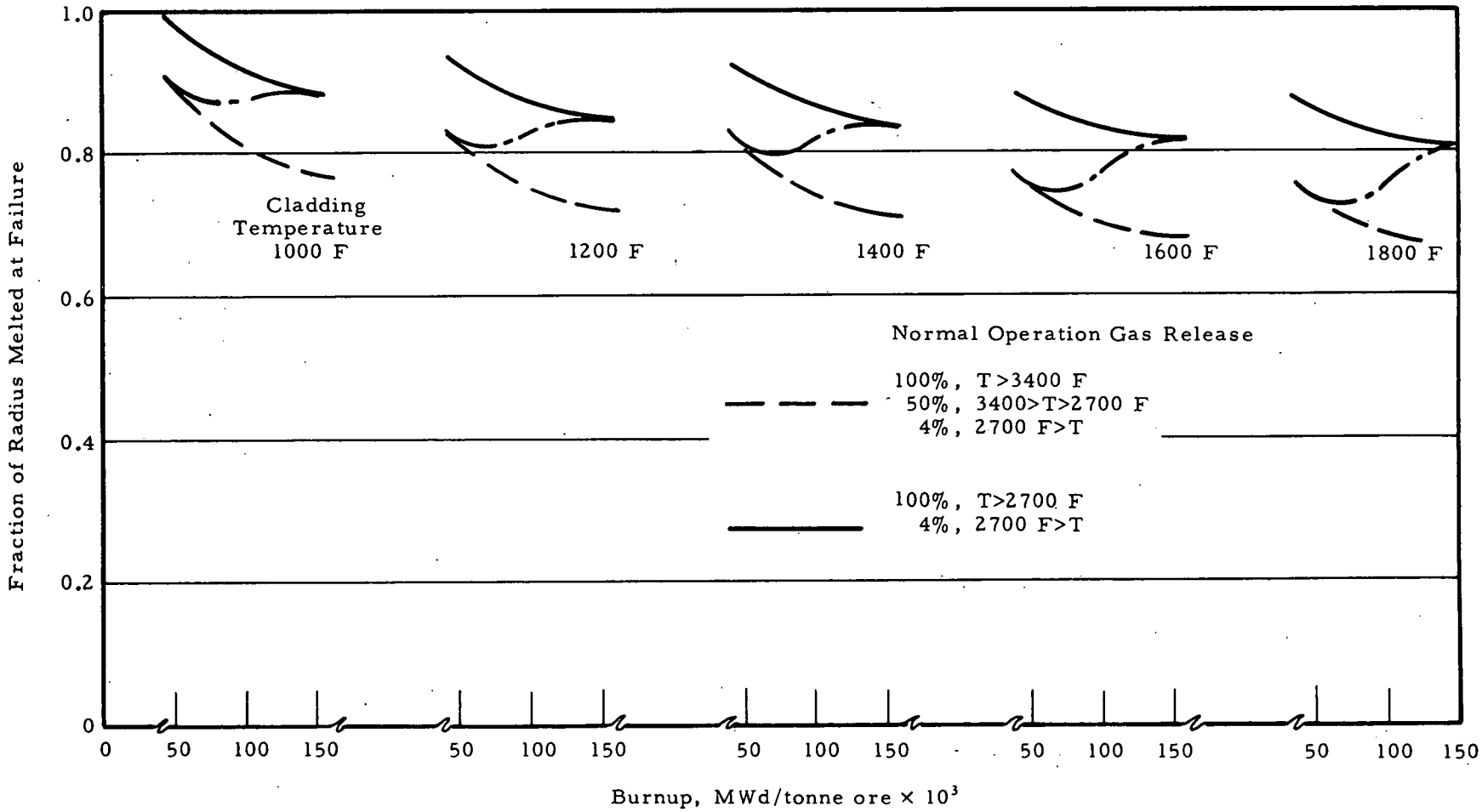

Figure A-8. Relationship Between Fractional Radius Melted and Total Pin Fuel Fraction Melted (Excluding Axial Blankets)

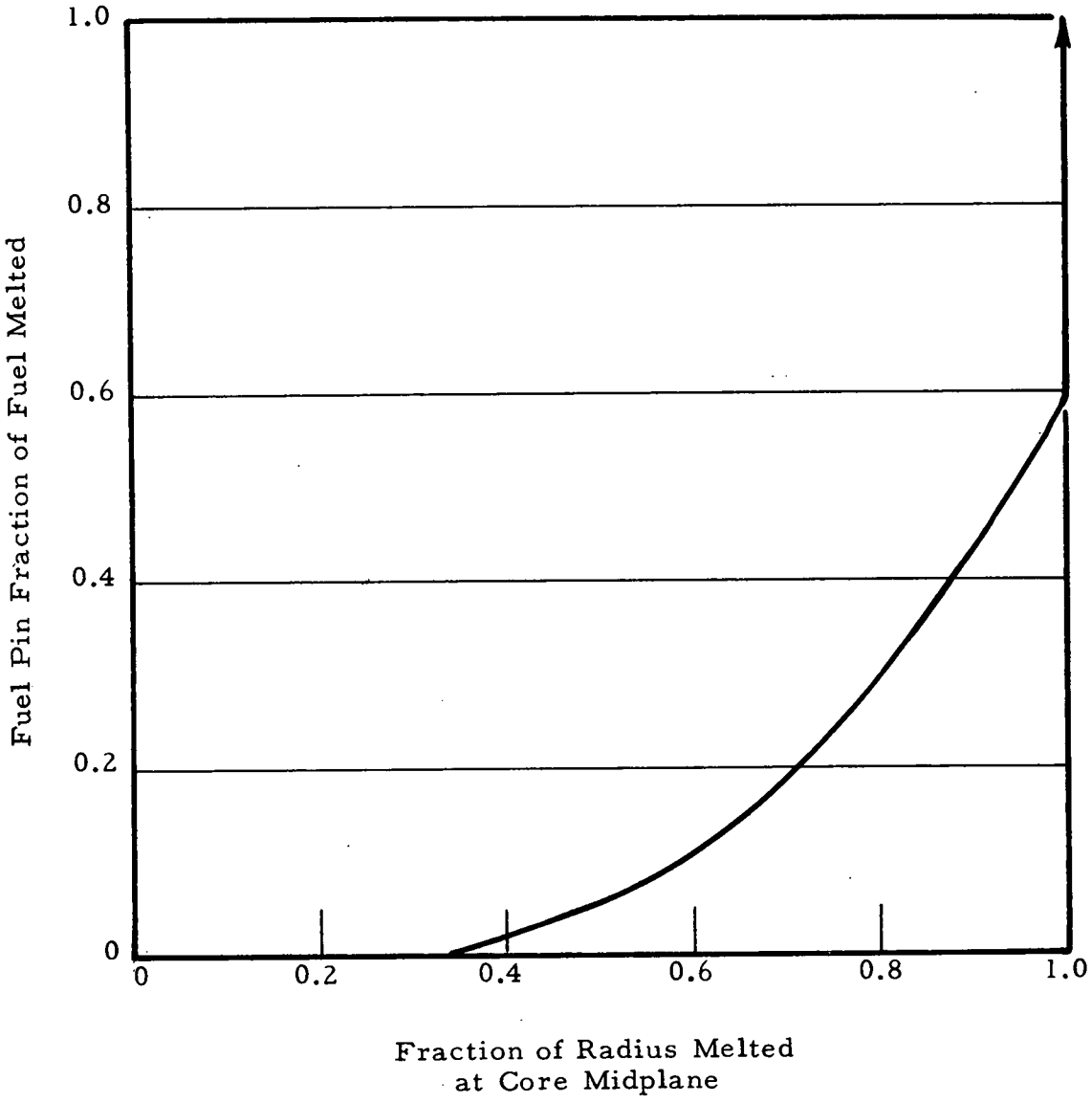

Figure A-9. UO_2 Vapor Pressure

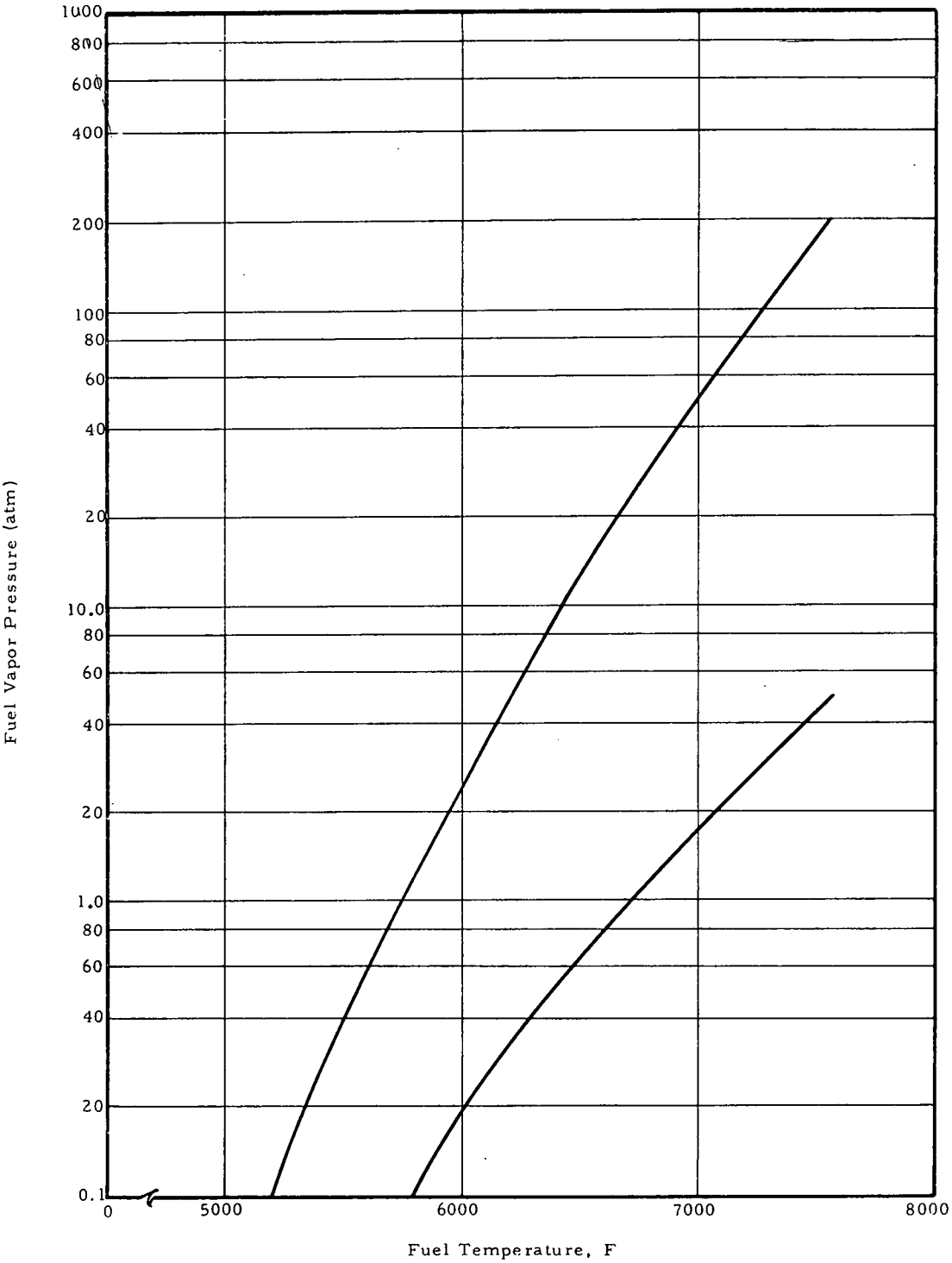

Figure A-10. Maximum Central Fuel Temperature as a Function of Molten Fuel Radius

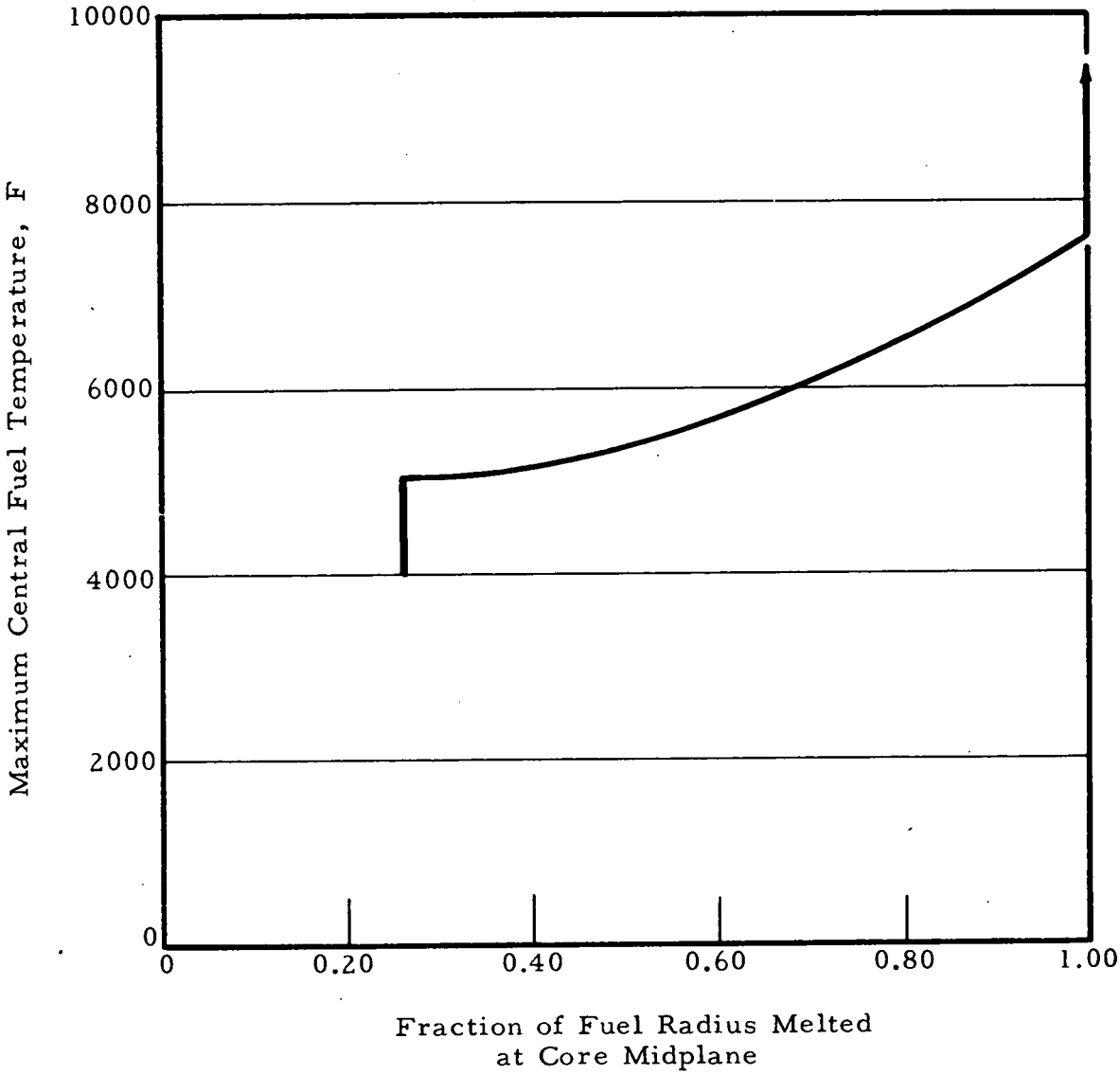

Figure A-11. Gaseous Fuel Pressure as a Function of Molten Fuel Radius

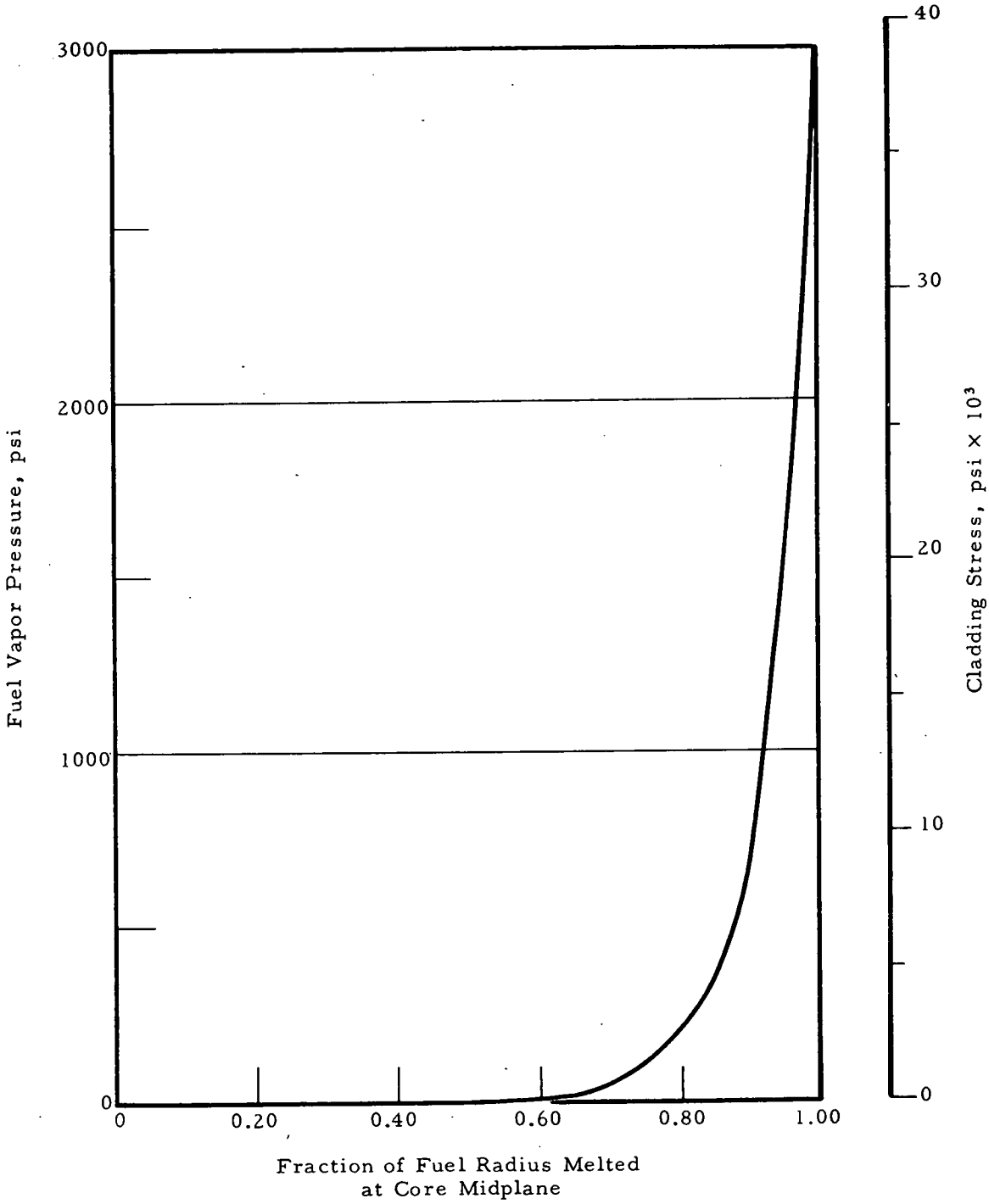

Figure A-12. Cladding Incipient Failure States Accounting for Gaseous Fuel Pressure

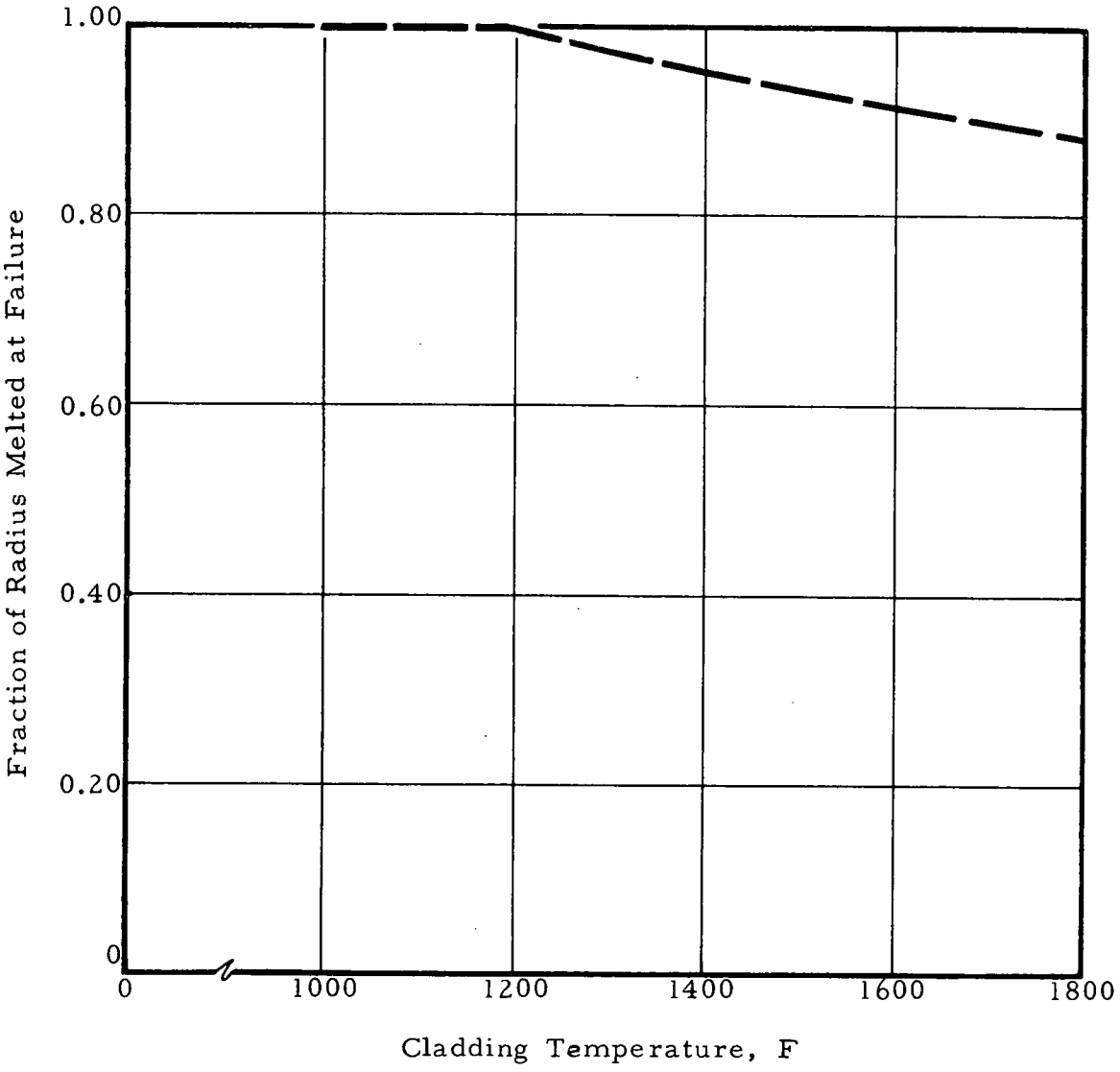

Figure A-13. Unrestrained Fuel Expansion for Fast Power Transient — Hot Pin

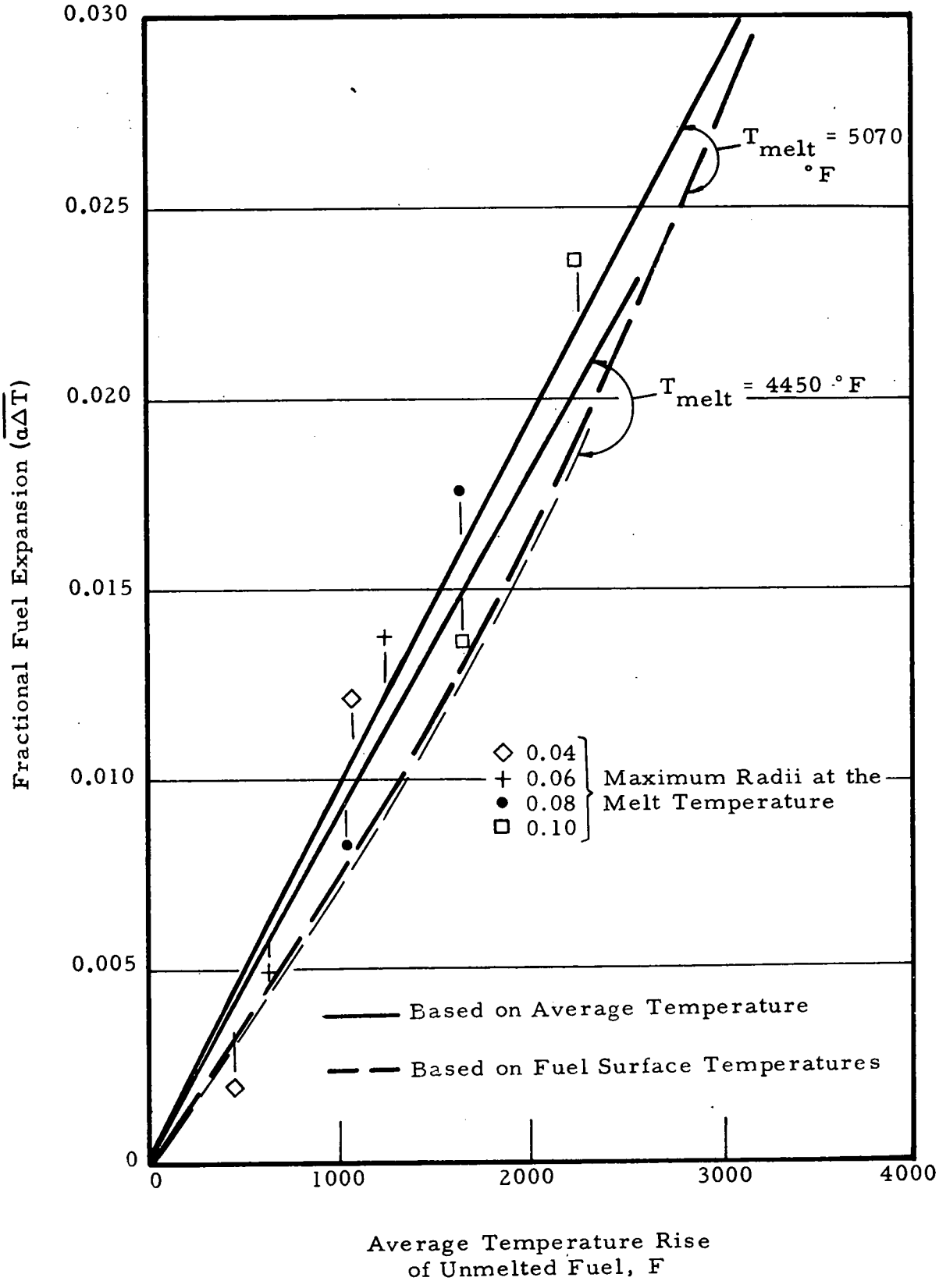

Figure A-14. Unrestrained Fuel Expansion for a Slow Power Transient — Hot Pin

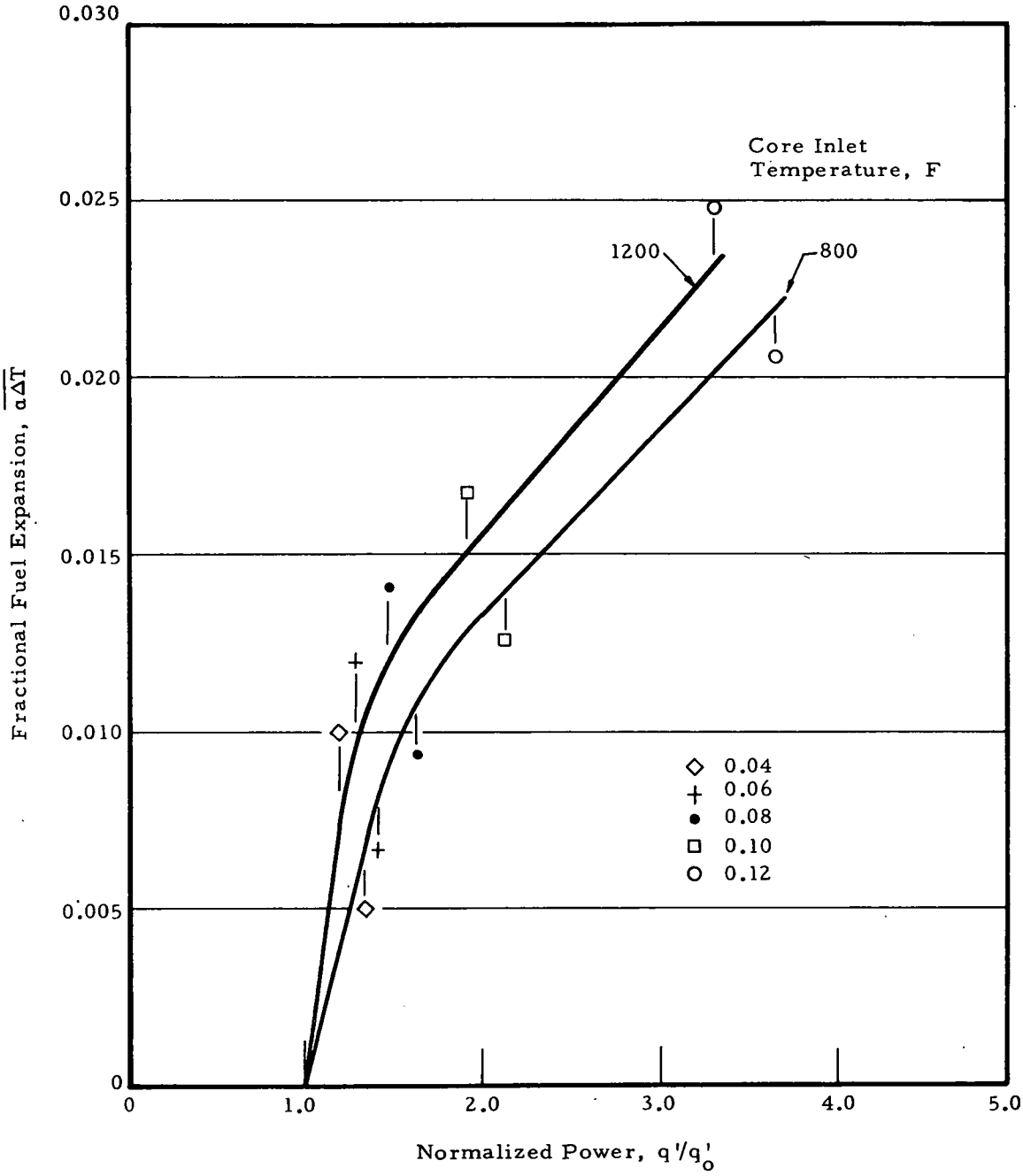

Figure A-15. Fast Transient Temperature Profiles for Fuel Beyond the Melt Temperature Isotherm — Hot Pin, Initial Condition of 100% Power

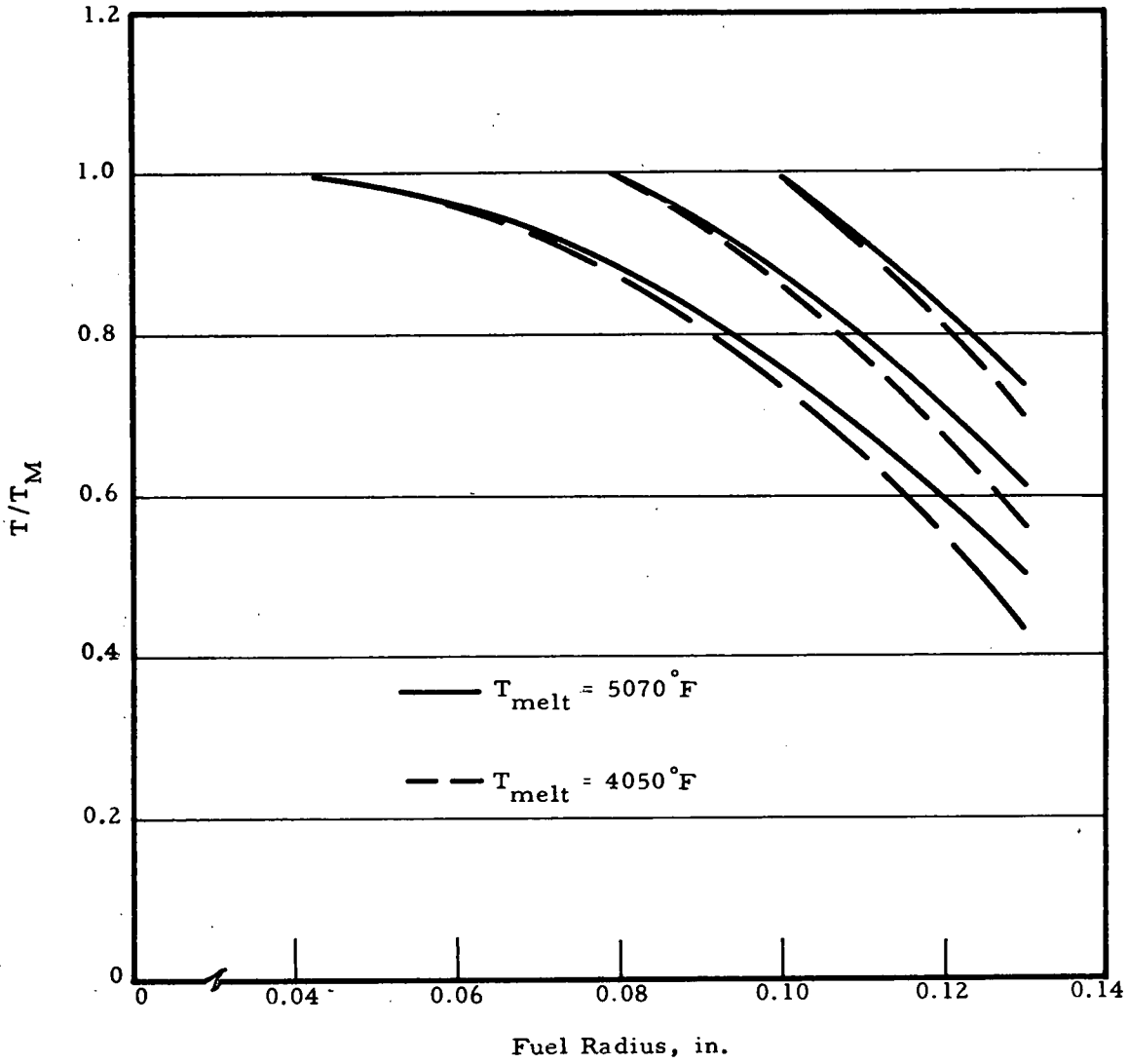

Figure A-16. Slow Transient Temperature Profiles for Fuel Beyond the Melt Temperature Isotherm

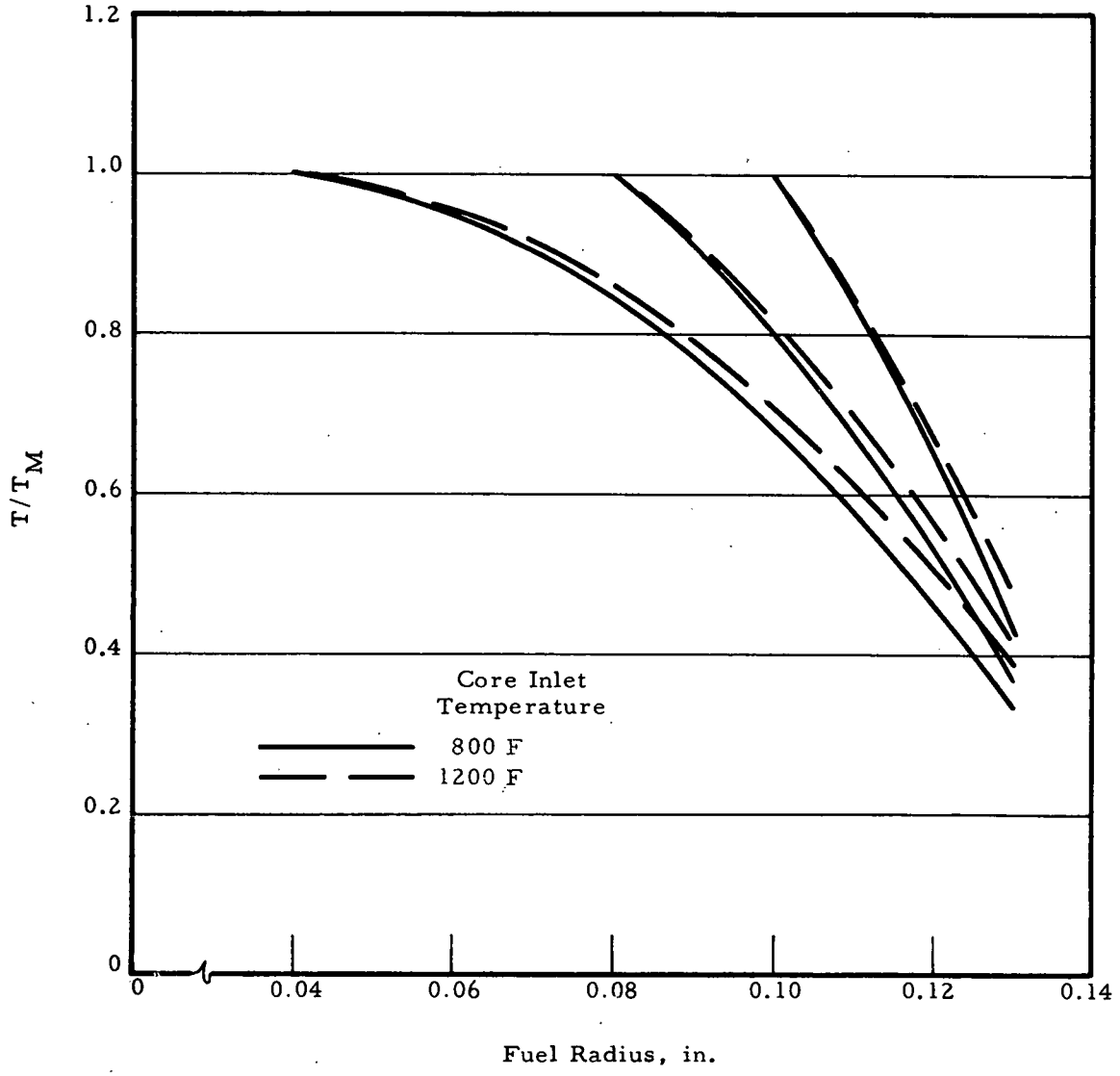

Figure A-17. Cladding Hoop Stress Required to Limit Fuel Thermal Expansion for Fast Transient

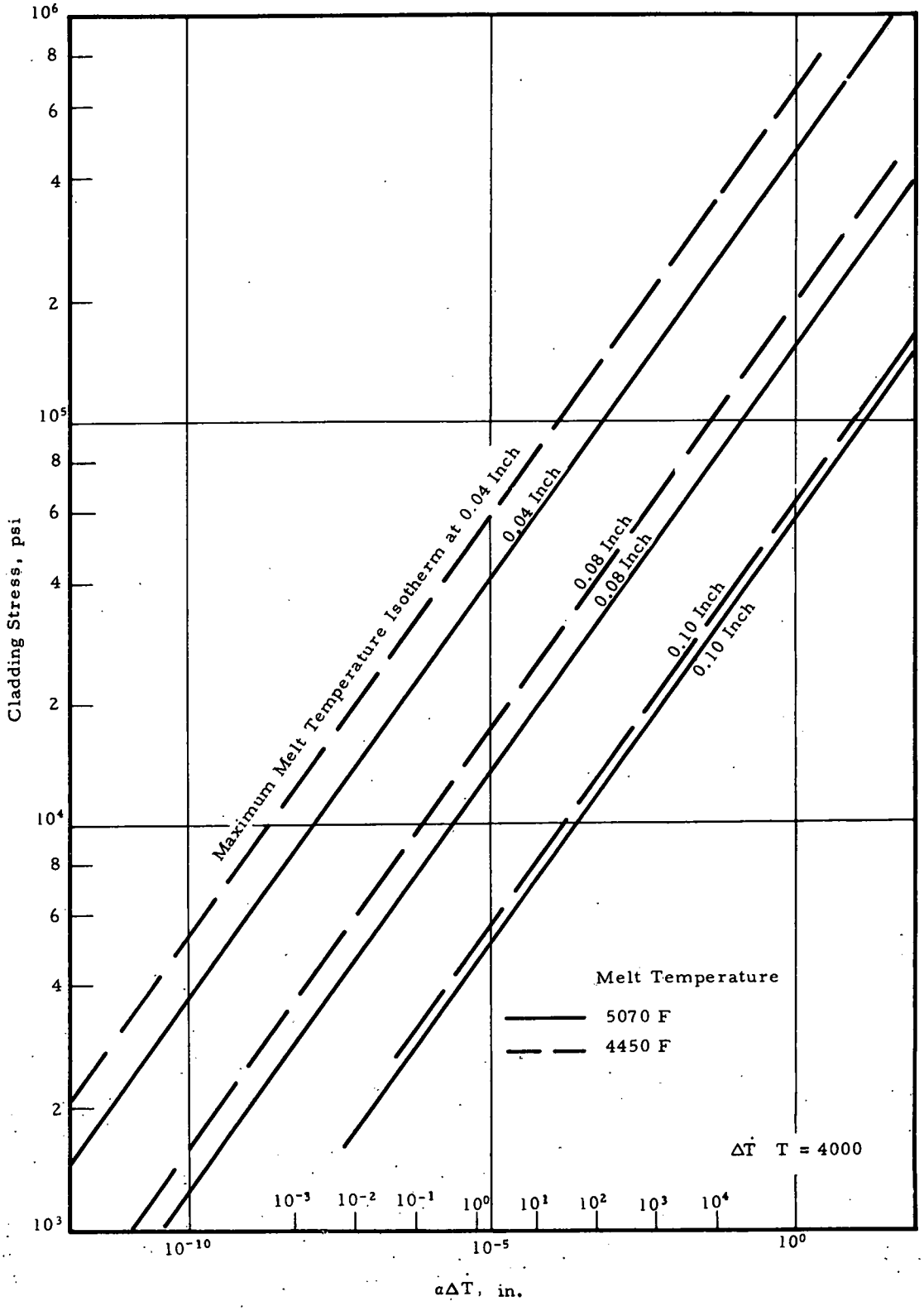

Figure A-18. Cladding Hoop Stress Required to Limit Fuel Thermal Expansion for a Slow Transient

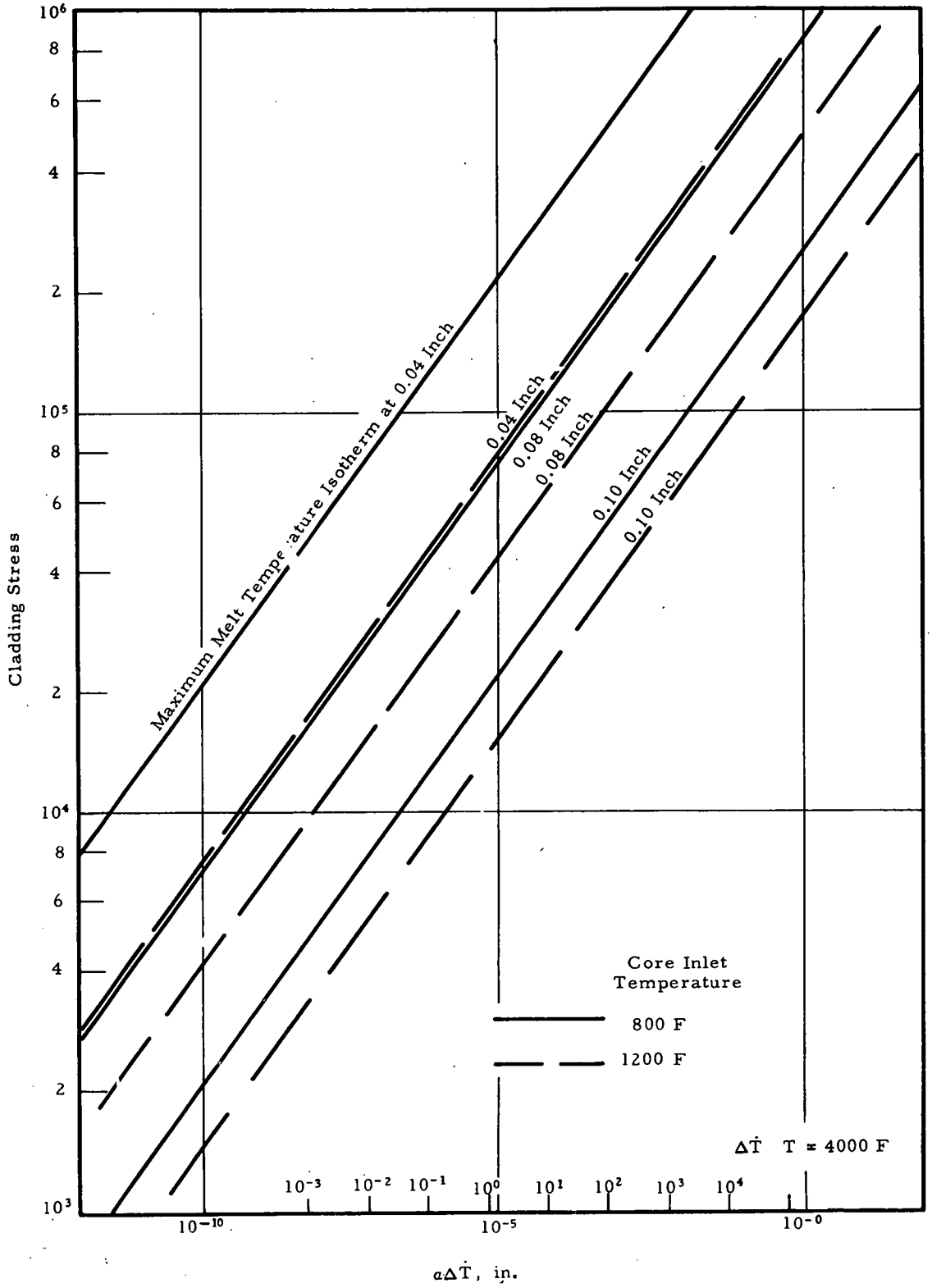

Figure A-19. Cladding Ultimate Strength Variation With Temperature

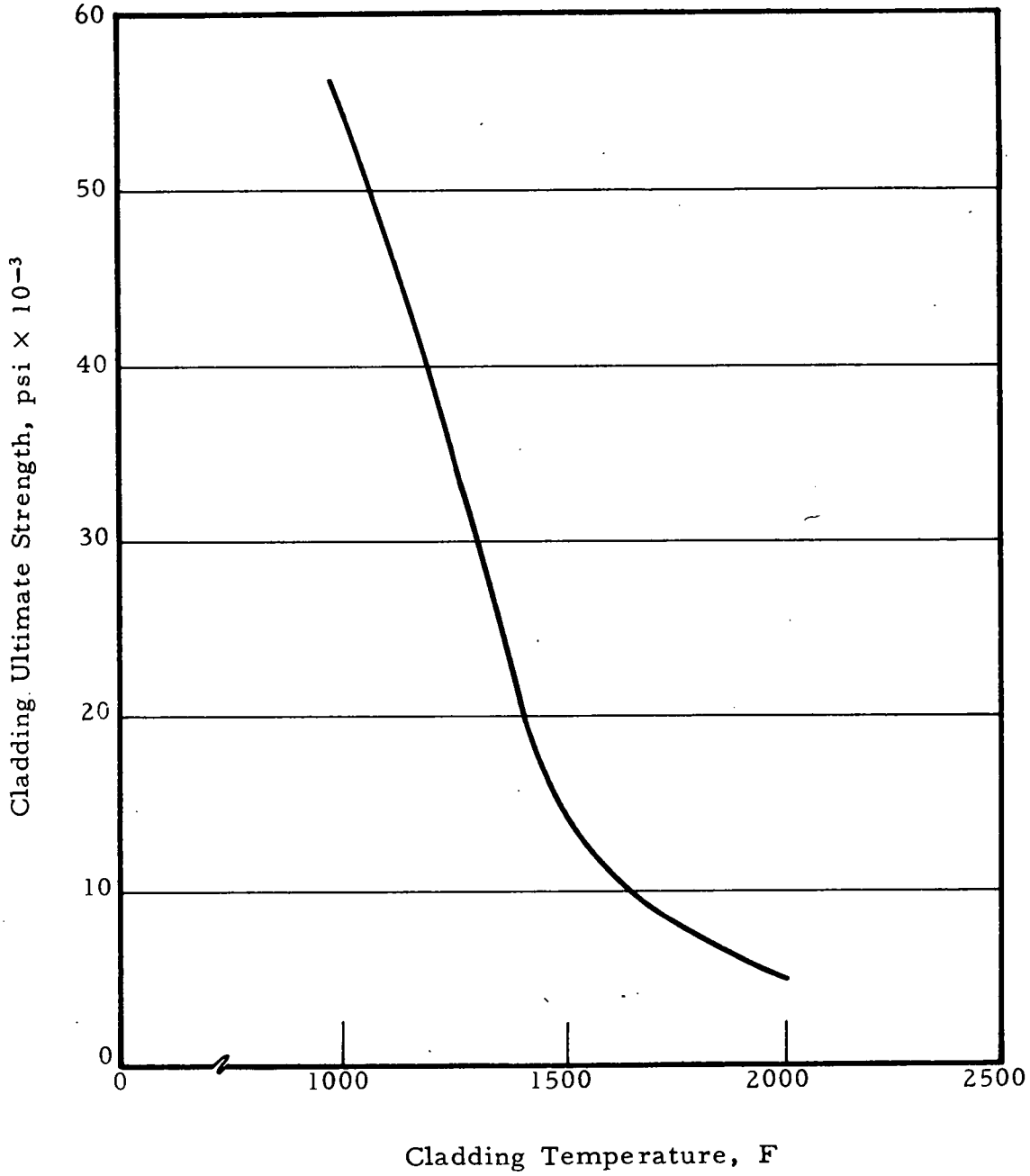

Figure A-20. Allowable Fuel Expansion Accounting for Cladding Thermal Expansion — Hot Pin, Initial Cladding Temperature of 1050 F

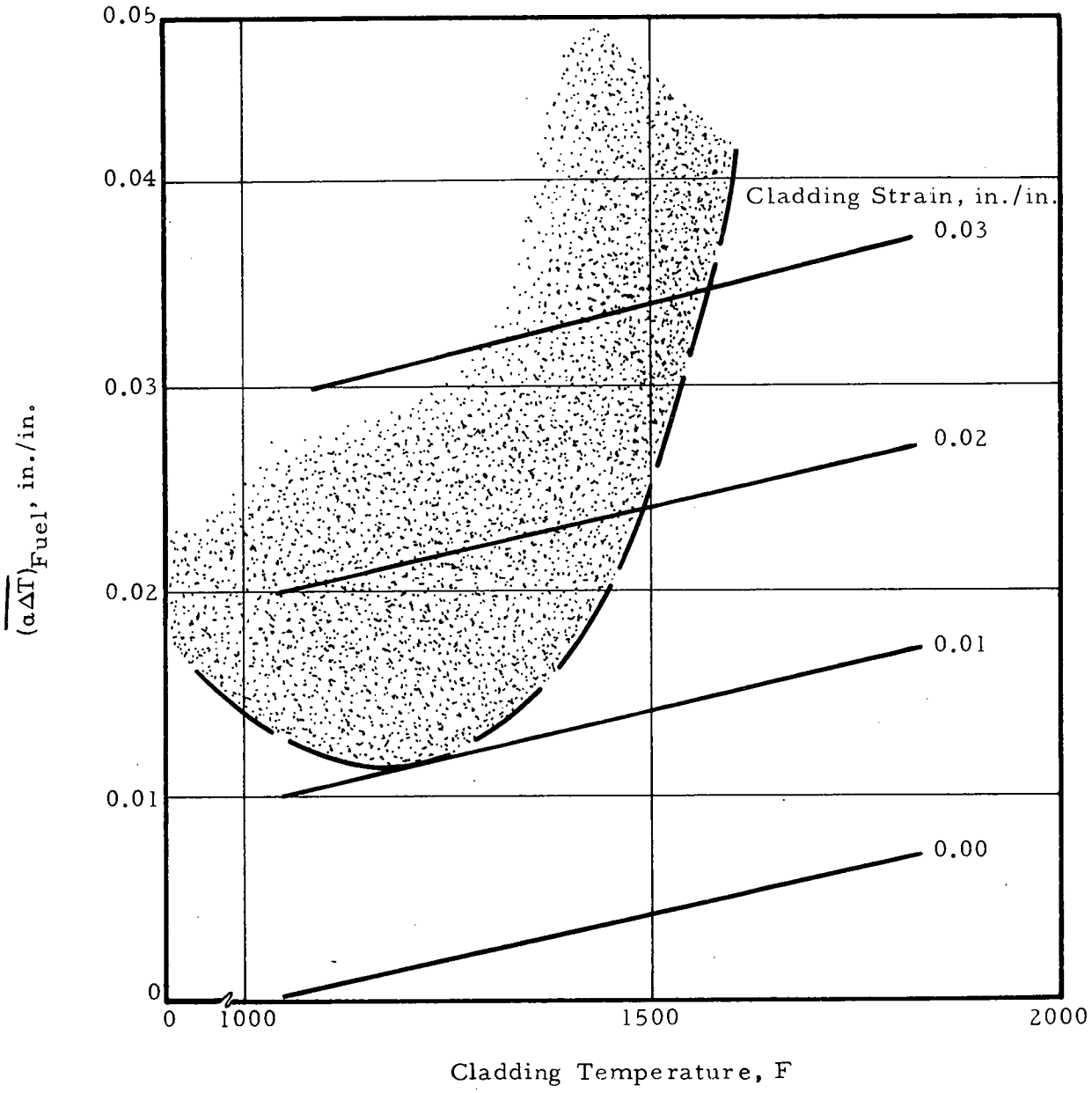

Figure A-21. Thermal Expansion of Fuel Beyond the Melt Temperature Isotherm — Hot Pin

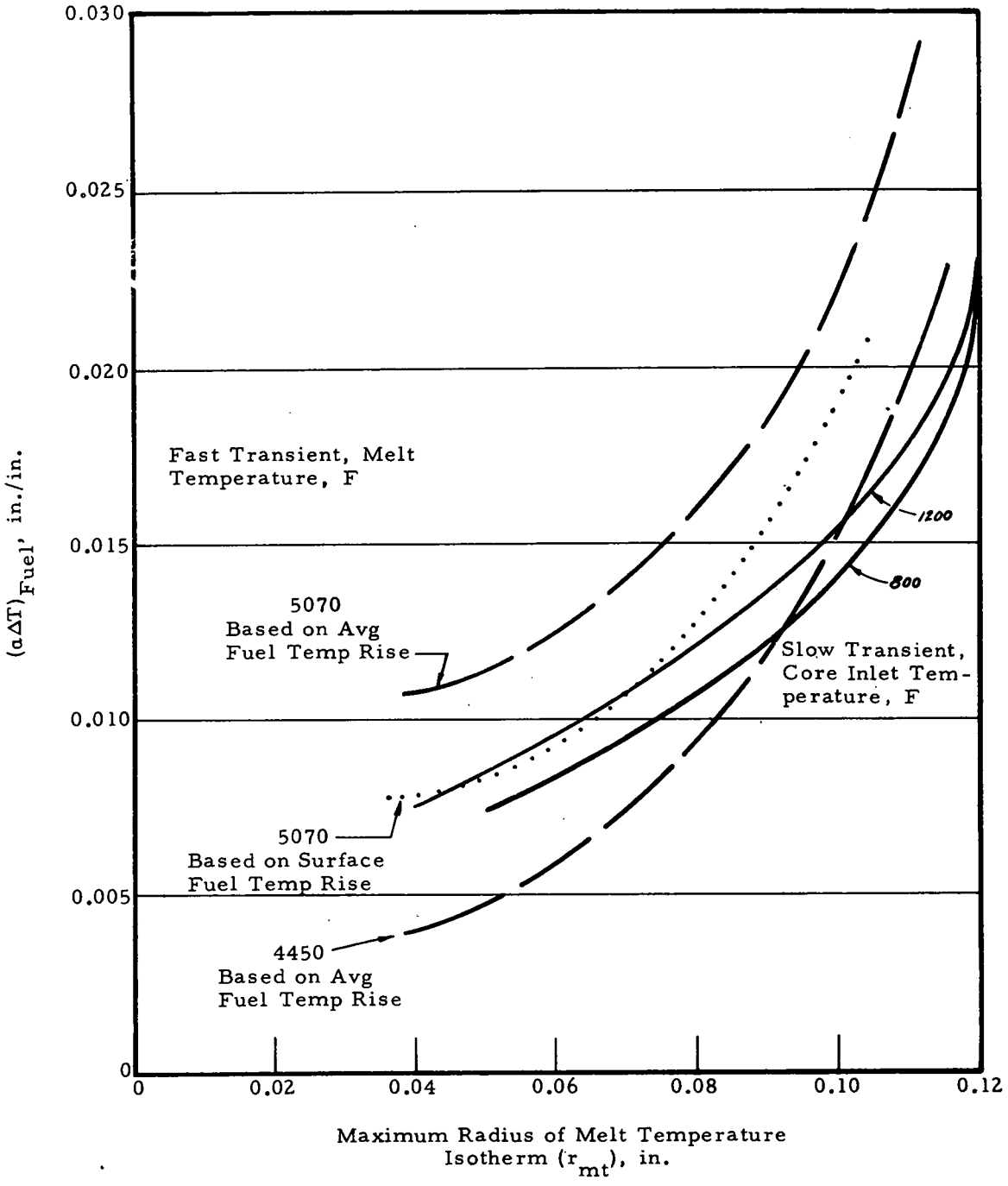

Figure A-22. Allowable Rate of Temperature Rise for Fuel Without Cladding Rupture in a Fast Transient

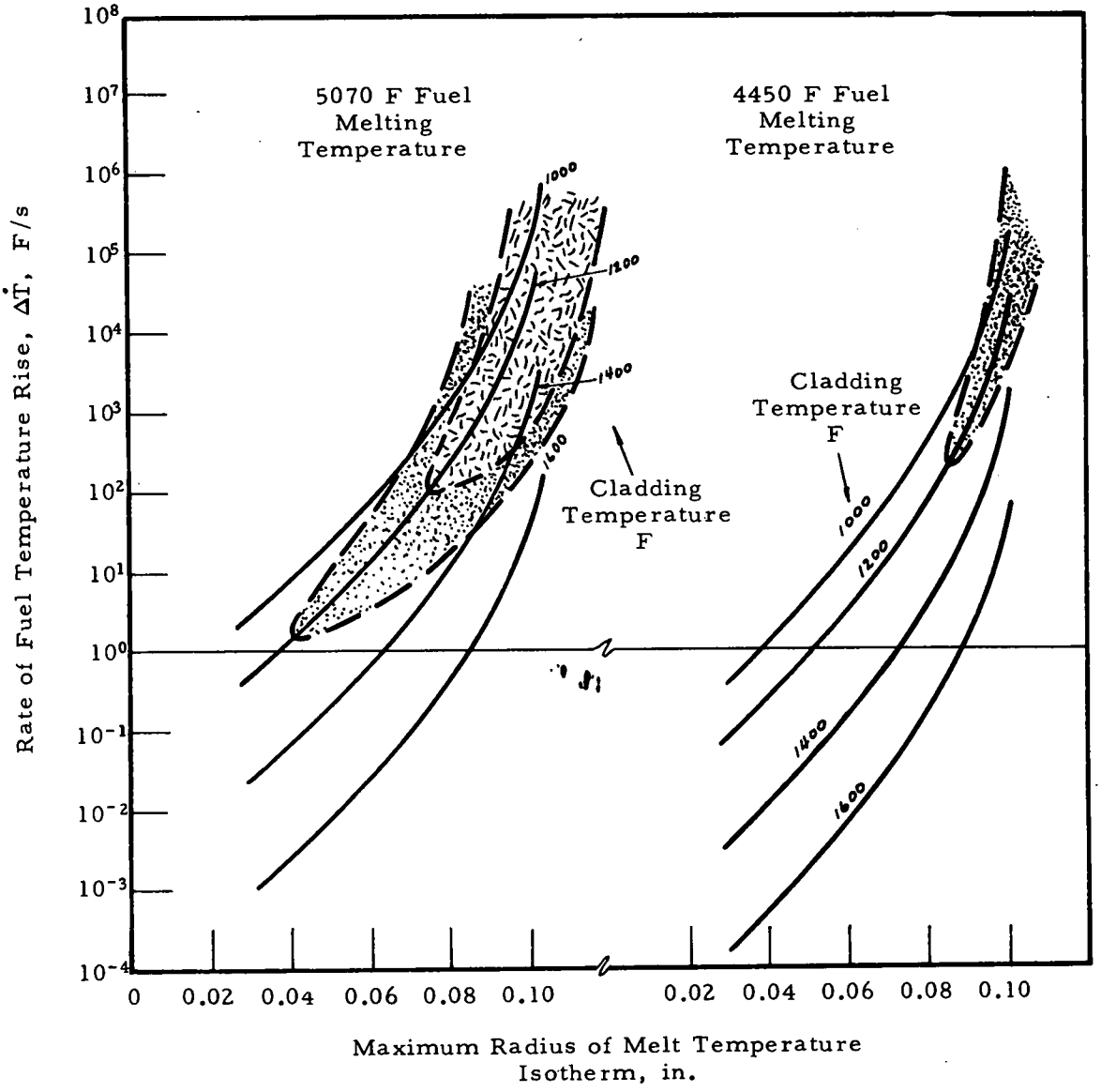

Figure A-23. Allowable Rate of Temperature Rise for Fuel Without Cladding Rupture in a Slow Transient

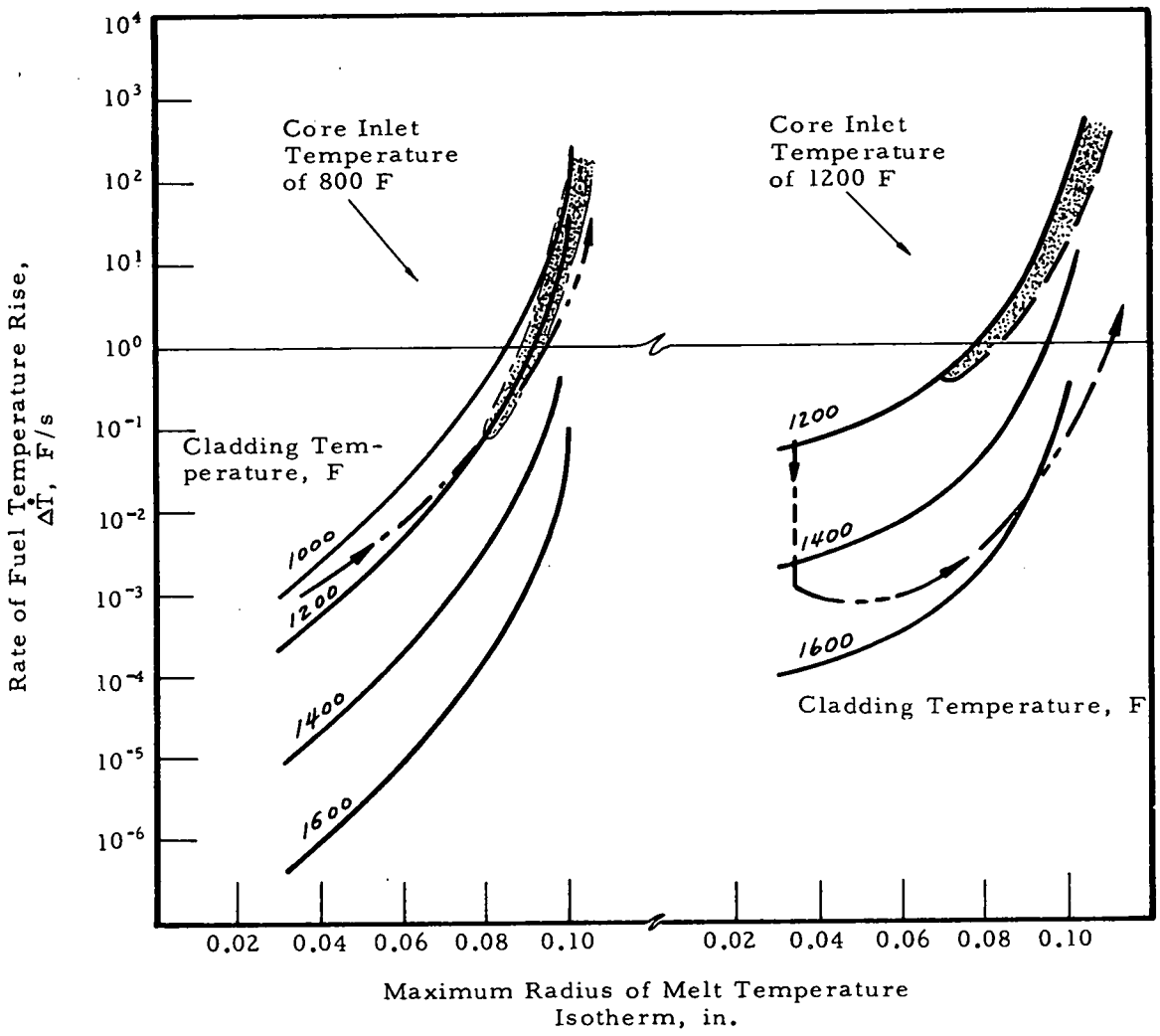

Figure A-24. Relationship Between The Fuel Pin Linear Power and Radius of Melt Temperature Isotherm for a Slow Transient

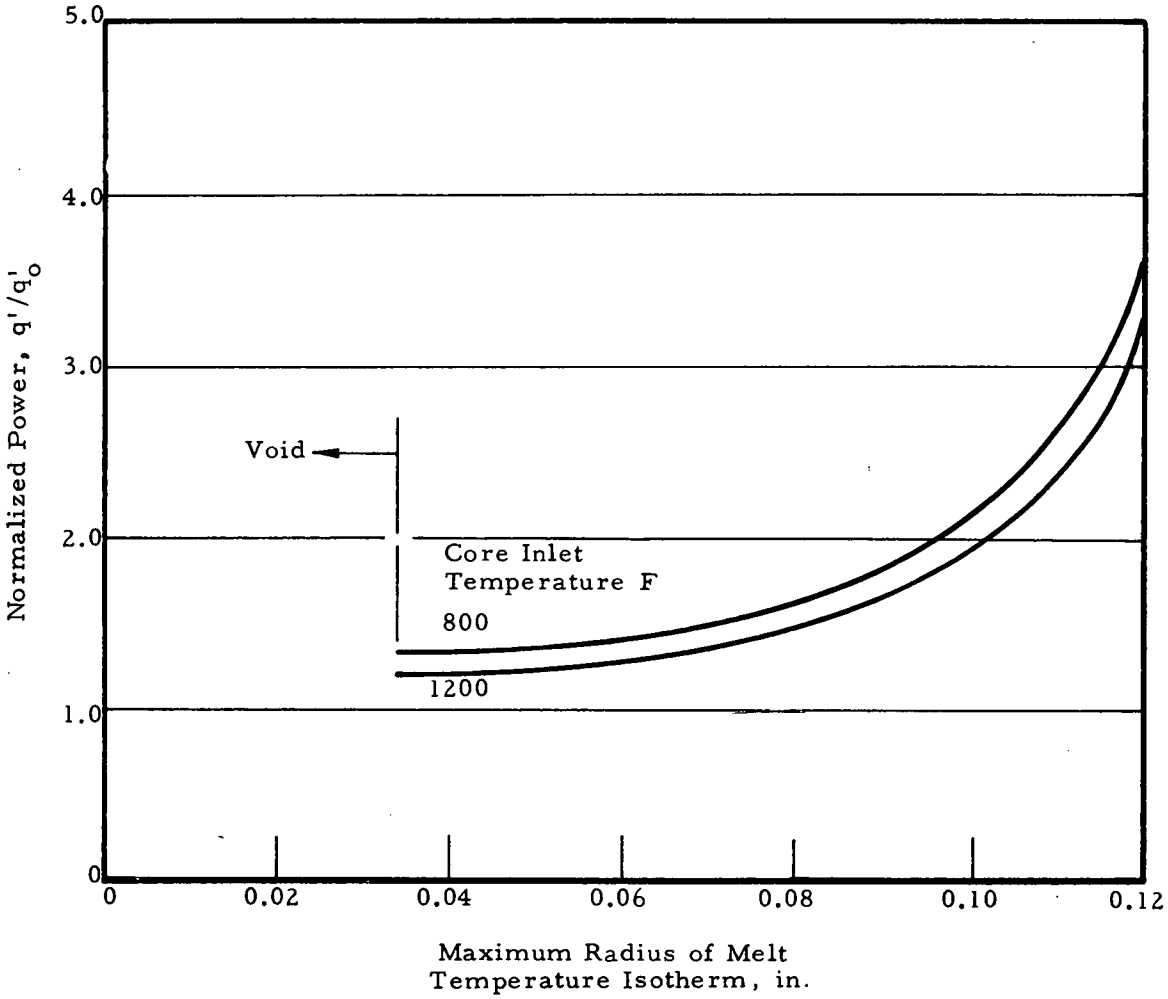

REFERENCES

[1] Hanson, J. E., and Field, J. H., Experimental Studies of Transient Effects in Fast Reactor Fuels, Series III, Pre-Irradiated Mixed Oxide (PuO_2-UO_2) Irradiations, Final Report, Transient Irradiations, GEAP-4469.

[2] Lawton, H., "The Irradiation Behavior of Plutonium-Bearing Ceramic Fuel Pins," London Conference on Fast Breeder Reactors, British Nuclear Energy Society, May 1966.

[3] AEC Fuels and Materials Development Program, 7th Annual Report, GEMP-1004, March 31, 1968.

[4] Baroch, C. J., et al., A Review of Properties Data for Fuels and Cladding for Pressurized Water and Liquid-Metal-Cooled Reactors, Babcock & Wilcox, BAW-341, Lynchburg, Virginia, August 1968.

[5] Osborn, R. B., and Sherer, D. B., Analytical Studies of Transient Effects in Fast Reactor Fuels-I, GEAP-4058, August 1962.

[6] Wolfe, R. A., and Kaufman, S. F., Mechanical Properties of Oxide Fuels (LSBR/LWB Development Program), WAPD-TM-587.

[7] Zudans, Z., et al., Thermal Stress Techniques in the Nuclear Industry, The Franklin Institute Research Laboratories, American Elsevier Publishing Company, Incorporated, New York (1965).

[8] Richards, Cedric W., Engineering Materials Science, Wadsworth Publishing Company, Incorporated, Belmont, California (1961).

UNITED STATES
ATOMIC ENERGY COMMISSION
DIVISION OF TECHNICAL INFORMATION EXTENSION

Post Office Box 62
Oak Ridge, Tennessee
37830

In Reply Refer To: TDD:PWR

October 20, 1970

Files

PROCESSING OF 1000-MWe LMFBR SAFETY STUDIES

We have been asked by L. W. Fromm, Manager, 1000-MWe Studies LMFBR Program Office, ANL, to print and distribute subject reports as a logical continuation of our involvement in the Follow-on Study Program. A total of 12 reports have been generated by BAW. There may also be a single report from each of 3 contractors, AI, GE and Westinghouse. Each report will be cleared for publication before being sent to DTIE.

Distribution is to be as follows:

UC-80	- 225 copies
NTIS	- 25 extra cys.
Stock	- 50 copies
1000 MWe Dist.	- 165 copies
	465 copies

Phillip W. Rosser

cc: Dreyer
Masters (12)

U of C-AUA-USAEC

ARGONNE NATIONAL LABORATORY

February 19, 1971

PRO:K:029

Mr. Robert L. Shannon, Director
Division of Technical Information Extension
U.S. Atomic Energy Commission
P.O. Box 62
Oak Ridge, Tennessee 27830

Subject: 1000-MWe LMFBR Safety Studies -
Publication of Babcock & Wilcox Topical Reports

Reference: Letter, L. W. Fromm to R. L. Shannon, "1000-MWe LMFBR Safety Studies - Publication of Contractors' Phase and Topical Reports," October 16, 1970

Dear Mr. Shannon:

In the reference letter I advised you that we would be transmitting to you for publication a total of twelve Babcock & Wilcox Company Phase and Topical Reports, and possibly three reports from other contractors, generated under the AEC-sponsored 1000-MWe LMFBR Safety Analysis Studies program. With that letter I enclosed one B&W report (BAW-1344, which you have since published), and advised that the remainder would be transmitted to you for publication when received and patent-cleared.

I am enclosing herewith one copy of each of the eight B&W Topical Reports listed below, all of which are now patent-cleared and ready for publication. The covers for these reports should be that used for the previously-issued BAW-1344, except for the changes noted in the table below. The letters heading the columns of the table are keyed to the markings on the attached xerox copy of the cover for BAW-1344.

OK
pwr
2-25-71

9700 South Cass Avenue, Argonne, Illinois 60439 · Telephone 312-739-7711 · TWX 910-258-3282 · WUX LB, Argonne, Illinois

"A"	"B"	"C"
BAW-1342	TOPICAL REPORT	Accident Analysis Methods
BAW-1349	TOPICAL REPORT	Candidate Secondary Containment Support Systems
BAW-1350	TOPICAL REPORT	Accident Initiating Conditions Part 1 - Flow Abnormalities
BAW-1351	TOPICAL REPORT	Candidate Emergency Decay Heat Removal Systems
BAW-1352	TOPICAL REPORT	Candidate Primary Containment Safety Features
BAW-1354	TOPICAL REPORT	Candidate Protective Features
BAW-1355	TOPICAL REPORT	Effects of Irradiation-Induced Metal Swelling on the Reference Design
BAW-1360	TOPICAL REPORT	Accident Initiating Conditions Part 2 - Reactivity Insertions

All other parts of the front covers for these reports should remain the same as the cover for BAW-1344.

Binding edge captions for the reports should read:

BAW-1342	1000-MWe LMFBR Safety Studies	B&W	Acc. Anal. Methods	USAEC
BAW-1349	1000-MWe LMFBR Safety Studies	B&W	Sec. Containment	USAEC
BAW-1350	1000-MWe LMFBR Safety Studies	B&W	Init. Cond. - 1. Flow	USAEC
BAW-1351	1000-MWe LMFBR Safety Studies	B&W	Decay Heat Removal	USAEC
BAW-1352	1000-MWe LMFBR Safety Studies	B&W	Pri Containment	USAEC
BAW-1354	1000-MWe LMFBR Safety Studies	B&W	Protective Features	USAEC
BAW-1355	1000-MWe LMFBR Safety Studies	B&W	Eff. of Metal Swelling	USAEC
BAW-1360	1000-MWe LMFBR Safety Studies	B&W	Init. Cond. - 2. Reactivity	USAEC

I note that for BAW-1344 you used a two-piece cover with staple binding, and the "binding edge caption" actually appeared on the back of the report. If this is to be the case with the reports enclosed, then the binding edge captions may be omitted. However, if any of the reports will actually have binding edges upon which printing can appear (and be visible with the reports on a library shelf), then the above captions should be used.

The distribution of all of these reports should be our "Distribution A" plus Category UC-80, Reactor Technology, as before. For your convenience I am enclosing another copy of the "Distribution A" list previously supplied to you.

In the reference letter I stated that there would be twelve B&W reports, and possibly three from other contractors. This has now been revised downward to eleven B&W reports and one report from Atomics International. The single remaining B&W report and the AI report will be transmitted to you when received and patent-cleared.

Thank you again for your excellent cooperation in publishing these reports. If there are any questions, please contact me on FTS extension 312/739-2971 or 312/739-4844.

Very truly yours,

L. W. Fromm, Manager
1000-MWe Studies
LMFBR Program Office

LWF:el
encls.

cc: (w/o encl.)
AEC-RDT: Director
Asst. Dir. for Project Mgt.
Chief, Liquid Metal Proj. Br.
LMFBR Program Manager
Sr. Site Representative - ANL

Manager, AEC-CH
Director, LMFBR Program Office - ANL (2 copies)
R. C. Dreyer, DTIE
C. R. Bruce, DTIE
P. W. Rosser, DTIE

BAW-1344 "A"

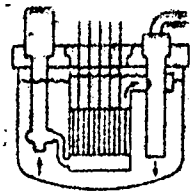

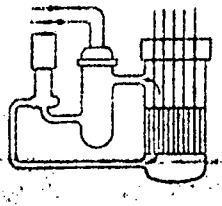

1000 MWe LMFBR

Liquid Metal Fast Breeder Reactor

SAFETY ANALYSIS STUDIES

BABCOCK & WILCOX

Accident Analysis and Safety System Design Study

PHASE I REPORT "B"

Fault Trees and Malfunction Catalog "C"

Prepared for ARGONNE NATIONAL LABORATORY

Rev. per
D. McGoff
8/5/68

DISTRIBUTION "A"

(1 copy to each addressee unless otherwise noted)

Division of Reactor Development and Technology
U. S. Atomic Energy Commission
Washington, D. C. 20545

Milton Shaw, Director
Assistant Director for Project Management
Chief, Liquid Metal Projects Branch (2 copies)
LMFBR Program Manager
Assistant Director for Plant Engineering
Chief, Applications and Facilities Branch
Chief, Components Branch
Chief, Systems Engineering Branch
Assistant Director for Reactor Engineering (2 copies)
Chief, Core Design Branch
Chief, Fuel Handling Branch
Assistant Director for Reactor Technology
Assistant Director for Nuclear Safety
Assistant Director for Program Analysis
Project Manager, FFTF

Director, LMFBR Program Office - ANL (2 copies)
Argonne National Laboratory
9700 South Cass Avenue
Argonne, Illinois 60439

Office of Senior RDT Site Rep. - AI
U. S. Atomic Energy Commission
P. O. Box 309
Canoga Park, California 91304

Office of Senior RDT Site Rep. - APDA
U. S. Atomic Energy Commission
1911 First Street
Detroit, Michigan 48226

Office of Senior RDT Site Rep. - GE
U. S. Atomic Energy Commission
310 DeGuigne Drive
Sunnyvale, California 94086

Office of Senior RDT Site Rep. - PNL
U. S. Atomic Energy Commission
Federal Building
Richland, Washington 99352

Office of Senior RDT Site Rep. - ID
U. S. Atomic Energy Commission
P. O. Box 2108
Idaho Falls, Idaho 83401

Office of Senior RDT Site Rep. - GGA
U. S. Atomic Energy Commission
P. O. Box 2525
San Diego, California 92112

Office of Senior RDT Site Rep. - ORNL
U. S. Atomic Energy Commission
P. O. Box X
Oak Ridge, Tennessee 37830

Office of RDT Site Rep. - GE
U. S. Atomic Energy Commission
P. O. Box 500
Windsor, Connecticut 06095

Office of RDT Site Rep. - UNC
U. S. Atomic Energy Commission
Grandview Road
Elmsford, New York 10523

Reactor Systems and Performance Branch
Division of Reactor Standards - BETH - 010
U. S. Atomic Energy Commission
Washington, D. C. 20545

Atten: Mr. C. L. Allen

Division of Reactor Licensing - BETH - 010
U. S. Atomic Energy Commission
Washington, D. C. 20545
Atten: Dr. P. Morris, Director (1 copy)
Mr. S. Levine (1 copy)

Chief, Foreign Activities Staff
Office of Assistant General Manager for Reactors
U. S. Atomic Energy Commission
Washington, D. C. 20545

Mr. Carl R. Malmstrom
U. S. Atomic Energy Commission
Scientific Representative - London
American Embassy Box 40
F.P.O., New York 09510

Mr. Joseph DiNunno
U. S. Atomic Energy Commission
Scientific Representative - Paris
American Embassy
A.P.O., New York 09777

Mr. Dickson B. Hoyle
U. S. Atomic Energy Commission
Senior Scientific Representative
U. S. Mission to the European Communities
U. S. Embassy
A.P.O., New York 09667

Dr. William H. Hanum
Fast Reactor Physics Division
Atomic Energy Establishment, Winfrith
Dorchester, Dorset, England

Mr. Robert E. Macherey
Metallurgical Specialist
Fast Reactor Fuels
Gesellschaft fur Kernforschung M.B.H.
Postfache 947
75 Karlsruhe, Germany

Dr. Stanley J. Stachura
Commissariat a 1' Energie Atomique
Centre d' Etudes Nucleaires de Cadarache
Boite Postale 1
St. Paul Les Durance (B. Du. Rh.), France

Brookhaven National Laboratory
Upton, New York 11973
Attn: M. Goldhaber, Director (2 copies)

Los Alamos Scientific Laboratory
Post Office Box 1663
Los Alamos, New Mexico 87544
Attn: Dr. David B. Hall (2 copies)

Oak Ridge National Laboratory
Union Carbide Corporation
AEC Operations - Post Office Box X
Oak Ridge, Tennessee 37831
Attn: Dr. Floyd L. Culler (2 copies)

Oak Ridge National Laboratory
Building 9201-2, Y-12
Post Office Box Y
Oak Ridge, Tennessee 37830
Attn: Mr. R. E. MacPherson, Jr.

Atomics International
A Division of North American Rockwell Corporation
Post Office Box 309
Canoga Park, California 91304
Attn: Mr. J. J. Flaherty, President

Liquid Metal Engineering Center
P. O. Box 1449
Canoga Park, California 91304
Attn: Mr. R. W. Dickinson, Director (3 copies)

General Electric Company
Advanced Products Operation
310 DeGuigne Drive
Sunnyvale, California 94086
Attn: Mr. Karl P. Cohen, Manager (3 copies)

Pacific Northwest Laboratory
Battelle Memorial Institute
Post Office Box 999
Richland, Washington 99352
Attn: Dr. F. W. Albaugh, Director (1 copy)
Dr. E. R. Astley, Project Mgr., FFTF (4 copies)

Westinghouse Electric Corporation
Advanced Reactors Division
Waltz Mill Site - P.O. Box 158
Madison, Pennsylvania 15663
Attn: Dr. J.C.R. Kelly, Jr., General Manager (2 copies)

Combustion Engineering, Inc.
Nuclear Power Department
P.O. Box 500
Windsor, Connecticut 06095
Attn: Dr. Walter H. Zinn (2 copies)

MSA Research Corporation
Callory, Pennsylvania 14024
Attn: Mr. C. H. Staub, Director, Marketing Division

Atomic Power Development Associates, Inc.
1911 First Street
Detroit, Michigan 48226
Attn: Mr. Alton P. Donnell, General Manager (2 copies)

Power Reactor Development Company
1911 First Street
Detroit, Michigan 48226
Attn: Mr. Arthur S. Griswold, General Manager

United Nuclear Corporation
Post Office Box 1583
365 Winchester Avenue
New Haven, Connecticut 06511
Attn: Mr. A. Schaaser (1 copy)
Dr. K. Gottmann (1 copy)

The Babcock & Wilcox Company
Atomic Energy Division
Technical Library
5061 Fort Avenue - P.O. Box 1260
Lynchburg, Virginia 24505
Attn: Mr. S. H. Esleeck (3 copies)

General Atomics
Division of General Dynamics Corporation
Post Office Box 608
San Diego, California 92115
Attn: Dr. Frederic de Hoffmann

Nuclear Materials & Equipment Corporation
Apollo, Pennsylvania 15613
Attn: Dr. Z. M. Shapiro, President

Baldwin-Lima-Hamilton Corporation
Industrial Equipment Division
Eddystone, Pennsylvania 19013
Attn: Mr. John Gaydos, Senior Engineer (1 copy)
Mr. R. A. Tidball (1 copy)

M. W. Kellogg Company
711 Third Avenue
New York, New York 10017
Attn: Mr. D. W. Jesser, Vice President of Engineering

Southwest Atomic Energy Associates
Post Office Box 1106
Shreveport, Louisiana 71102
Attn: Mr. J. Robert Welsh, President

U. S. Atomic Energy Commission
Technical Information Extension
Post Office Box E
Oak Ridge, Tennessee 37830
Attn: Mr. Robert L. Shannon, Manager (3 copies)

Professor W. Haefele
Kernforschungszentrum Karlsruhe
7500 Karlsruhe, Germany (10 copies)

Mr. C. Vendryes
CEN Saclay
Boite Postale 2
Gif-Sur-Yvette (S at O), France (10 copies)

Mr. A. deStordeur
Euratom
53 Rue Belliard
Brussels 4, Belgium (10 copies)

Dott, Ing. F. Pierantoni
CNEN
Via Mazzini 2
Bologna, Italy (4 copies)

United Kingdom Atomic Energy Authority
Reactor Group Headquarters
Kisley, Warrington; Lancashire
England
Attn: Mr. Robin Nicholson, Head of Commercial and Overseas Relations Dept. (12 copies)

Argonne National Laboratory
9700 S. Cass Avenue
Argonne, Illinois 60439
Attn: Mr. L. W. Fromm (40 copies)